Performance prediction for a homopolar linear synchronous machine.

Helani, Mohammad Fayz

Award date:
1984

Awarding institution:
University of Bath

PERFORMANCE PREDICTION FOR A HOMOPOLAR LINEAR SYNCHRONOUS MACHINE

Submitted by

Mohammad Fayz Helani

for the degree of PhD

of the University of Bath

1984

COPYRIGHT

M.F. Helani

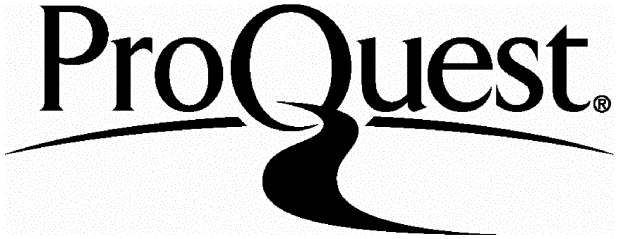

ABSTRACT

The synchronous reactances of a salient-pole synchronous machine are functions of the load of the machine because of the non-linearity caused by magnetic saturation. In the d-axis the machine is more saturated than in the q-axis, and for exact analysis appropriate saturated reactances have to be used.

A three dimensional numerical solution of the field problem, based on network method is developed to calculate the reactance. The non-linearity of the magnetic materials, the complicated contours of the cross section of the machine, and the currents in the various windings are fully considered. The analysis is applied to the predetermination of flux and flux density in a homopolar linear synchronous machine. The flux densities are used to predict the magnetising inductances, by the use of a flux linkage method. The normal forces acting between the rotor and stator are also calculated in a number of different ways including the use of Maxwell's stress.

The field is described and the simplifying assumptions and boundary conditions are discussed. The governing equations for scalar potential in terms of network properties are developed from Maxwell's equations. The numerical solution of the linear set of network equations is obtained by successive over-relaxation and the nonlinearity is considered by an alternating relaxation procedure. The difficulties associated with the use of scalar potential have been overcome by considering the permeable region to be current free. All the current-carrying conductors are placed in the surrounding air.

Equations for a simple air-gap calculation of the inductances and normal forces in a homopolar linear synchronous machine are derived. The leakage inductances produced by air-gap flux which fails to reach the rotor have been considered as parts of the magnetising inductances. Inclusion of these leakage components enables close agreement to be obtained with the measured voltages. The leakage components have no influence on the forces produced by the homopolar LSM.

The good agreement achieved in a comparison between the calculated and experimental results for the homopolar linear synchronous motor, confirms the validity and accuracy of the network field calculation method.

The mechanical and electrical characteristics of the homopolar LSM are compared with those already found for a heteropolar machine. The advantages and disadvantages of both these machines for advanced transport system are discussed in detail. Methods for improvement of power factor and for reducing pole losses are also mentioned.

ACKNOWLEDGEMENTS

The author wishes to express his gratitude to his supervisor, Dr. M.J. Balchin, for providing advice and daily guidance throughout the course of the work presented in this thesis. Thanks are also due to Professor J.F. Eastham for his continued interest in the project and for many useful discussions.

Dr. J.A.M. Davidson gave much advice on computational aspects of the work and J. McCaig constructed the experimental apparatus. The Author thanks both for giving their time and skills so generously.

The author also wishes to thank Mrs. A. Balchin for her careful and efficient typing of this thesis.

Thanks are due to the Syrian Government for providing financial support to the Author during the course of the work.

In addition, the Author wishes to thank the Science Research Council for the computing facilities.

Finally, the Author gratefully acknowledges the continued support and encouragement of his wife, Fikrat, and the forbearance of his children Firas and Fadi.

CONTENTS

LIST OF PRINCIPAL SYMBOLS

H	=	field intensity
B	=	flux density
ϕ	=	flux
A	=	area
μ	=	permeability
m	=	magnetomotive force (mmf)
P	=	permeance
V	=	magnetic scalar potential
J	=	current density
I_f	=	field current
I_a, I	=	rms armature current
μ_o	=	permeability of free space
λ	=	flux linkage
L	=	inductance
M_{af}	=	mutual inductance between field and armature winding
E	=	induced phase voltage
ω	=	angular frequency
Z_f	=	series conductors per field winding slot
Z_a	=	series conductors per armature winding slot
K_w	=	winding factor
q	=	slots per pole and phase
g	=	air-gap at pole centre
W	=	stator width
τ_p	=	pole pitch
p	=	number of pole pairs
δ_i	=	torque angle

$F_{N,n}$ = normal force

F_t = thrust force

ℓ = track pole length

CHAPTER ONE

General Introduction

All forms of rotary electrical machine have their linear counterparts. The use of the linear forms is particularly attractive in the field of electric traction since direct propulsion is possible. This removes the need for mechanical power transmission components and also the necessity for wheel to track adhesion.

In addition to the thrust forces that are produced by linear machines there also exist components of force that act in a direction normal to the track surface. These forces can be utilised to support a complete vehicle. If wheels are used then the normal force could be used to support the traction motors so that the size of the suspension components could be reduced.

Linear forms of the induction machine (Fig.1.1) have received most attention for use in traction applications[1.3,1.4,1.6]. This is because such machines produce force at all speeds (up to synchronous speed) from a fixed-frequency ac supply. Speed control is also possible by using a very simple voltage controller. Although attractive at first sight the linear induction machine has a number of deficiencies.

Induction machines have high efficiencies only in the vicinity of synchronous speed. In traction applications long periods of operation at other speeds would probably be necessary. This difficulty can be partially overcome by using pole-change windings, or be completely removed by the use of a variable-frequency supply.

Rotary induction machines have very small air-gaps in order to keep the magnetising component of current as small as possible. This current is purely reactive and its effect is to reduce the motor power factor. In linear induction machines, it is necessary to use relatively large air-gaps in order to accommodate the rotor conductor and also to provide

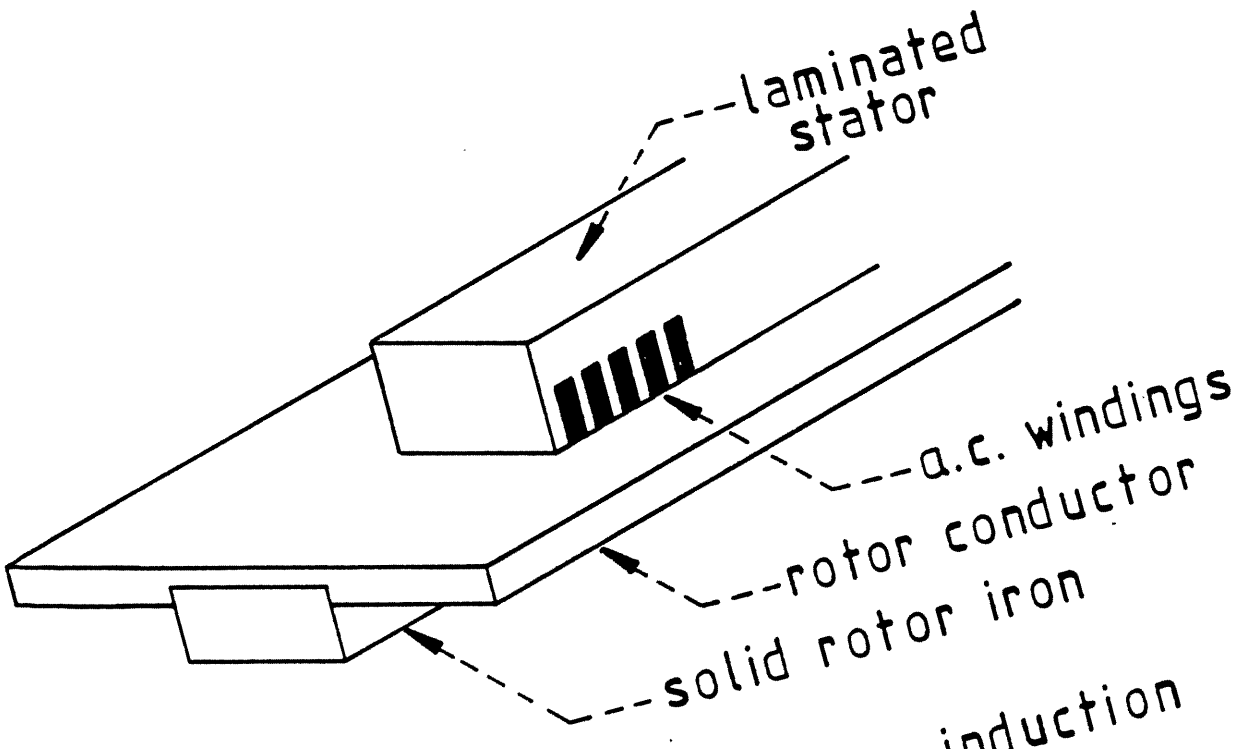

Fig 1·1 : Single-sided linear induction motor .

adequate clearance between motor and track.

In linear induction machines the edges of the wound (stator) member give rise to transient effects which can make the characteristics of the motor very different from those predicted on the basis of conventional theory. In short stator machines transient currents are induced in each element of the rotor as it passes beneath the entry edge of the stator. These currents tend to reduce the normal flux density. At the exit end, the normal flux density is distributed behind the stator by the exit edge transient currents. The result of these two effects (which are together known as the longitudinal edge effect[1.4]) is to cause reductions in efficiency, power factor, and thrust that are dependent on speed[1.4].

Because of the low power factors and efficiencies that are obtainable from linear induction machines, interest is currently being shown in linear forms of synchronous machine. This form of machine has the advantage that the air-gap magnetising current is supplied by a dc excited winding so that improved power factors are obtainable. Linear forms of the wound rotor machine are not considered to be applicable for traction applications since the production of a long, wound secondary is potentially very expensive. The most economical form of machine for this duty is an inductor-type machine in which both the ac and the dc excited windings reside on the short primary member that is attached to the vehicle.

Figure 1.2 shows a form of "claw pole" linear synchronous motor considered by Levi[1.2]. When the dc winding is energised alternate N and S poles are produced beneath the primary on the track member. The ac winding is wound with the same pole-pitch as the track member.

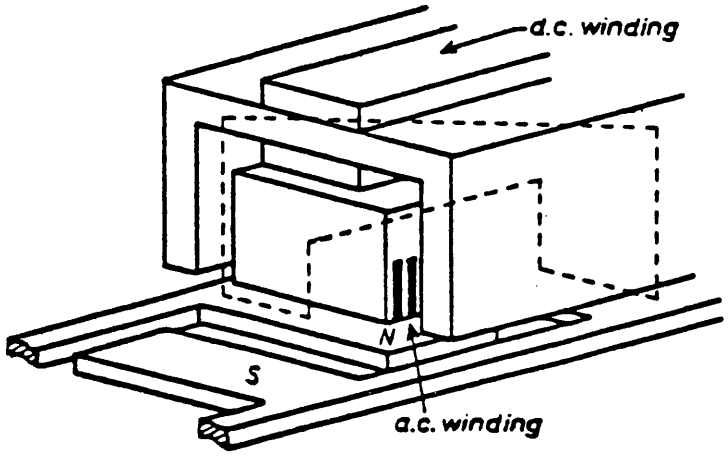

Fig 1·2 : Claw-pole hetropolar linear synchronous motor.

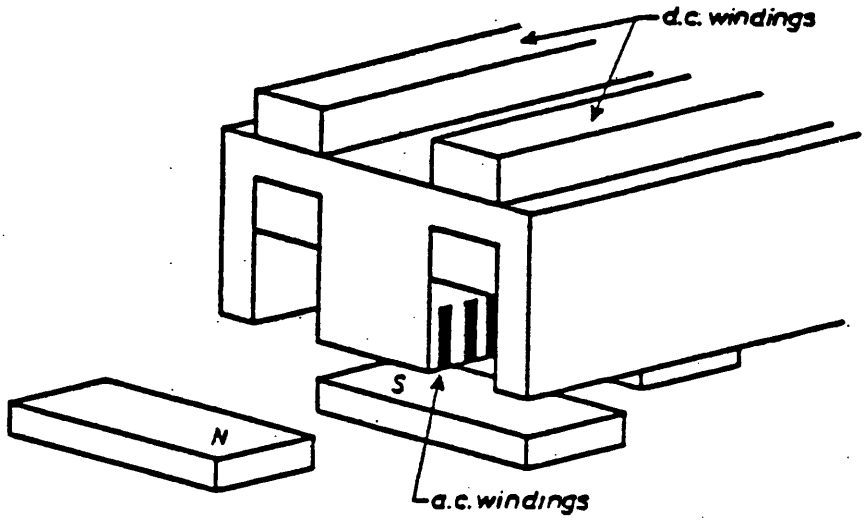

Fig 1·3 : Transverse-flux hetropolar linear synchronous motor.

When energised with ac a field is produced that has a velocity relative to the primary. Provided that the ac field has a velocity equal and opposite to that of the vehicle it will be stationary relative to the track poles and thrust force will be produced.

In order for the motor of Fig. 1.2 to produce thrust at all speeds it is necessary to use a variable-frequency ac supply. Variable voltage is also necessary in order to produce variable thrust. Both functions are available from modern voltage source or current source inverters.

The flux paths in the Levi machine are rather long, complex and prone to leakage. A more compact form of machine (Fig. 1.3) was first described in Reference 1.1 and tests on a practical model and a first analysis given in Reference 1.5. In this machine the dc flux paths lie in planes that are transverse to the direction of motion. This results in a much simpler track construction than is required for the machine of Fig. 1.2. The ac flux can take longitudinal or transverse paths depending on the position of the poles produced by the ac current relative to the track poles. When the track poles are coincident with the ac field poles (the d-axis position in conventional synchronous machine theory) the flux is transverse. At a position where the track pole is midway between two ac poles (the q-axis position) the flux takes longitudinal paths.

Figure 1.4 shows a linear form of the "homopolar inductor alternator" type of machine[1.2]. In this form of machine the dc winding produces N poles on one side of the track member and S poles on the other. The two ac windings have a pole-pitch of one half of the distance between the track poles. Force is produced by the same mechanism as was described for the heteropolar machines.

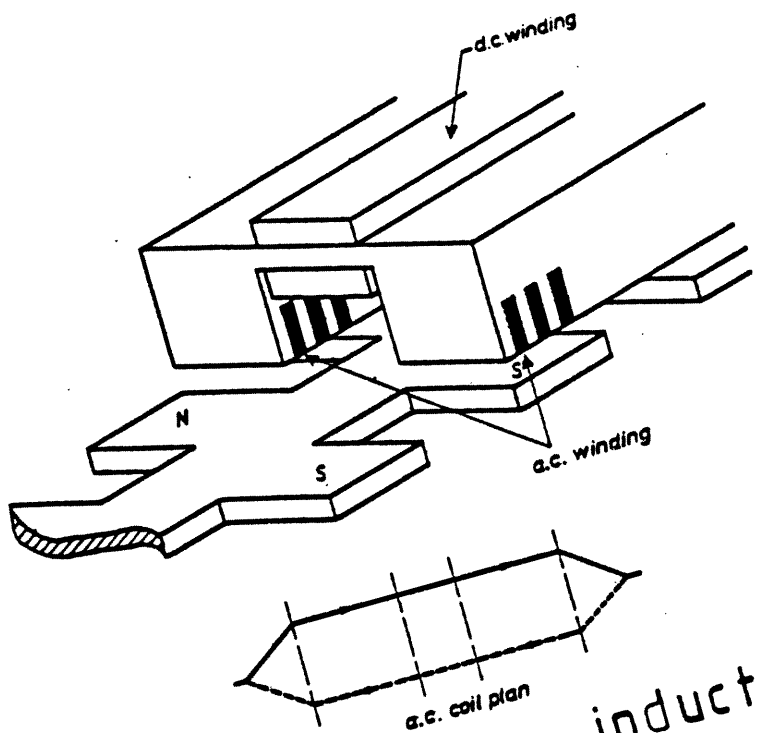

Fig 1·4 : Homopolar-inductor-type linear synchronous motor.

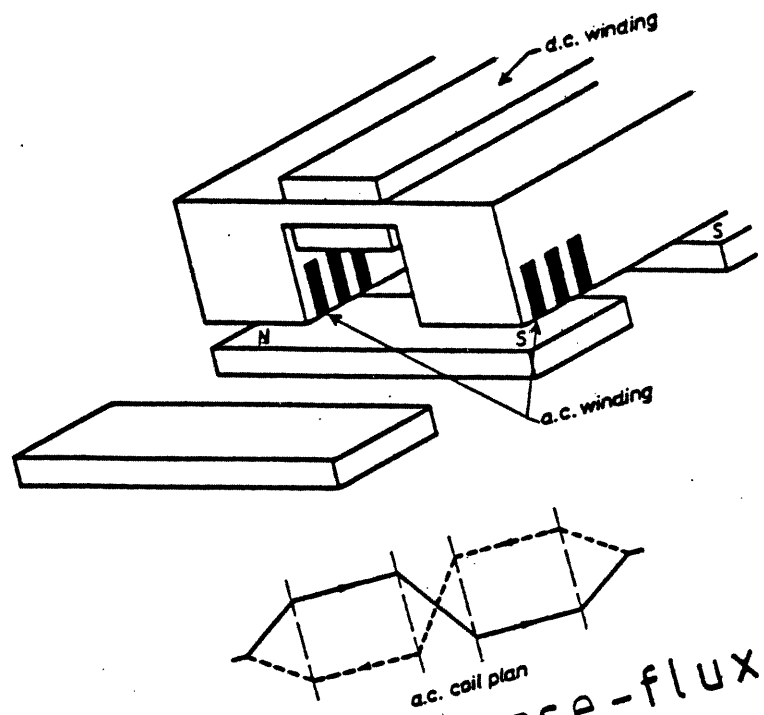

Fig 1·5 : Transverse-flux homopolar linear synchronous motor.

The complexity of the track member used by the machine of Fig. 1.4 can be reduced by rearranging the position of the two ac windings as shown in Fig. 1.5[1.1]. The individual coils could be simply formed by using a "cross-over" between the two side limbs[1.6].

The rotor member in the linear inductor machines is only required to complete the flux paths and not, as in the case of the induction machine, to support the secondary currents. Rotor resistance can therefore be made as high as is practically possible. By this means the longitudinal edge effects can be almost entirely eliminated with consequent improvements in both power factor and efficiency. A further advantage of the reduced edge effect is that the theories which have been developed for cylindrical synchronous machines can be used to give very good predictions of the performance of linear machines.

In Reference 1.5 conventional salient-pole theory was used to develop a model for the heteropolar transverse-flux linear synchronous machine. The theory was based on the principle of superposition and thus could not take into account the non-linearity of the iron in the magnetic circuit. In order to use the minimum weight of iron the magnetic circuit should be worked at as high a flux density as possible. This inevitably means that the non-linearity of the characteristics of the magnetic material must be introduced into the model.

One approach to the introduction of non-linearity was devised by Kilgore[1.7]. He resolved the synchronous reactances into two components using the principles of superposition. Empirical constants were obtained from tests and used to modify the axis reactances. A more rigorous determination of the axis reactances was developed in Reference 1.8 that utilised two-dimensional, non-linear flux plots. One purpose of the

work described in this thesis is to improve further the calculation of synchronous machine constants by employing a three-dimensional, non-linear flux plotting method.

Production of flux plots using computers has a relatively short history. In 1960 Mamak and Laithwaite[1.9] suggested using a relaxation method for solving machine field problems. Finite-difference equations based on the magnetic vector potential were used. The solution was in two dimensions only, with the assumption that the permeability of the iron was infinite. The distribution of vector potential in a 2-dimensional field, in which permeabilities depend on field quantities, was found numerically by Ahamed[1.10] using a finite-difference method. He applied Stokes' theorem to Maxwell's equations to modify Southwell's relaxation technique in order to accelerate convergence of the numerical solution. This was necessary because the permeabilities of two adjoining regions, in the electromagnetic field, may vary considerably leading to extremely slow convergence. He also suggested that an under-relaxation of permeabilities would be desirable for avoiding undamped oscillations.

The saturation of magnetic materials, which were assumed to be isotropic, was accurately taken into account by Fuchs and Erdelyi[1.8] in a 2-dimensional problem. This method was based on vector potential and used difference equations with a two-step iteration technique. In the first iteration step, the vector potentials were found by using successive line over-relaxation with the assumption that the reluctivities were recalculated and under-relaxed after the new vector potentials were found.

Silvester and Chari[1.11] applied a finite element method for the solution of nonlinear 2-dimensional magnetic field problems. Their calculation method was based on a discrete representation of the magnetic field problem using finite elements with nonvarying properties within the elements. They derived finite difference equations for the entire problem in terms of the potentials at the vertices of the finite elements. Within each element the vector potential was a linear function of the vertex potentials. In their solution, the nonlinear part of the calculation was performed using the Newton-Raphson method, whereas Gaussian triangular decomposition was used to solve the linear equations.

In the methods described in References (1.8), (1.9) and (1.11) the reduction of the problem to two dimensions required that only a small number of equations need be solved. In the case of rotating machines, a 2-dimensional representation means that the contribution of the leakage flux of the end windings is neglected. In addition to this the geometry of linear synchronous machines is complex, so that an accurate prediction of performance requires 3-dimensional flux distributions to be calculated. When using vector potential formulations in 3D it is necessary to calculate the three components at each point. This greatly increases the number of equations that have to be solved. Carpenter[1.12] overcame this difficulty by using a scalar potential formulation that requires only one equation per field point. In order to represent large section conductors the field strength distribution that they produced was first calculated. This was then incorporated into the main scalar potential solution.

Recently, three dimensional field problems have been solved numerically by using a finite element formulation[1.13]. This method is used to best advantage when the solution is in terms of scalar potential, since one unknown per nodal point is required. If vector potential were used the use of three equations per node would be necessary. The finite element method is very useful for solving problems that have complicated boundary contours. When finite difference methods are used a large number of extra nodes are generated.

When scalar potential is the unknown quantity there may be a loss of accuracy in highly permeable regions[1.13]. This is due to cancellation between the field due to the conductors and that due to the scalar potentials. It has been shown[1.14] that this problem can be avoided by using two separate regions. One of the regions contains the high permeability material only. The other region has a relative permeability of value 1 and contains the conductors.

In the following Chapter, the equations required for a numerical computation of the magnetic field within a homopolar linear synchronous machine are derived. The distribution of the field in three dimensions is considered and the non-linearity of the iron parts is included. The resulting set of linear simultaneous equations are solved using the successive over-relaxation technique.

In Chapter 3 the inductances of the machine are found by a flux linkage method using the flux densities computed in Chapter 2. Simple formulae, ignoring iron reluctance, are also derived. These are used to check the inductance obtained from the 3D field calculation. The inductance formulae can also be used for producing first designs for a homopolar machine. In Chapter 4, various methods for calculating the forces acting between the stator and rotor of the homopolar LSM are

given, and the flux densities from Chapter 2 are also used in this calculation. The calculated values of Chapters 3 and 4 are compared with those obtained from experimental work in Chapter 5 to confirm the validity of the numerical method.

Chapter 6 gives a comparison between heteropolar[1.5] and homopolar machines. This was performed on an experimental basis and was described at a recent Institution of Electrical Engineers Colloquium[1.15]. Part of this work regarding the calculation of 3-dimensional field solutions was also described at an IEE Colloquium[1.16].

References

1.1 Eastham, J.F.:
"Iron-cored linear synchronous machines", Electronics and Power, 1977, 23, pp.239-242.

1.2 Levi, E:
"Linear synchronous motors for high speed ground transportation", IEEE Trans., MAG-9, pp.242-248.

1.3 Laithwaite, E.R.:
"Linear induction motors", Proc.IEE, 1957, 104(A), (12), pp.461-470.

1.4 Laithwaite, E.R.:
"Induction Machines for Special Purposes", (Newnes, 1966).

1.5 Balchin, M.J. and Eastham, J.F.:
"Characteristics of a heteropolar linear synchronous machine with passive secondary", IEE J. Electr. Power, Appl.(GB), Vol.2, No.6, pp.213-218, Dec. 1979.

1.6 Eastham, J.F. and Laithwaite, E.R.:
"Linear motor topology", Proc.IEE, 1973, 120(3), pp.337-343.

1.7 Kilgore, L.A.:
"Calculation of synchronous machine constants", Trans.AIEE, Vol.50, pp.1201-1213, 1931.

1.8 Fuchs, E.F. and Erdelyi, E.A.:
"Determination of waterwheel alternator steady-state reactances from flux plot", IEEE Summer Power Meeting, July 1971, pp.2510-27, Paper No. TP596.

1.9 Mamak, R.S. and Laithwaite, E.R.:
"Numerical evaluation of inductance and ac resistance with particular reference to electrical machines", Proc.IEE, Vol.108C, pp.252-258, Nov. 1960.

1.10 Ahamed, S.V.:
"Accelerated convergence of numerical solution of linear and non-linear vector field problems", Computer Journal, Vol.8, No.1, April 1965, pp.73-76.

1.11 Silvester, P. and Chari, M.V.K.:
"Finite element solution of saturable magnetic field problems", IEEE Trans., PAS-Sept/Oct, 1970, Vol.89, No.7, pp.1642-1651.

1.12 Carpenter, C.J.:
"Numerical solution of magnetic fields in the vicinity of current carrying conductors", Proc.IEE, Vol.114, No.11, Nov. 1967, pp.1793-1800.

1.13 Zienkiewicz, O.Z., Lyness, J. and Owen, D.R.J.:
"Three dimensional magnetic field determination using a scalar potential - a finite element solution", IEEE Trans. Magnetics, Vol.MAG-13, No.5, Sept. 1977, pp.1649-1656.

1.14 Simkin, J. and Trowbridge, C.W.:
"On the use of the total acalar potential in the numerical solution of field problems in electromagnetics", International Journal for Numerical Methods in Engineering, Vol.14, 1979, pp.423-440.

1.15 Balchin, M.J., Helani, M.F. and Eastham, J.F.:
"A comparison of the chracteristics of heteropolar and homopolar linear synchronous motors", Colloquium on Linear Synchronous Machines for Magnetically Levitated Vehicles, London, England, 4 Feb. 1983 (London, England: IEE 1983), p.3/1-4.

1.16 Balchin, M.J., Davidson, J.A.M. and Helani, M.F.:
"Application of network field solution methods to AC machine problems", Colloquium on Finite Element Methods Applied to Electrical Machines, London, England, 7 March 1983 (London, England: IEE 1983), p.7/1-4.

CHAPTER TWO

Three Dimensional Magnetostatic Flux Calculations for a Homopolar Linear Synchronous Machine Including Iron Nonlinearities

2.1 Introduction

The basic equations of magnetostatics are obtained from Maxwell's equations[2.1]

$$\text{curl } H = J \qquad 2.1.1$$

$$\text{div } B = 0 \qquad 2.1.2$$

These equations are connected by the constitutive relation

$$B = \mu H \qquad 2.1.3$$

where μ is a non-linear function of the field intensity H in permeable materials. In the magnetostatic problem, H has three components[2.2], and the parameter μ can be found to be

$$\mu = \mu(|H|)$$

with 2.1.4

$$|H| = \sqrt{H_x^2 + H_y^2 + H_z^2}$$

where $|H|$ is an absolute value of the field intensity, and H_x, H_y and H_z represent the mean value of H in the directions x, y and z respectively when Cartesian co-ordinates are used. In two dimensional problems H_z will be zero when the network exists in the x-y plane. The calculation of $|H|$ will be described in more detail in section 2.5.

2.2 Derivation of Network Element

The magnetic medium of a three dimensional problem can be replaced by a set of rectangular brick elements. Each brick is connected to its six immediate neighbours by sharing a common face.

A typical brick element is shown in Fig.2.2.1. The material within the element is assumed to be isotropic and its permeability (μ) is a function of the magnetic field strength as indicated by equation 2.1.4.

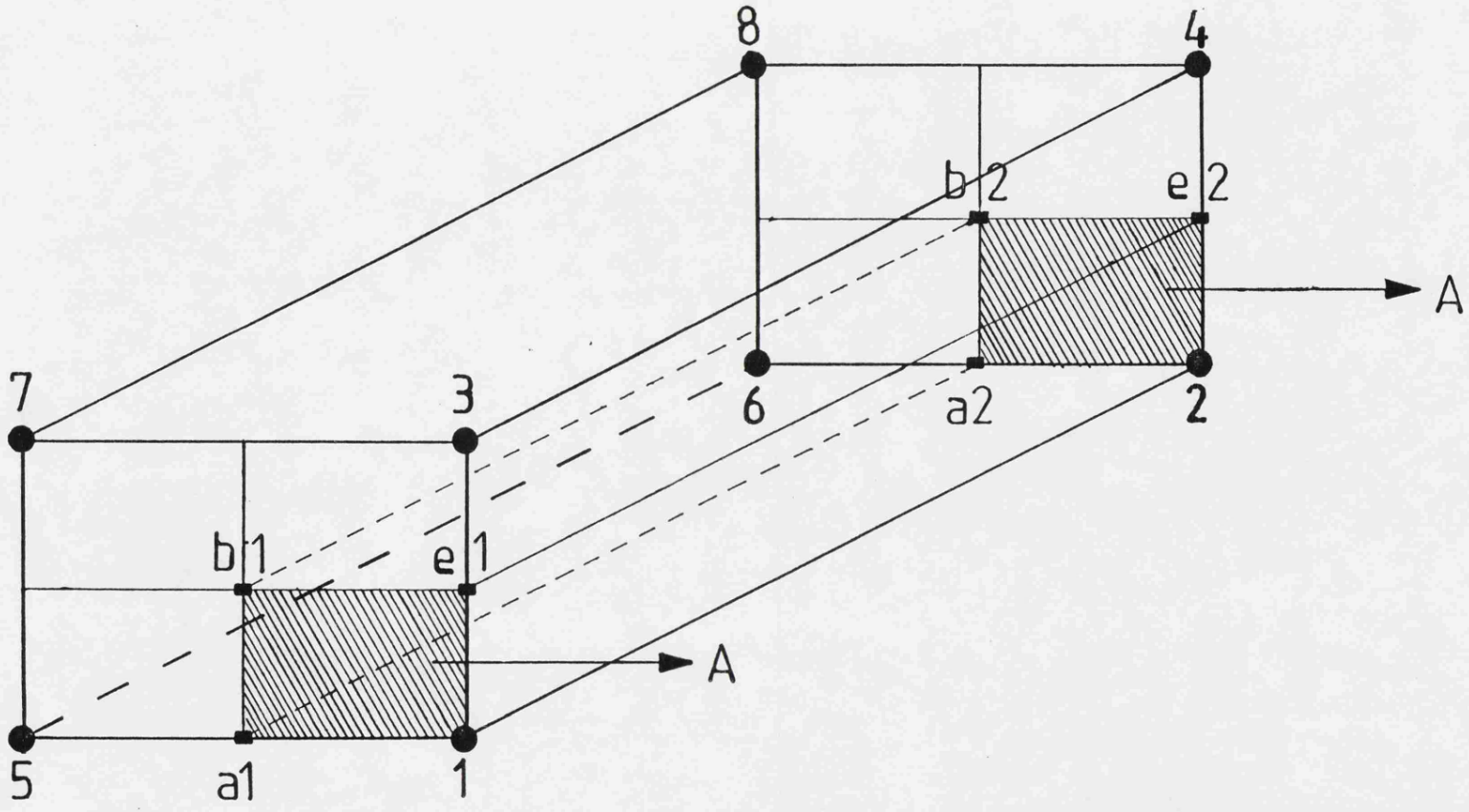

Fig 2·2·1 : RECTANGULAR BRICK ELEMENT

A component of flux density is associated with each of the element edges. There are four edge elements in a brick in each of three directions. In order to assign a flux to each of the 12 edges, it is necessary to consider the geometric properties of the element. The brick element 1-8 is divided into four smaller brick elements in the z-direction as $1\text{-}a_1\text{-}b_1\text{-}e_1\text{-}2\text{-}a_2\text{-}b_2\text{-}e_2$ shown in Fig.2.2.1. The edges b_1e_1 and b_2e_2 intersect the surface 1-2-3-4 normally and likewise the edges b_1a_1 and b_2a_2 intersect the surface 1-2-5-6 normally. The areas A are rectangular surfaces and intersected normally by edge 1-2.

Practical magnetic field problems usually involve current sources so that the total field H can be expressed as the sum of the field for sources H_s and the field from the magnetization H_m(2.2). The following relation can be written

$$H = H_m + H_s \qquad 2.2.1$$

taking the curl on both sides of this equation gives

$$\text{curl } H = \text{curl } H_m + \text{curl } H_s \qquad 2.2.2$$

but in a current free region(2.3)

$$\text{curl } H_m = 0 \qquad 2.2.3$$

This equation allows the introduction of a potential function V and that H_m is its gradient i.e.:

$$H_m = -\nabla V \qquad 2.2.4$$

From equations 2.1.1, 2.2.2 and 2.2.3

$$\text{curl } H_s = J \qquad 2.2.5$$

and substituting for H from equation 2.2.1 in the constitutive equation 2.1.3 gives

$$B = \mu(H_s + H_m) = \mu H \qquad 2.2.6$$

In order to illustrate the development of the branch relations the edge between nodes 1 and 2 in Fig.2.2.1 will be considered. It is assumed that the components of the B and H vectors are parallel to edge 1-2, are constant over area A and are also constant between points 1 and 2. The field components within the region $1\text{-}a_1\text{-}b_1\text{-}e_1\text{-}2\text{-}a_2\text{-}b_2\text{-}e_2$ are those associated with edge 1-2. Thus the flux through area A will be

$$\phi_{12} = BA = \mu A(H_s + H_m) \qquad 2.2.7$$

If equation 2.2.5 holds then the line integral of H_s between two points 1 and 2 may be written

$$\int_1^2 H_s \, d\ell = H_s \, \ell_{12} = \mp m_{12} \qquad 2.2.8$$

The sign of m_{12} depends on the orientation of branch 1-2 and this point will be discussed further in section 2.6.3. The magnitude of the mmf source m_{12} is equal to the amount of current circulating around edge 1-2.

The line integral of equation 2.2.3 between points 1 and 2 defines the potential difference between these nodes, i.e.

$$\int_1^2 H_m \, d\ell = H_m \, \ell_{12} = V_{12} \qquad 2.2.9$$

where V_{12} is the potential difference existing between the points 1 and 2 i.e.:

$$V_{12} = V_1 - V_2 \qquad 2.2.10$$

Substituting H_s and H_m from equations 2.2.8 and 2.2.9 respectively into equation 2.2.7 gives

$$\phi_{12} = \frac{\mu A}{\ell_{12}} (\mp m_{12} + V_{12}) \qquad 2.2.11$$

In this equation the quantity $\mu A/\ell_{12}$ represents the permeance that admits the flow of flux through area A in Fig. 2.2.1, i.e.

$$P_{12} = \frac{\mu A}{\ell_{12}}$$

When this is substituted in equation 2.2.11, the result is

$$\phi_{12} = P_{12} (\mp m_{12} + V_{12}) \qquad 2.2.12$$

It is convenient to represent this equation by means of an equivalent circuit as shown in Fig. 2.2.2. This circuit in fact represents the branch existing between points 1 and 2. The procedure described in this section is repeated at each of the element edges.

2.3 Complete Magnetic Field Model

In the previous section the complete magnetic field was replaced by a set of rectangular brick elements such as that shown in Fig. 2.2.1. Each edge of each element consists of an equivalent circuit of the type shown in Fig. 2.2.2. In the complete model, there will be a number of circuit branches connected in parallel along each element edge. The permeability of the material contained within each brick need not necessarily be the same as that in an adjacent element. Boundary conditions can therefore be imposed at the interfaces between elements.

The curl equations 2.1.1, 2.2.3 and 2.2.5 are equivalent to the following line integrals:

$$\oint_L H d\ell = I \qquad 2.3.1$$

$$\oint_L H_m d\ell = 0 \qquad 2.3.2$$

$$\oint_L H_s d\ell = I \qquad 2.3.3$$

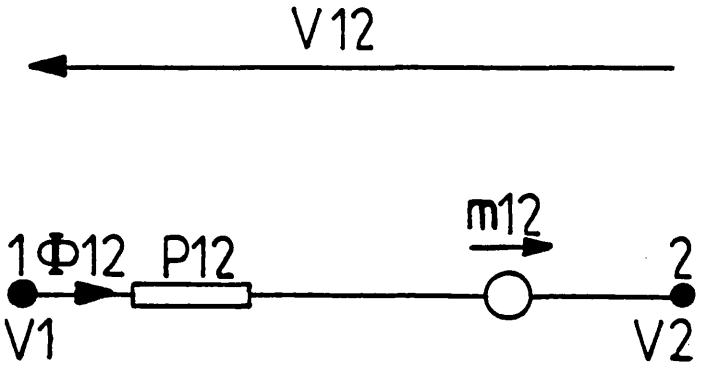

Fig 2·2·2 : ELEMENT OF MAG-NETIC FIELD MODEL

where L is a closed path traced along edges of the complete magnetic field model. Equation 2.3.2 indicates that the sum of potential differences along all the edges which form the closed path is zero. Thus the interconnection of equivalent circuits like that in Fig. 2.2.2 in a closed path is justified if the potential V_{12} is chosen to be the branch potential difference. Equation 2.3.3 indicates that the sum of source potential differences over all edges which form the closed path will be equal to the enclosed current. In this case the inter-connection of equivalent circuit such as in Fig. 2.2.2 in a closed path is justified if m_{12} is chosen to be a source quantity for the branch.

The divergence equation 2.1.2 is equivalent to the following surface integral

$$\oint_S B_n dS = 0 \qquad 2.3.4$$

where B_n is the flux density normal to a closed surface S surrounding each node or vertex of the complete discretization of the magnetic field. A surface such as S is formed by a number of areas each as A in Fig. 2.2.1. The flux through the areas A is the branch flux so that the inter-connection of equivalent circuits such as in Fig. 2.2.2 at any node or vertex is justified if the flux ϕ_{12} is chosen to be the branch flux.

2.4 Method of Solution of the Network Model

The solution of the network model for both two and three dimensional problems is based on equation 2.3.4. This can be written for any node J as:

$$\sum_{K=1}^{N_b} \phi_{JK} = \oint_S B_n dS = 0 \qquad 2.4.1$$

where N_b is a number of branches which are connected to node J.

Substituting for the flux ϕ_{JK} from equation 2.2.12 into equation 2.4.1 gives:

$$\sum_{K=1}^{N_b} \phi_{JK} = \sum_{K=1}^{N_b} P_{JK} (\mp m_{JK} + V_{JK}) = 0 \qquad 2.4.2$$

From equations 2.2.10 and 2.4.2 the following nodal equation can be obtained:

$$\sum_{K=1}^{N_b} P_{JK} (\mp m_{JK} + V_J - V_K) = 0 \qquad 2.4.3$$

2.5 Solution of Nonlinear Problem

In the network model described in sections 2.2-2.4 linear behaviour has been assumed. This means that there is no change in permeability with field strength. The formulation is, however, valid for the general non linear case. The governing equations 2.4.3 are valid for variation of permeability but an iterative solution is now necessary. The solution method is explained in the following subsections:

a) A linear solution using estimated starting values of μ and node potentials is performed to calculate the potentials at all nodes in the network model. The method used is that of successive over relaxation. Throughout each S.O.R. iteration, potentials are increased to give zero flux into a node. As each node potential is reset it obviously upsets the node equations for the neighbouring nodes. To accelerate the convergence of the iteration the node potentials are not updated to a value which satisfies the node equation 2.4.3, but instead the required change is over-corrected by a factor "ALPHA" i.e. the new node potential V_{n+1} becomes:

$$V_{n+1} = V_n + \text{ALPHA x change} \qquad 2.5.1$$

where n is the iteration number. The value of accelerating factor ALPHA depends on the nature of problem to be solved. The method is always convergent for ALPHA = 1, i.e. no over relaxation, and always divergent for ALPHA = 2. Best convergence is obtained for some value between these two limits, i.e.

$$1.0 < \text{ALPHA} < 2.0$$

b) When convergence of the S.O.R. solution has been obtained, the potentials are used to adjust the element permeability using equation 2.1.4. This is done by first calculating the field strength along the edges of each element. For example between nodes 1 and 2 in Fig. 2.2.1 the field strength will be

$$H_{12} = \frac{m_{12} + V_{12}}{\ell_{12}} \qquad 2.5.2$$

Since the element is rectangular a set of four edges will be parallel to each coordinate direction. The field strength in this direction is taken to be the mean value of the four edge field strength values.

In order to illustrate the calculation of H, equation 2.5.2 will be evaluated at each of the elements shown in Fig. 2.2.1.

For direction x

$$H_{51x} = \frac{m_{51} + V_{51}}{\ell_{51}} \qquad H_{62x} = \frac{m_{62} + V_{62}}{\ell_{62}}$$

$$H_{73x} = \frac{m_{73} + V_{73}}{\ell_{73}} \qquad H_{84x} = \frac{m_{84} + V_{84}}{\ell_{84}}$$

$$H_x = \frac{H_{51x} + H_{73x} + H_{62x} + H_{84x}}{4}$$

For direction y

$$H_{13y} = \frac{m_{13} + V_{13}}{\ell_{13}} \qquad H_{24y} = \frac{m_{24} + V_{24}}{\ell_{24}}$$

$$H_{57y} = \frac{m_{57} + V_{57}}{\ell_{57}} \qquad H_{68y} = \frac{m_{68} + V_{68}}{\ell_{68}}$$

$$H_y = \frac{H_{13y} + H_{57y} + H_{24y} + H_{68y}}{4}$$

For direction z

$$H_{21z} = \frac{m_{21} + V_{21}}{\ell_{21}} \qquad H_{87z} = \frac{m_{87} + V_{87}}{\ell_{87}}$$

$$H_{43z} = \frac{m_{43} + V_{43}}{\ell_{43}} \qquad H_{65z} = \frac{m_{65} + V_{65}}{\ell_{65}}$$

$$H_z = \frac{H_{21z} + H_{43z} + H_{87z} + V_{65z}}{4}$$

The absolute value of H is then calculated using equation 2.1.4.

An experimentally obtained B-H curve is used to calculate the permeability μ for a given H in each brick element. The curve is represented by a number of straight-line segments joining each of the measured B and H values. When the particular segment corresponding to the known $|H|$ value has been located the flux density is calculated using[2.4]

$$|B| = B_J + \frac{1}{m_J}(|H| - H_J) \qquad 2.5.3$$

where

$$m_J = \frac{H_{J+1} - H_J}{B_{J+1} - B_J}$$

$$H_J < |H| < H_{J+1}$$

and J is a point of B-H curve. The new value of element permeability is then calculated using equations 2.1.3 and 2.5.3, i.e.

$$\mu = \frac{B_J + (|H| - H_J)/m_J}{|H|}$$

c) The node potentials obtained from step (a) and the branch permeances calculated from step (b) are used as starting values for step (a). After the linear solution converges the new node potentials are again used in step (b) to calculate new permeances. This procedure is repeated until the nonlinear solution converges.

d) When convergence has been obtained the node potentials and branch permeances are used to calculate the branch fluxes. Flux densities are calculated using equation 2.2.12 with appropriate areas.

2.6 Procedure for Setting up the Network Model in a Practical Problem

2.6.1 Subdivision of region to be modelled

It is first necessary to let the magnetic field region be subdivided into rectangular brick elements ensuring only that all air-iron interfaces coincide with element faces. Subdivision throughout a region depends on the rate of change of the field expected at each point. If this is high then many small elements must be used. Following subdivision, the elements are replaced by their equivalent circuit models as described in sections 2.2 and 2.3. It is necessary to set an exterior boundary round the region of interest to limit the extent of the magnetic

subdivision. The exterior boundary normally takes the form of a flux plane or an equipotential surface and should be far enough away so as not to be significant in the solution. In the network model, planes are represented by open circuits and equipotential surface by short circuits. Planes of positive or negative symmetry are treated as external boundaries in the manner just described.

The next step is to give a number to all branches and nodes of the network model using an arbitrary numbering scheme. An arbitrary positive direction is given to the flow in all branches. This defines a start and finish node for each branch with the positive flow from the start node to the finish node. Three arbitrary numbers are given to all branches in three dimensional network model depending on whether the branch lies in the x, y or z direction. Also an arbitrary datum node number is specified in the network model. It is preferable to make this datum node the one to which most branches are connected. Finally, all elements are given a number. This is used to distinguish whether they contain iron or air.

All known sources in the field, such as winding currents, are transformed into known branch sources. For a magnetic field in which the currents are specified the normal method of making the transformation is to use the tearing principle[2.5]. This is used to relate the branch mmf sources to the current that circulates around the branch. If this current tends to induce positive flux in the branch, the sign of the mmf generator is positive. If negative flux is induced, the sign of mmf should be negative.

2.6.2 Choice of the set of independent voltage variables

The next step after the equivalent circuit model has been formed and numbered is to choose an appropriate set of independent voltage variables for the network to be solved. This is in fact the node-to-datum set of voltage variables. The procedure is to choose the potential of one node (the datum node) as a reference and designate as variables the potentials of the remaining nodes with respect to this reference. A computer program is used to set up a list of all node numbers in relaxation order, and also to set up a list of branches connected to each node.

2.6.3 Choice of sign for branches connected to each node

When the branches connected to each node in the equivalent circuit are defined, the next step is to choose the sign for each of them. This is done by taking each node of the network to be a datum node for all branches connected to it. Each of these branches will be terminated at a particular node such as K. The branch sign is set as +1 if node K represents a start point, or as -1 if K is the finish node of this branch. The same procedure is performed for all the branches connected to each node. All the signs together with the node number (K) are then stored in a linked list form.

2.6.4 Construction of the NCOM matrix

To evaluate the permeabilities from equations 2.1.4 and 2.5.2, and then the permeances for all branches, it is necessary to list all the branches in each brick element containing magnetic material and also all their directions. This is done by searching the input data of the network model using a computer program. The branch and magnetic material data are stored in a matrix (NCOM). A number is given to all branches to

define whether the branch is in the x, y or z direction. The matrix NCOM is arranged to have columns corresponding to the total number of branches and rows corresponding to all elements containing magnetic material. The first number of each row of matrix NCOM is a number of a certain brick element, and the remaining numbers of this row represent x, y and z components of field intensity H for this element. The average value of H_x, H_y and H_z for each brick element is determined using equation 2.5.2 with the aid of matrix NCOM, and the absolute value of H is then found from equation 2.1.4.

Once the field intensity H and the permeability μ have been found for each brick element, the next step is to calculate a branch permeance for all branches of the network model. These permeances are used in node equation 2.4.3 for each step of the nonlinear iteration which is discussed in section 2.5 of this chapter.

2.7 Nonlinear Three Dimensional Magnetic Field Solution for a Homopolar Linear Synchronous Machine (LSM)

2.7.1 Introduction

To demonstrate the validity of the network field model described in previous sections, the programme TESTF was written to find the magnetic induction in a homopolar linear synchronous machine. This LSM is a new form of iron-cored linear synchronous machine which has been described by Eastham[2.6]. It is described in detail in Chapter 1.

The calculated flux density within the LSM is compared with measured values. Air-gap densities due to field and armature in both the d-axis and q-axis are obtained. These fluxes are used in the next chapters for the predetermination of the LSM performance characteristics.

2.7.2 Assumptions

The analysis is treated as a magnetostatic non linear three dimensional problem. Simplifying assumptions are necessary in order to keep the storage and time as small as possible but maintain acceptable accuracy. These assumptions are as follows:

1. The analysis is confined to a part of the LSM which is symmetrical and periodic. The plane of symmetry is shown in Fig. 2.7.1(a). The periodic length is chosen as two pole-pitches.

2. The curvature of the machine is not considered. Also the cross section of the slots and the teeth are assumed to be rectangular.

3. The stator was constructed using grain-oriented steel laminations. In the limbs carrying the ac windings the major part of the flux path is at 90^{o} to the rolling direction. In the bridging limb the flux passes mainly in the direction of rolling. The use of a separate B/H curve for each of these parts is therefore necessary. The magnetic material in both stator and rotor is assumed to be isotropic and its saturation curve is single valued; i.e. hysteresis effects are not considered. Magnetization curves of the materials of stator are established by measurements which will be described in detail in chapter five.

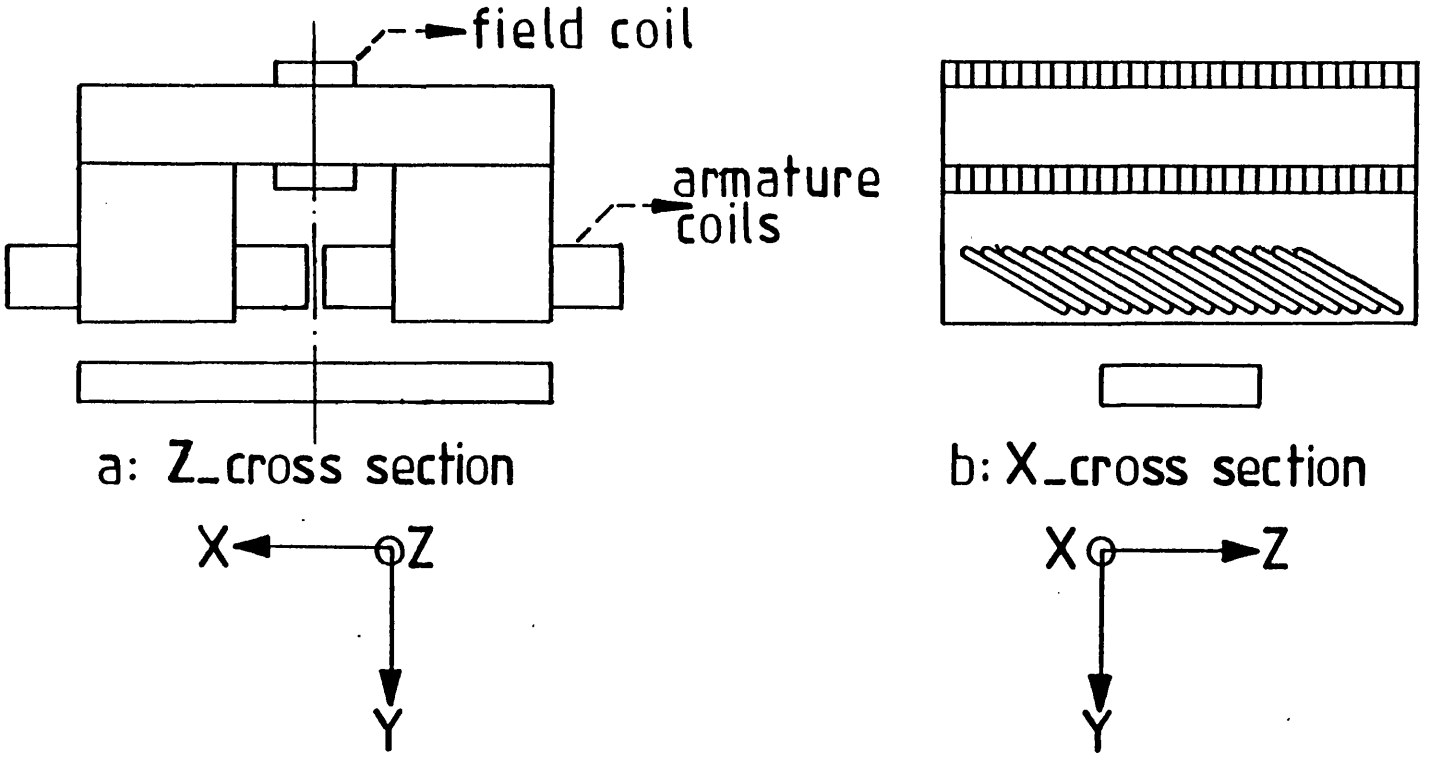

Fig 2·7·1 : Homopolar LSM cross sections

4. The current in the ac winding is assumed to be "frozen". The analysis of the machine, when the three-phase windings are excited with ac, is carried out at the instant when the red-phase is carrying zero current. The end turns of the windings are represented in the model.

5. There are transient currents induced in the rotor poles as they pass under the machine. The effect is ignored although it could be appreciable at high speeds.

2.7.3 Sub-division of the LSM region to be modelled

The cross sections of the linear homopolar synchronous machine are shown in Fig.2.7.1. The magnetic field region of the LSM is subdivided into rectangular brick elements such that all interfaces between different types of material coincide with faces. The subdivision of the cross-section is shown in Fig.2.7.2. To limit the extent of the subdivision, an exterior boundary taking the form of a flux plane is used for all sides. except the plane of symmetry. This is represented by an equipotential plane. All brick elements in the air are given the number "0", and those in the iron region different arbitrary numbers. The elements from number 1 to 8 are those in which the flux is passing parallel to the direction of rolling.In elements 9 to 12 the flux is passing perpendicular to the direction of rolling.

In two poles of the LSM there are twelve teeth and twelve slots. In order to model this, twenty four z-cross sections are used. The odd numbered sections contain the teeth, and the even contain the slots. For cross-sections containing teeth the elements numbered 13, 14, 15 and 16 contain iron through which the flux is passing out 90^{o} to the rolling direction. When the cross-section contains slots elements 13 to 16 will be given the number "0".

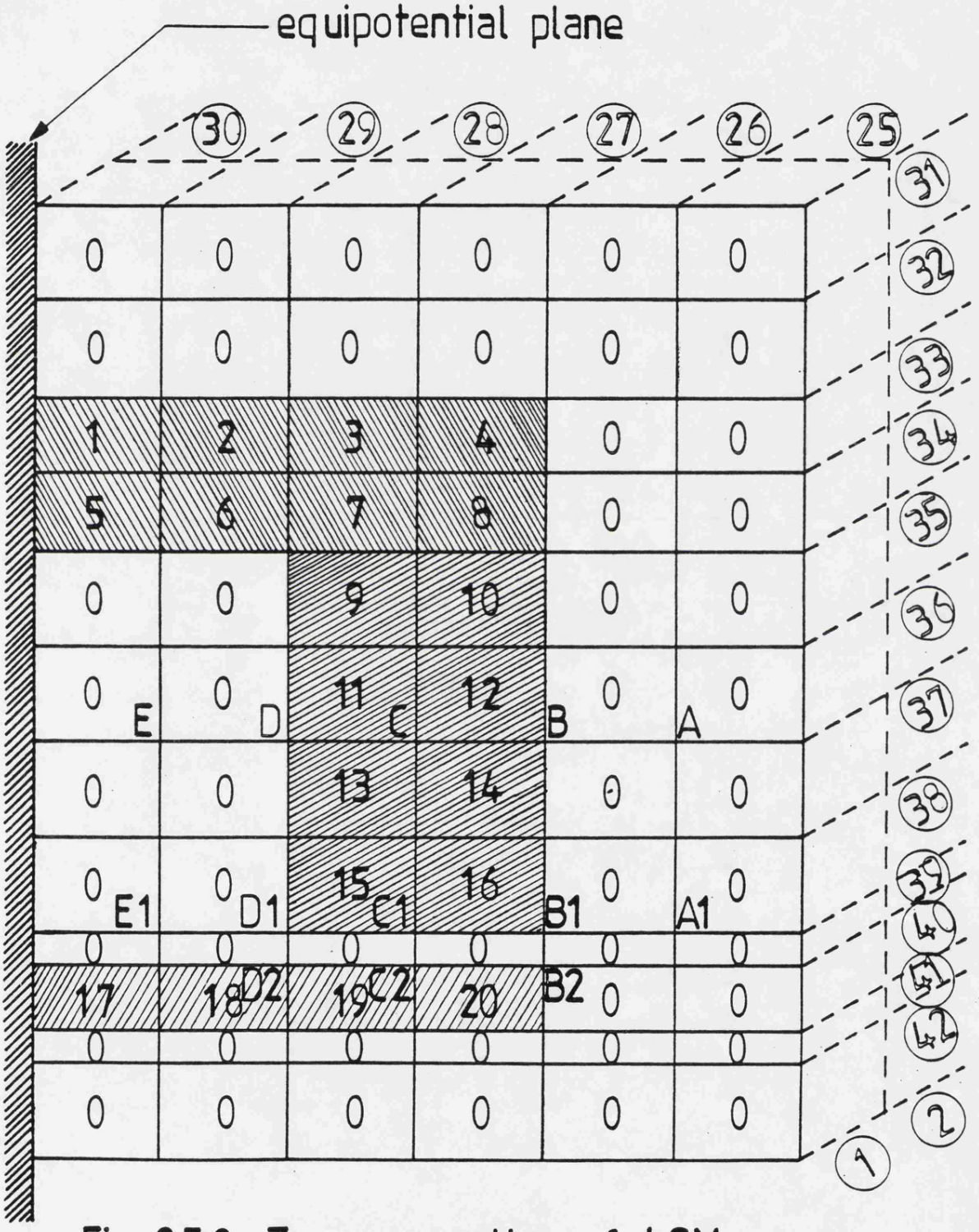

Fig 2·7·2 : Z_cross section of LSM
(1st plane)

In the d-axis position the rotor iron appears in the 9th to 16th z-cross sections. In the q-axis position the rotor iron is in planes 3 to 10. The network need be set up only once if the assumption is made that the rotor iron exists in all z-cross sections. The number "0" is then given to elements which are actually air. To explain this procedure, consider the rectangular region shown in Fig. 2.7.3. This region is subdivided into 12 parts. Arbitrary numbers such as 1,2,3,....,11, and 12 are given to indicate that these elements contain iron. In stage (a) elements numbered 1 to 4 contain iron. The elements 5 to 12 are renumbered zero. When the iron parts are moved to the right, as shown in in stage (b) of Fig. 2.7.3, the numbers 1, 2 and 3 are changed to "0" and three of the elements which were previously numbered zero are now labelled 5, 6 and 7. This process is continued in order to move the rotor progressivly to the right.

The numbers 17 to 20 in Fig.2.7.2 indicate the elements containing rotor iron. The numbers in small circles at the top and right of Fig.2.7.2 indicate the numbering of the x-cross sections and the y-cross sections.

The second z-cross section is the same as the first except that the elements numbered 13 to 16 will be renumbered "0" because there is now a slot as shown in Fig.2.7.4. In this figure the elements numbered 21 to 28 pass flux in the rolling direction (0^{o}). Elements numbered 29 to 32 indicate those brick elements in which the flux passes at 90^{o} to the rolling direction. Elements numbered 33 to 36 are those containing rotor iron. Similar descriptions apply for all the z-cross sections (numbered 3 to 24).

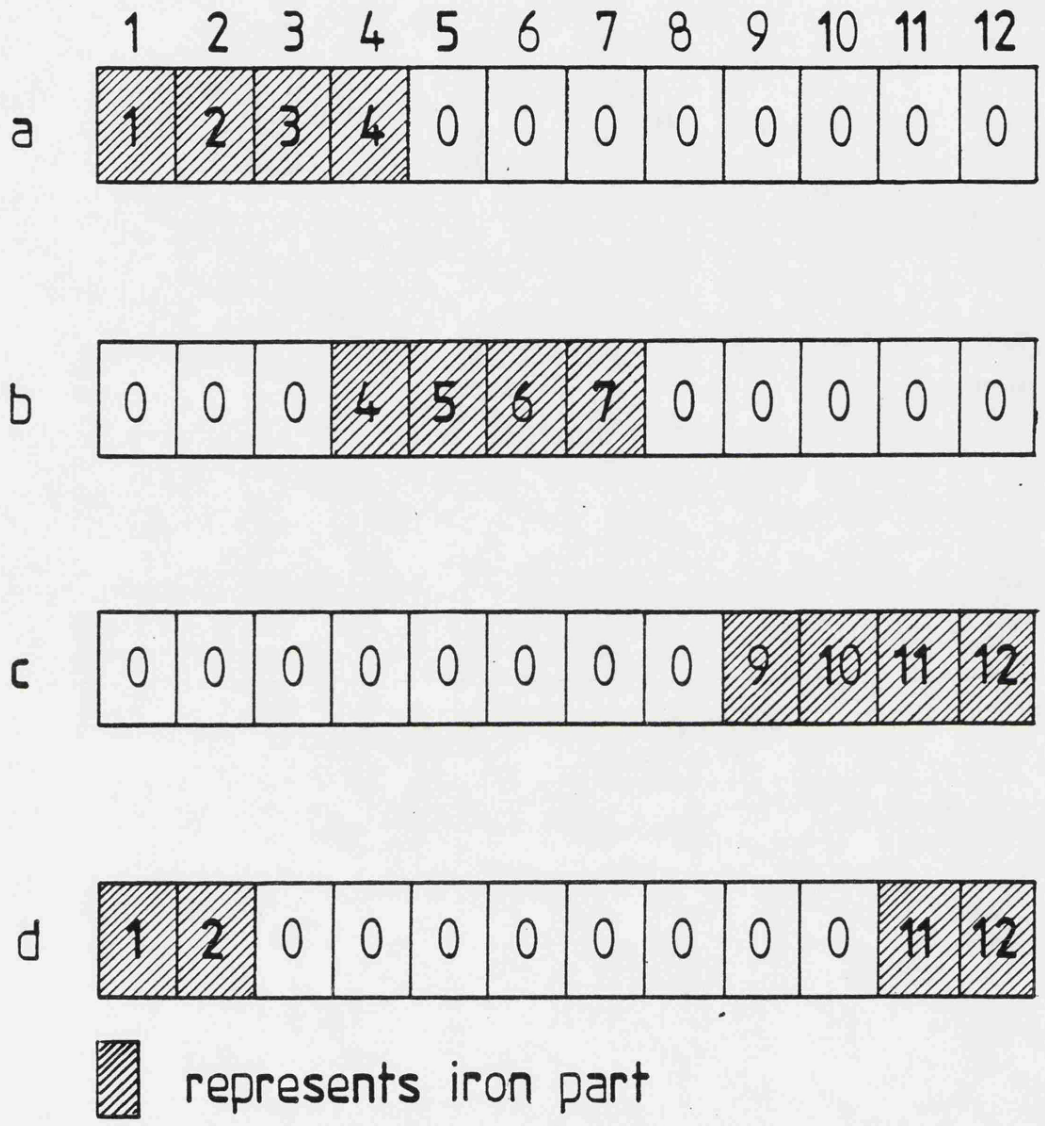

Fig 2·7·3 : representation of different rotor iron positions .

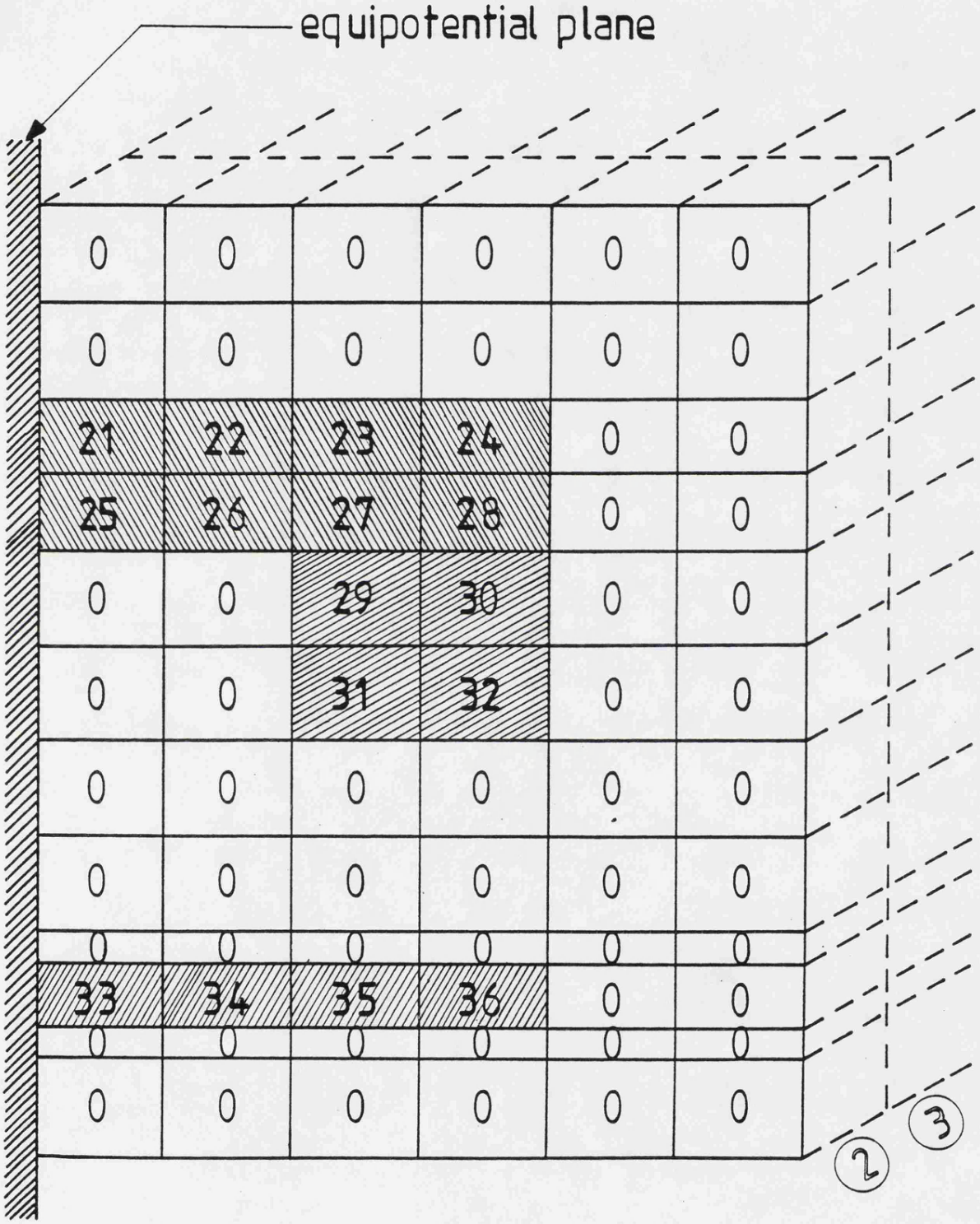

Fig 2·7·4 : Z_cross section of LSM
(2nd plane)

The x and y cross sections are set up in a similar way. Fig.2.7.5 shows the 27th x-cross section and Fig.2.7.6 shows the 38th y-cross section.

Once the brick elements have been numbered the next step is to give numbers to all the nodes. All the edges of the elements are replaced by equivalent circuits which are similar to that of Fig.2.2.2. These circuits or branches are also numbered. The area of each branch can easily be calculated with the aid of cross section diagrams in which this branch exists. The length of a branch must be equal to the depth of the cross section.

The complete set of data for the solution of the homopolar linear synchronous machine has 42 cross sections. The numbers of branches, nodes, and brick elements containing iron are 9893, 1873 and 368 respectively.

2.7.4 Equivalent mmf sources for LSM network

The "tearing" technique[2.5] is used to transform all winding currents into branch mmf sources. In each magnetic branch of the network cut by current an mmf source equal in magnitude to that current is inserted. The sign of the mmf source is positive if the current tends to induce positive flux, i.e. flux in the assumed direction as indicated in Fig.2.2.2.

2.7.4.1 Transformation of the field winding current

The field winding of the LSM is a dc coil and it is placed on the primary member as shown in Fig.2.7.1. The transformation of the field winding current is illustrated in Fig.2.7.7(a). Each coil of the field winding carries a current equal to $(Z_f I_f/2)$, where Z_f is a number of

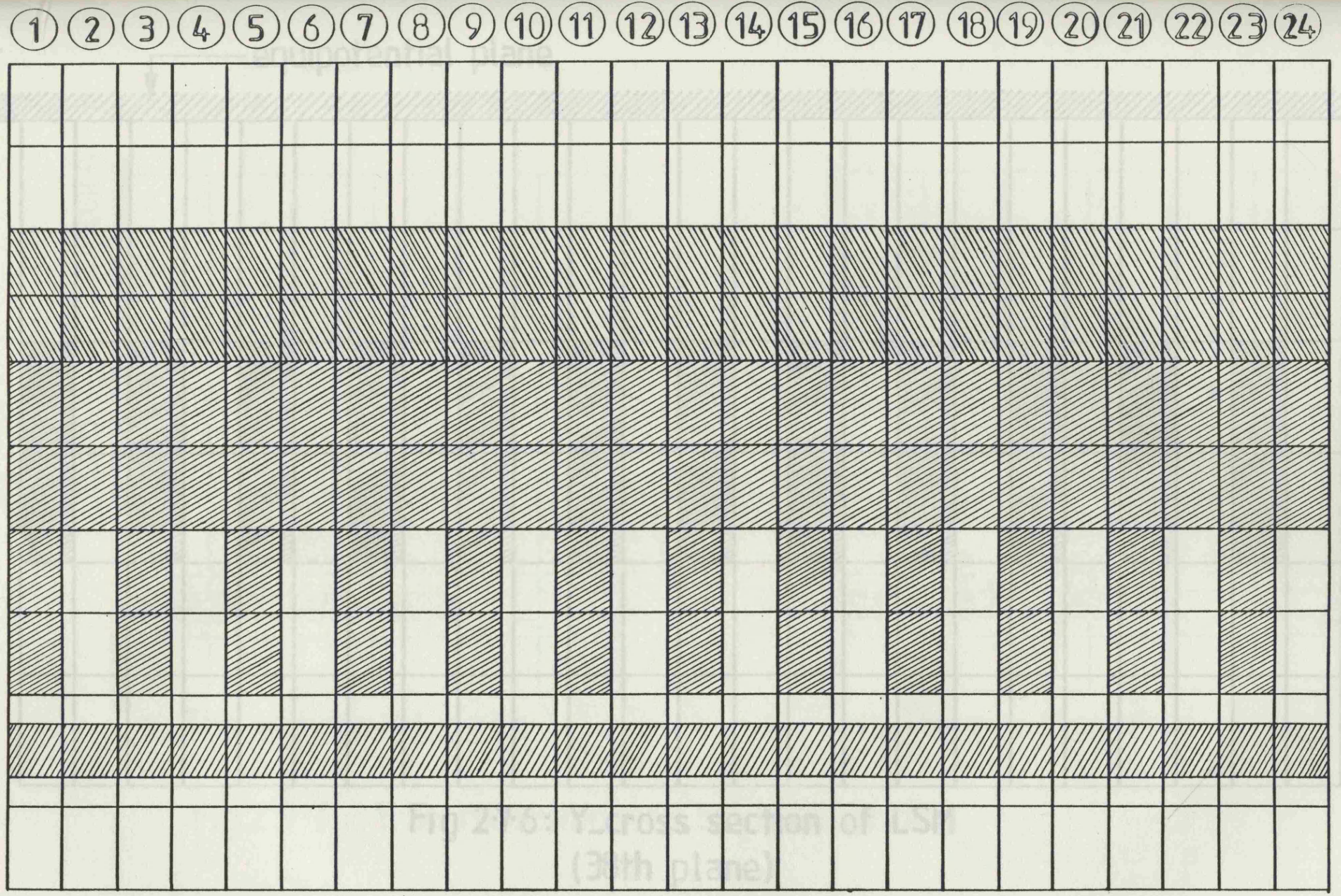

Fig 2·7·5: X_cross section of LSM
(27th plane)

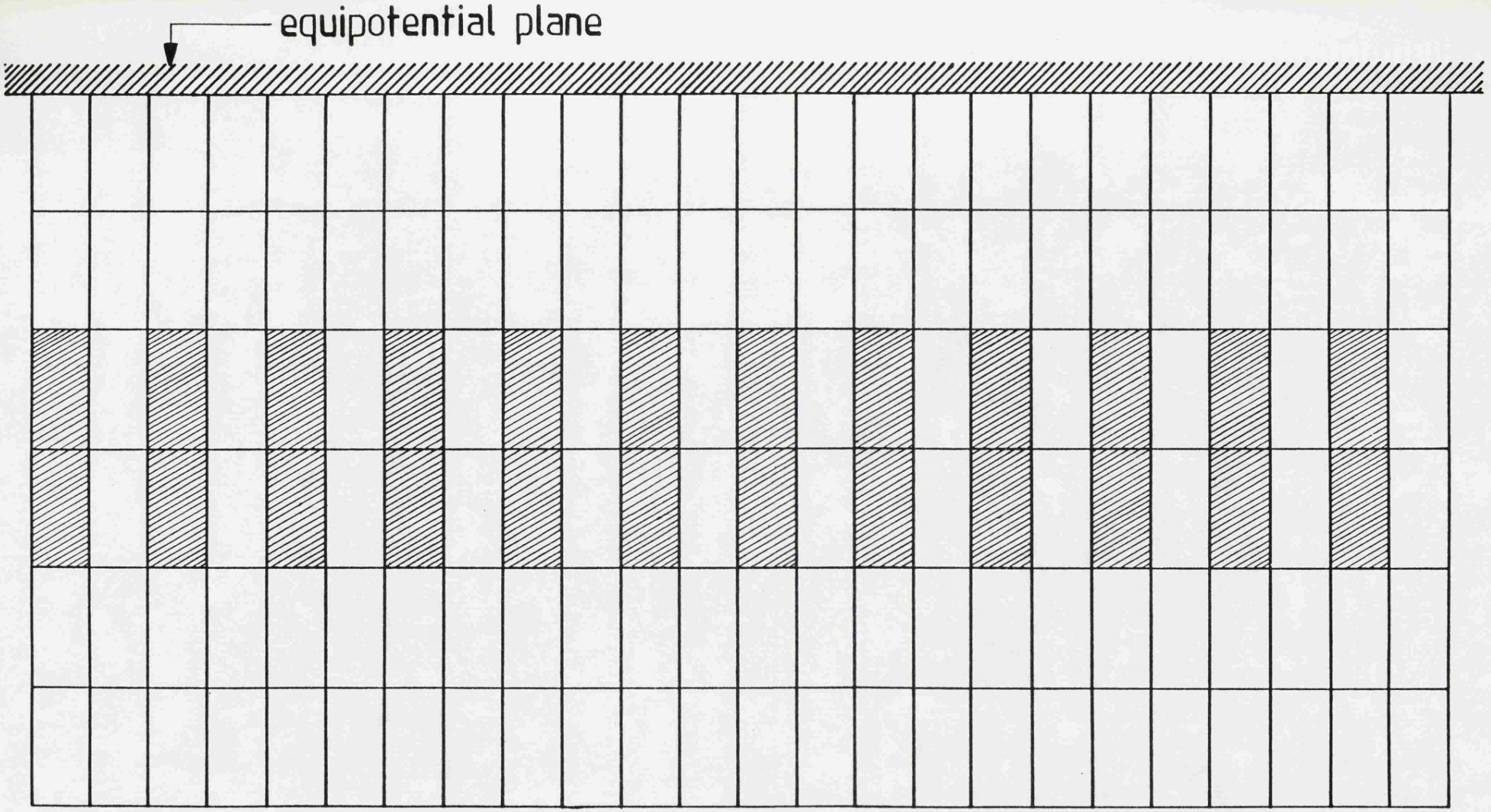

Fig 2·7·6: Y_cross section of LSM
(38th plane)

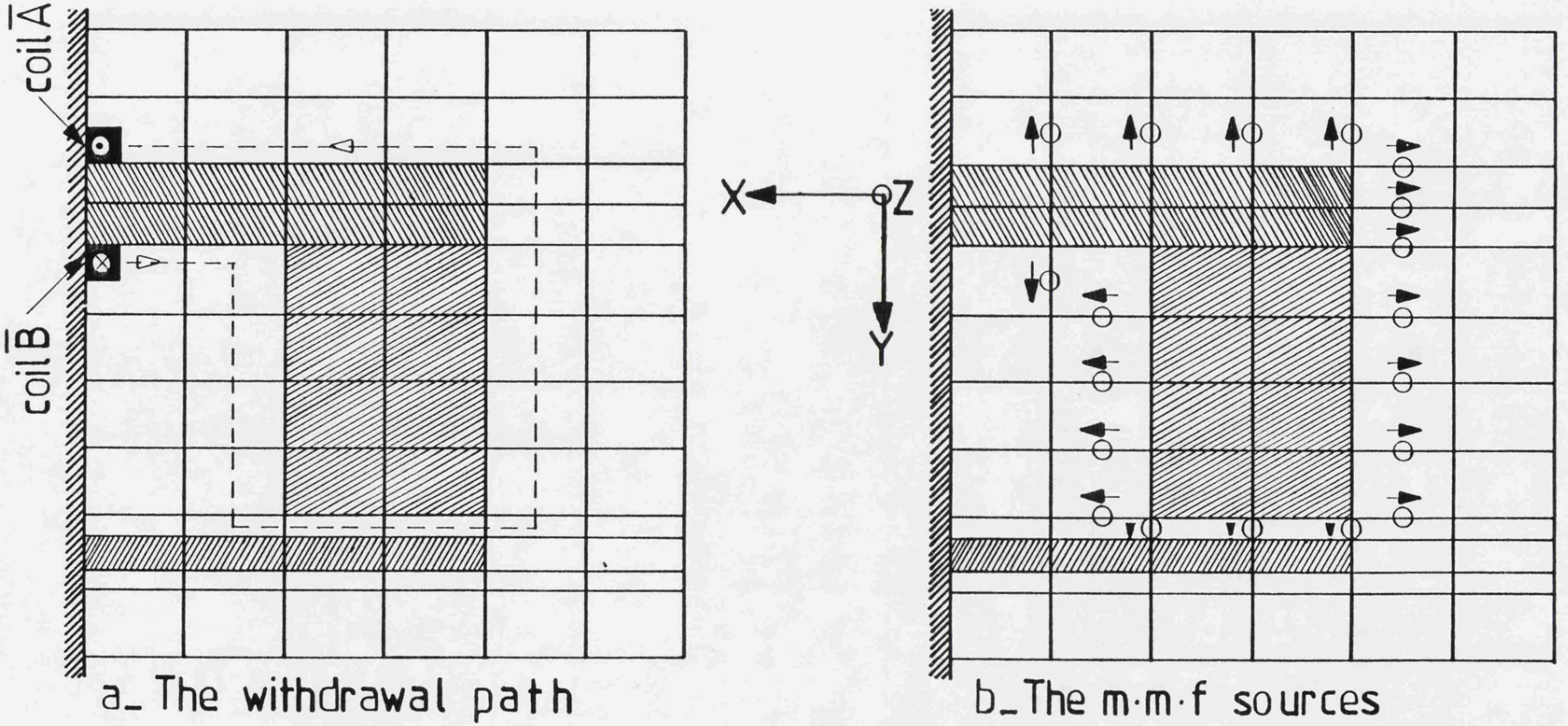

Fig 2·7·7 : Transformation of LSM field winding

turns of field winding, and I_f is a field current. The parameter 1/2 appears because of symmetry, i.e. half of the field winding exists. In a coil side B the current is assumed to enter the plane of the diagram. The current in coil side A flows out from the diagram. The method of making the transformation is to withdraw coil side B along the path shown by the dotted line until it coincides with coil side A (Fig. 2.7.7.a). The direction of withdrawal is everywhere perpendicular to the current flow paths. The equivalent mmf source appears in each of the magnetic branches which is cut by the dotted line. Each mmf source is equal in magnitude to $Z_f I_f/2$ and its direction is shown on the diagram. This transformation can also be performed by withdrawal of coil side A along the dotted line until it coincides with coil side B. Fig. 2.7.7(b) shows a view, in 2-dimensions, of the equivalent mmf sources due to the transformation of the field winding current. To obtain the equivalent mmf sources in the three dimensional network the same procedure must be followed for all cross sections looking in the z direction. Fig. 2.7.8 shows a comparison between measured flux density and that calculated using program TESTF. The point of comparison is at the coincidence of the pole centre-line and the centre-line of the side limb.

Figs. 2.7.9 (a) and (b) show the spatial distribution of air-gap flux for two different field currents.

2.7.4.2 Transformation of armature winding current

The armature winding of the homopolar linear synchronous machine is a distributed three phase winding in two layers with each coil side having N_c turns. The winding has 2 slots per pole and phase and each coil has a pitch of 4 slots. Two poles of the winding is shown in Fig. 2.7.10.

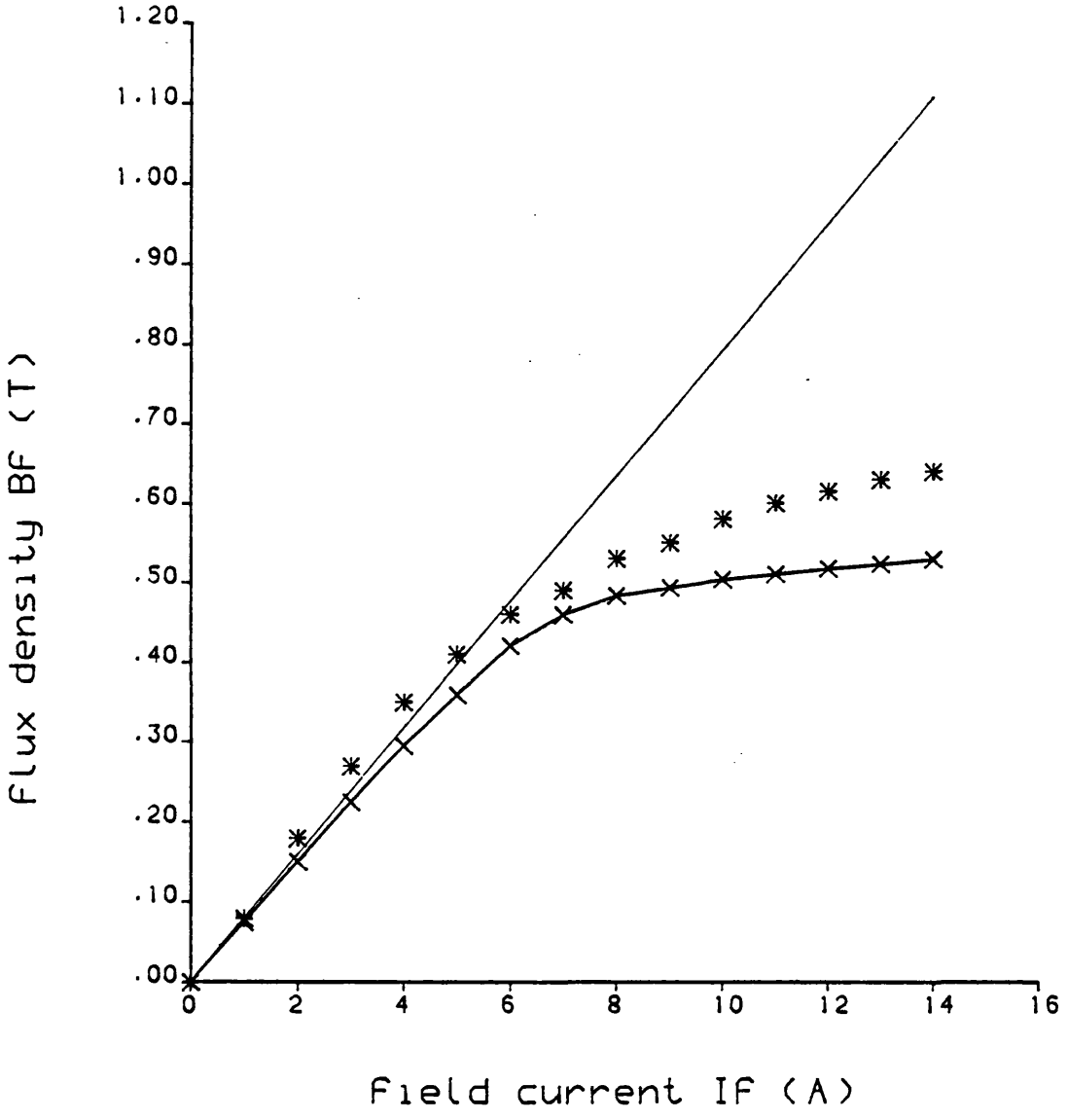

Fig.2.7.8 Magnetization curve and air gap line

* * * * * measurement

———— air gap line

x—x—x—x—x computing

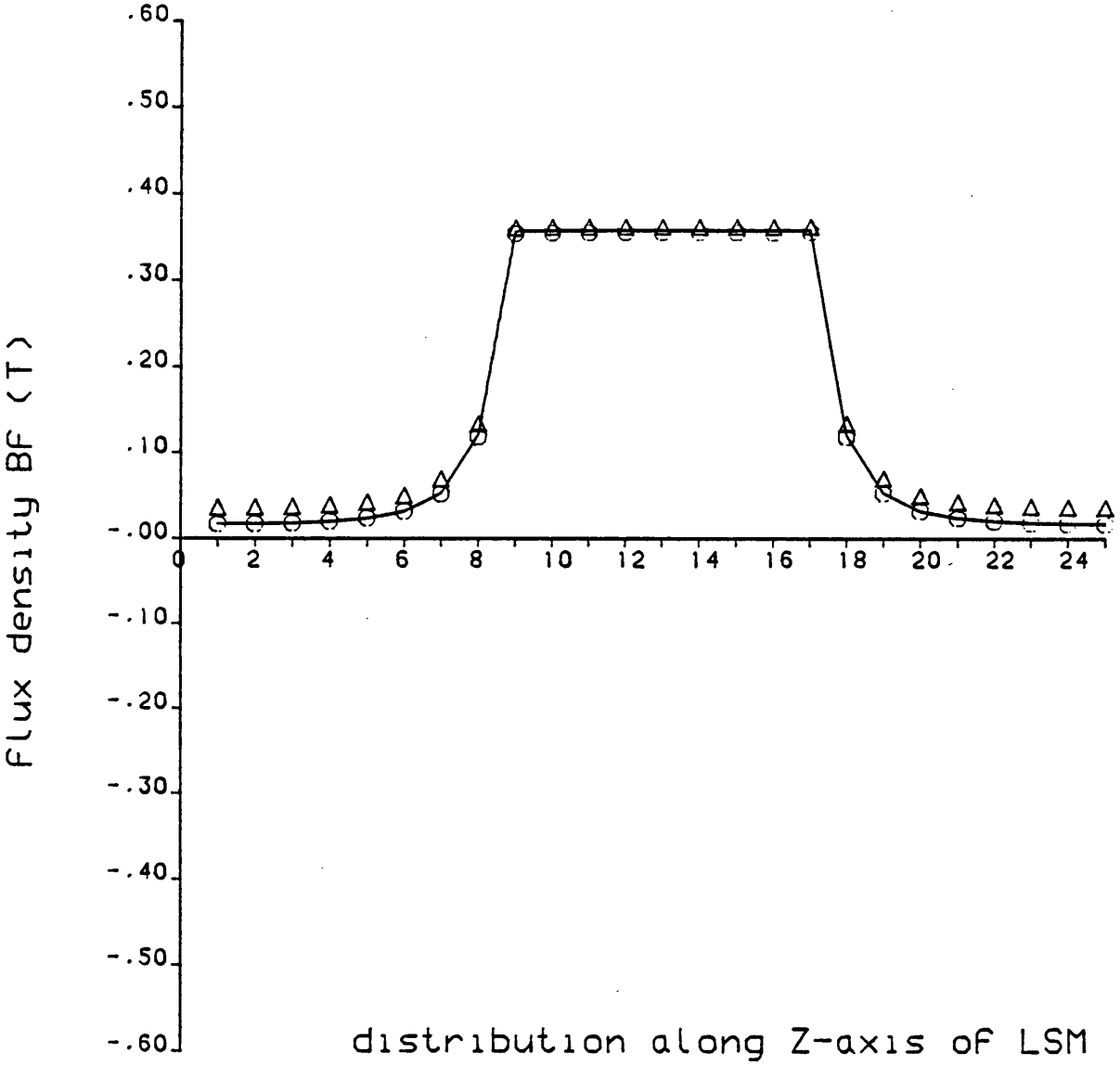

Fig. 2.7.9 (a) Space distribution of air gap flux density due to a field current of (5A)

Δ Δ Δ Δ Δ represents the flux density at D_2D_1 of Fig.2.7.2

——— " " " " " C_2C_1 " " "

o o o o o " " " " " B_2B_1 " " "

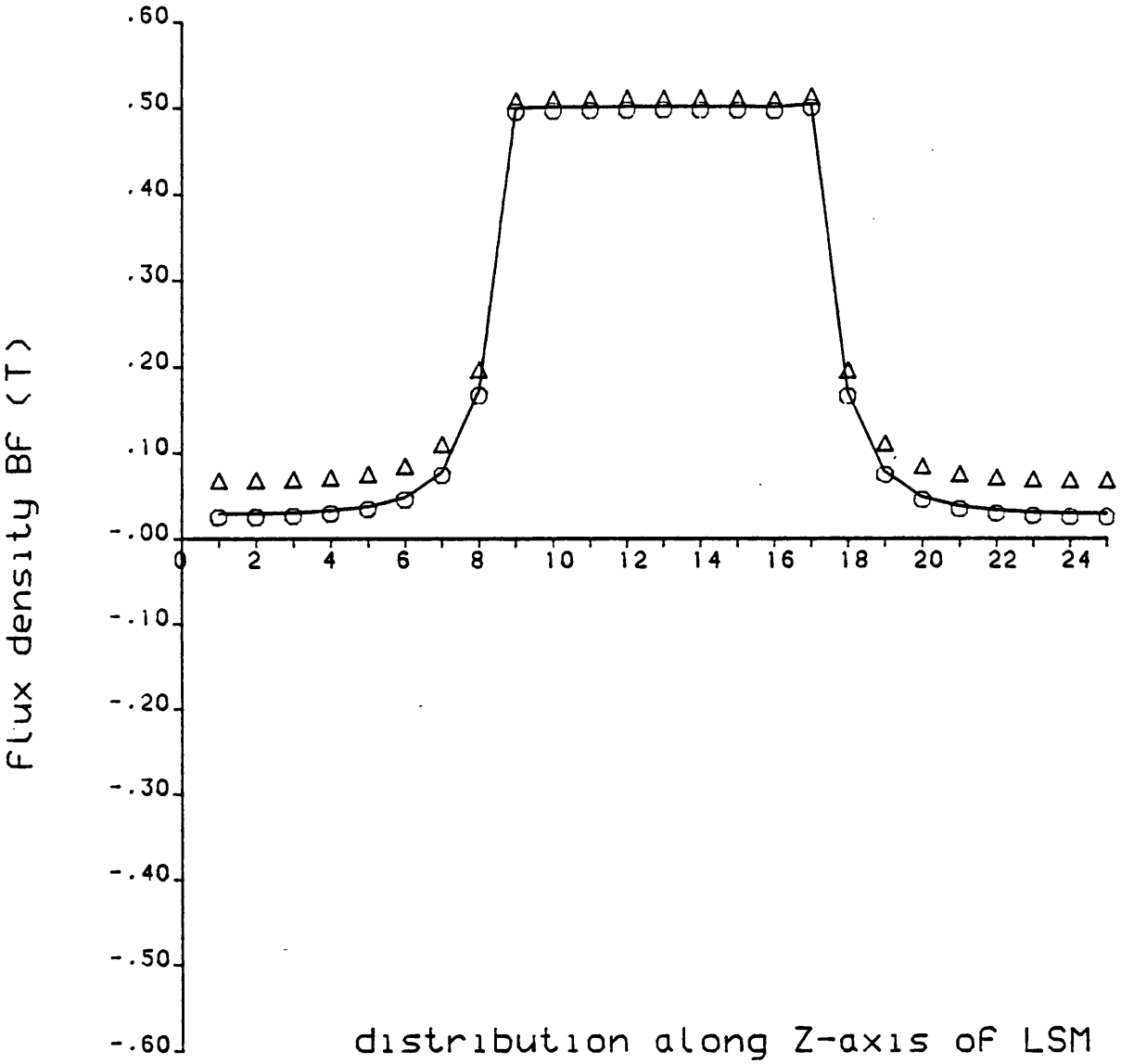

Fig. 2.7.9 (b) Space distribution of air gap flux density due to a field current of (10A)

Δ Δ Δ Δ Δ represents the flux density at D_2D_1 of Fig.2.7.2

——— " " " " " C_2C_1 " " "

o o o o o " " " " " B_2B_1 " " "

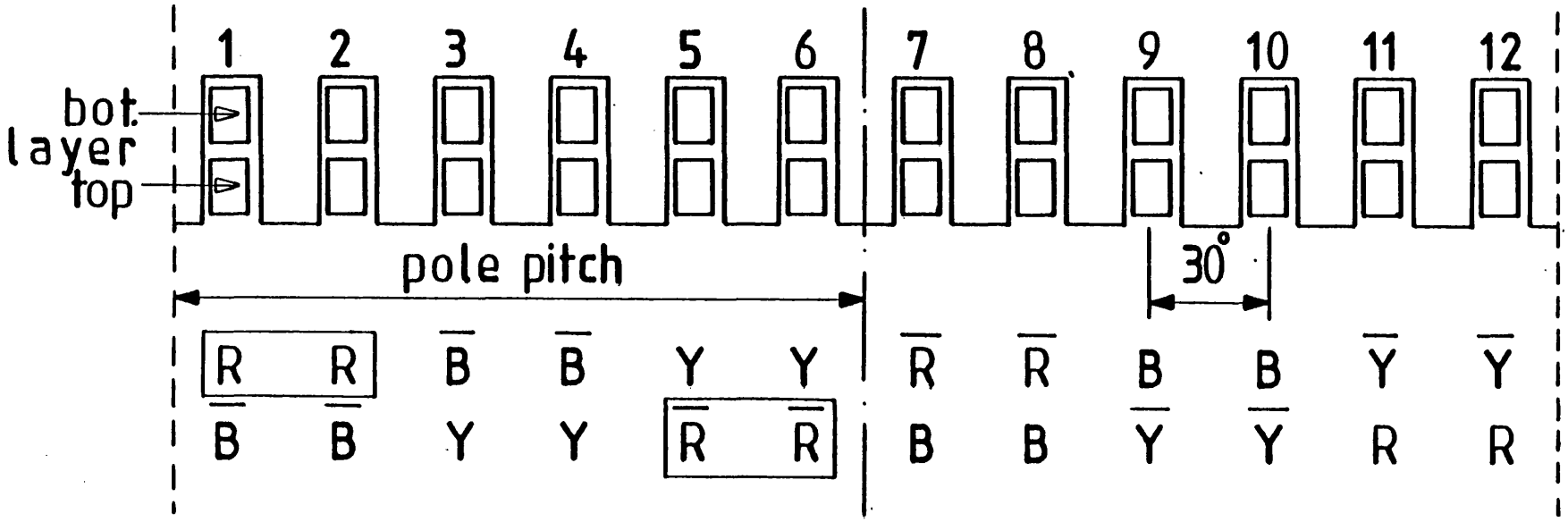

Fig 2·7·10: Integral slot chorded arrangement for 3_phase winding of LSM

The windings on each limb of the homopolar LSM were connected in series-star and connected together in series.

The analysis is carried out for the instant at which the red-phase is carrying the zero current. At this instant the yellow and blue phases carry a current equal to ($\sqrt{2}\ N_c I_a \cos 30$), where I_a is the rms value of armature current, as shown in Fig. 2.7.11.

A similar procedure to that used for the transformation of field current is used to transform the armature currents into equivalent mmf sources. In order to illustrate the process a single cross section will be considered.

The first step of transformation is to define the path which will be followed by withdrawal of a coil side. These paths for all the coil sides are illustrated by the dotted lines in Fig. 2.7.12. As a coil is withdrawn, it intersects a number of branches. Into each of these branches is placed an mmf source having the value of the coil current. The mmf sources in each branch are summed to give a set of single generators in each branch as shown in Fig. 2.7.13.

In the three dimensional network the procedure just described is used at each of the three cross sections seen in the x-direction. These are taken at BB_2, CC_2 and DD_2 as indicated in Fig. 2.7.2. In addition to these two further cross sections containing the end-turns (AA_1 and EE_1) are considered. For one of these cross sections, Fig. 2.7.14 shows the transformation of the end winding armature current into equivalent mmf sources. The withdrawal paths of the coil ends are

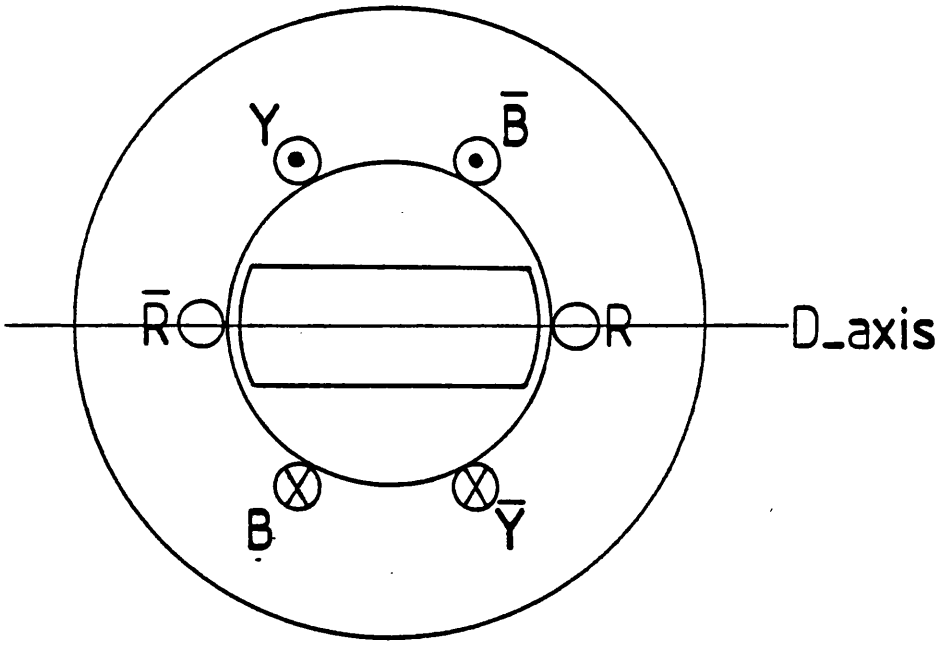

a:elementary representation of LSM

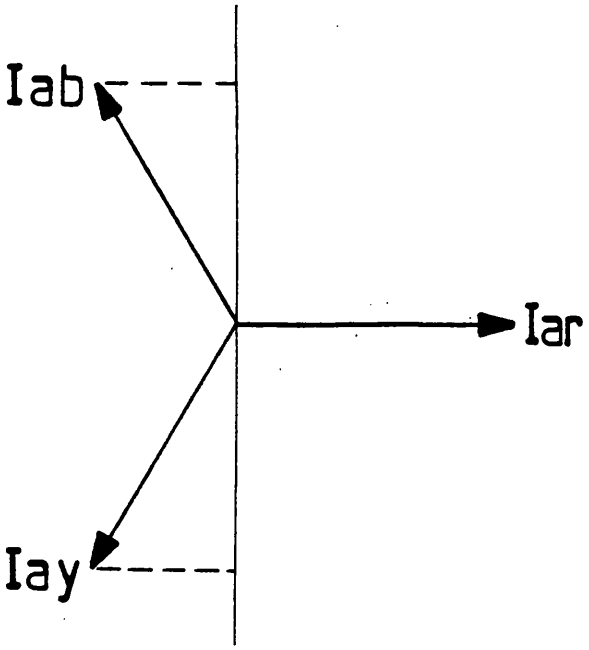

b:3_phase components of armature current

Fig 2·7·11

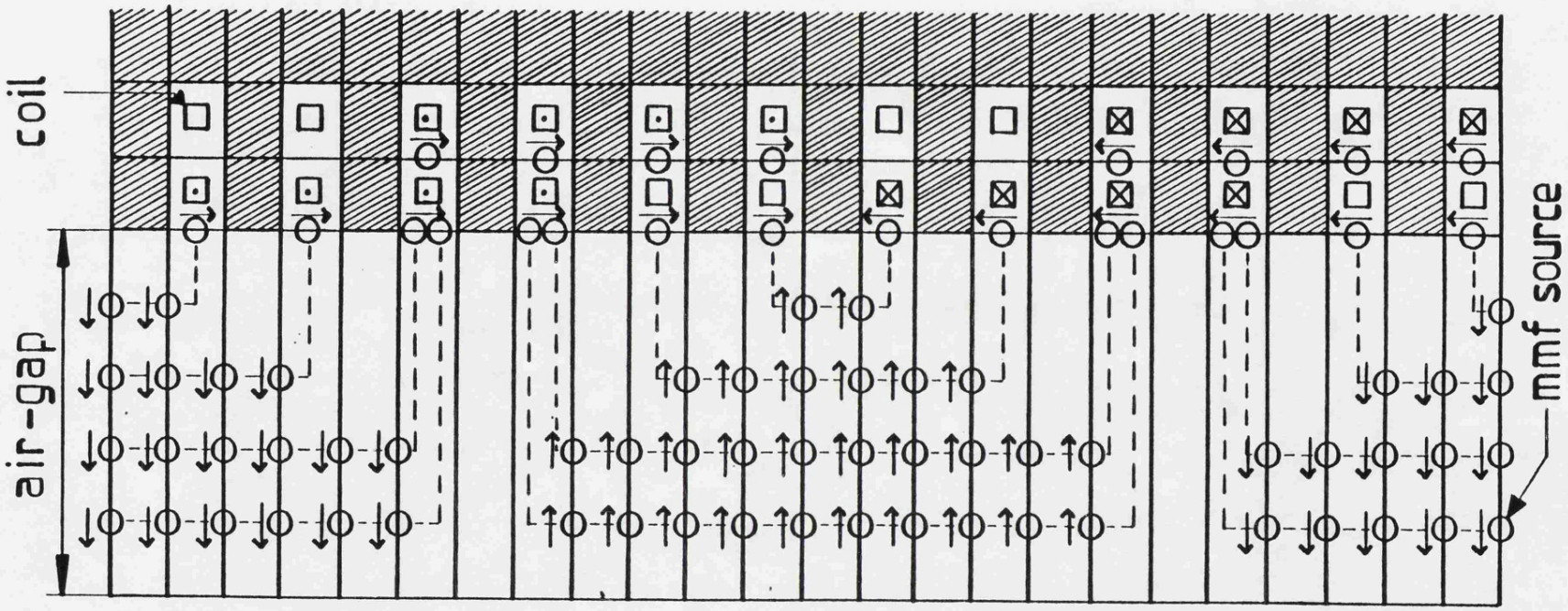

Fig 2·7·12 : Transformation of LSM armature winding

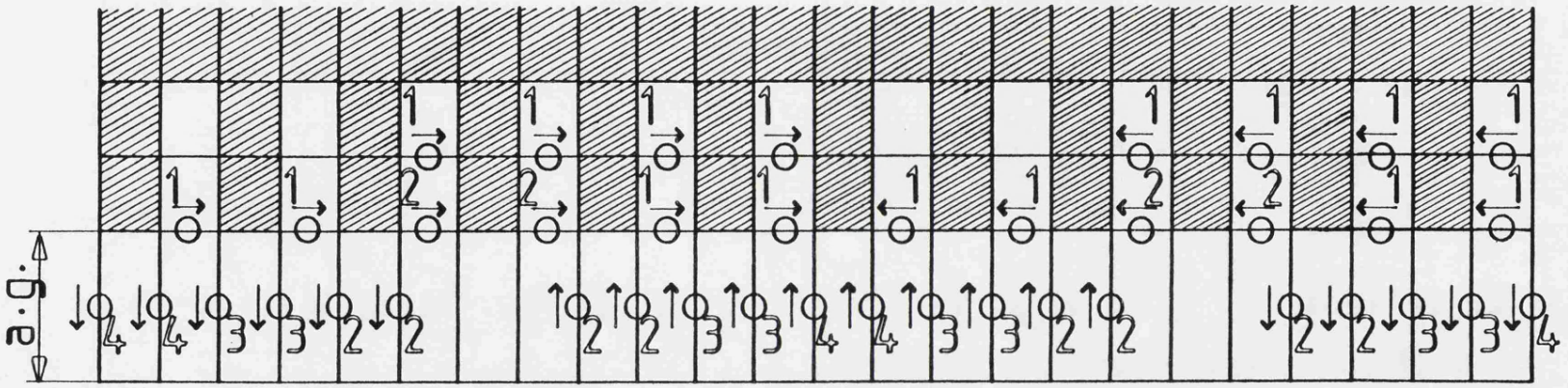

Fig 2·7·13 : The equivalent mmf sources duo to armature winding transformation

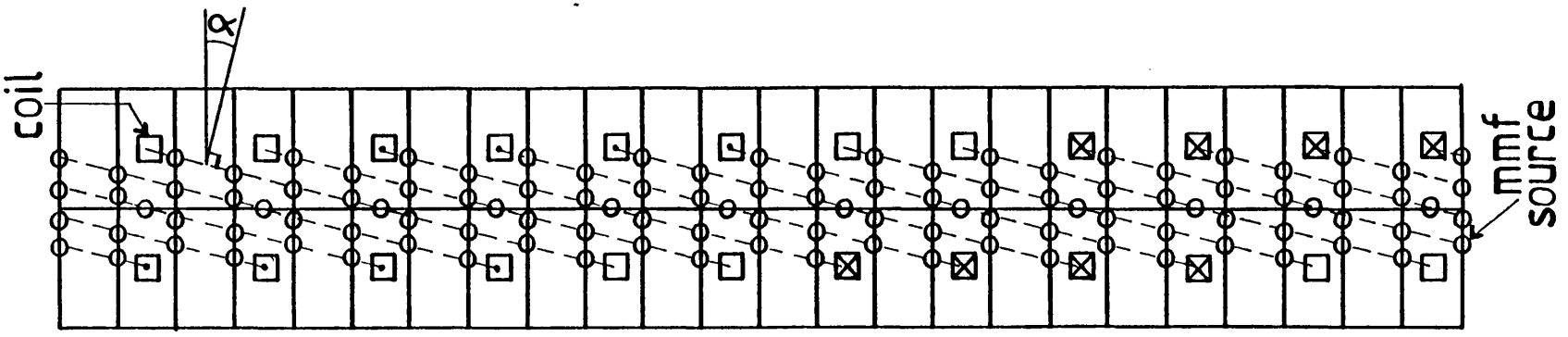

Fig 2·7·14 : Transformation of LSM armature end winding

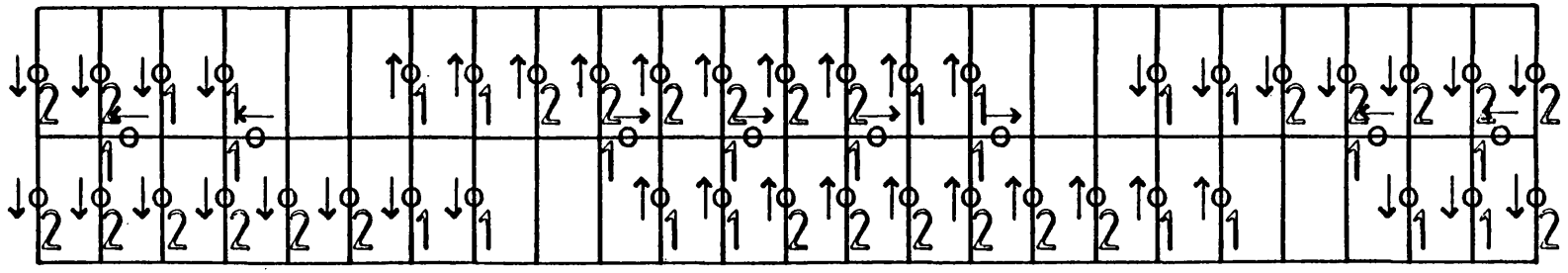

Fig 2·7·15 : The equivalent mmf sources duo to armature end winding transformation

indicated by dotted lines which are perpendicular to the current flow. The point to be noted in this case is that the withdrawal paths do not intersect the branches normally as in the previous cases when the field and armature, coil side currents were transformed. In this case, the normal direction (n) of each dotted line forms an angle "α", the vertical branches shown in Fig. 2.7.14. The value of the mmf source placed in a vertical branch is now equal to the coil current that intersects the branch multiplied by (cos α). The corresponding horizontal mmf source is multiplied by (sin α). The mmf sources are:

$$\text{mmf of vertical branch} = \sqrt{2}\, N_c I_a \cos 30 \cos \alpha$$

$$\text{mmf of horizontal branch} = \sqrt{2}\, N_c I_a \cos 30 \sin \alpha$$

The set of end-turn mmf sources are shown in Fig. 2.7.15.

Fig. 2.7.16 shows a comparison between measured flux density and that calculated using program TESTF. The armature winding is excited alone and the rotor pole is in the d-axis position. The point of comparison is at the peak of the waveform, in the centre-line of a side limb. Fig. 2.7.17 shows the spatial distribution of air gap flux density at an armature current of 9.7A.

Figs. 2.7.18 and 2.7.19 show corresponding results for the q-axis position.

2.7.4.3 Transformation for both field and armature windings

The procedure which has been performed in the previous two sections for the separate transformation of field and armature currents can also be used when both windings are excited together. The same sources of mmf as those that have been found in sections 2.7.4.1 and 2.7.4.2 are used with the equivalent branch mmf being found by algebraic summation

of the mmf sources in each branch. The flux and flux density in each branch of the three dimensional network can be obtained by using the computer program TESTF for torque angles of 0^{o}, 90^{o} and 180^{o} when both the field and armature currents of the LSM are energised. The air gap flux density distributions for the three torque angles are shown in Fig. 2.7.20 to 2.7.22.

2.8 Discussion and Conclusion

A non linear three dimensional solution has been developed to obtain the flux density in different parts of a homopolar linear synchronous machine at torque angles of 0^{o}, 90^{o} and 180^{o} taking saturation effects into account. Other torque angles can be easily obtained by suitable re-labelling of rotor elements.

The flux densities obtained from the field calculations can be used to predict the characteristics of the LSM. This will be done and a comparison made with experimental results in the next two chapters.

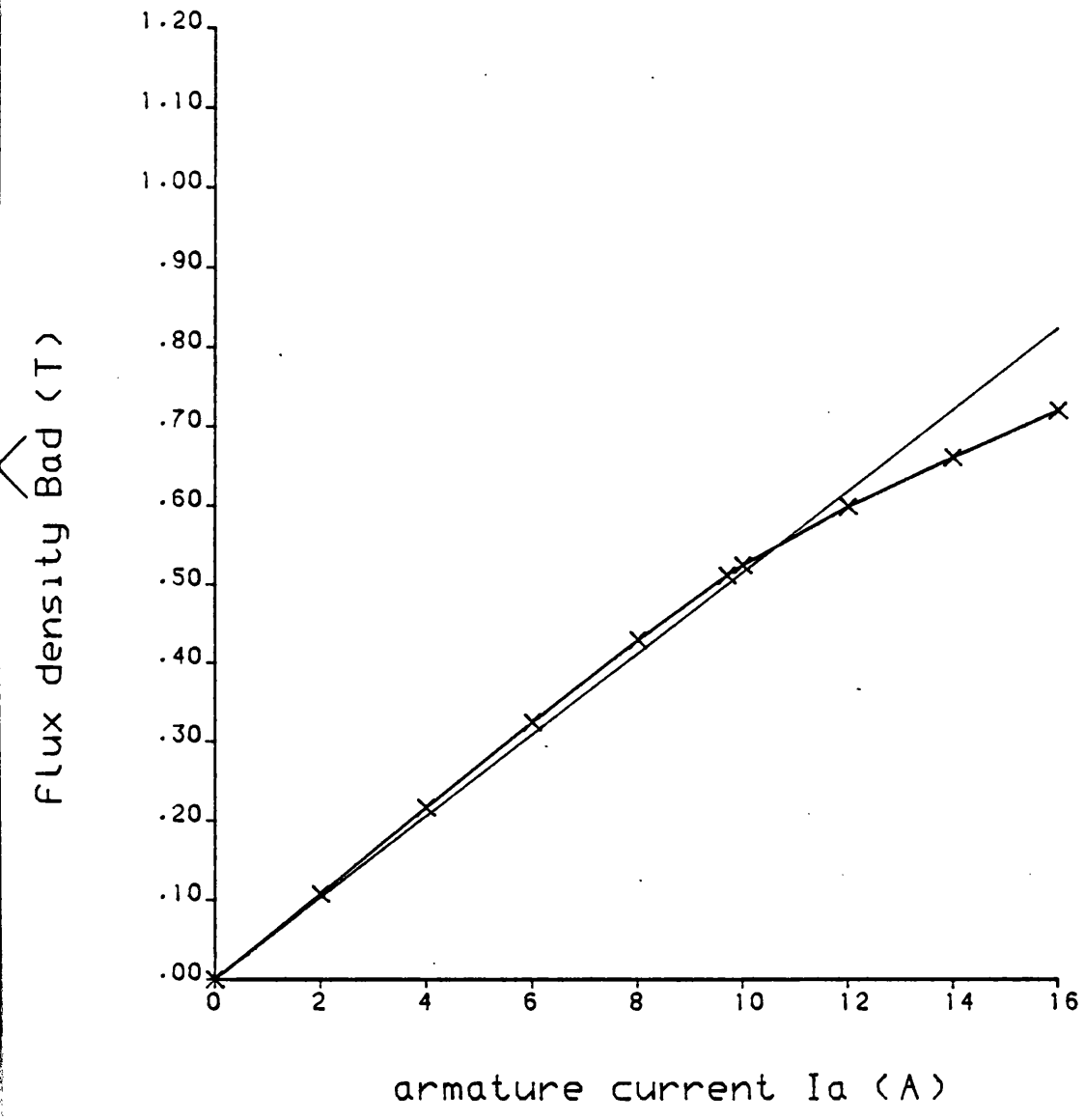

Fig. 2.7.16 D-axis air gap flux density due to an armature current, and air-gap line

———— air gap line

x—x—x—x—x— computing

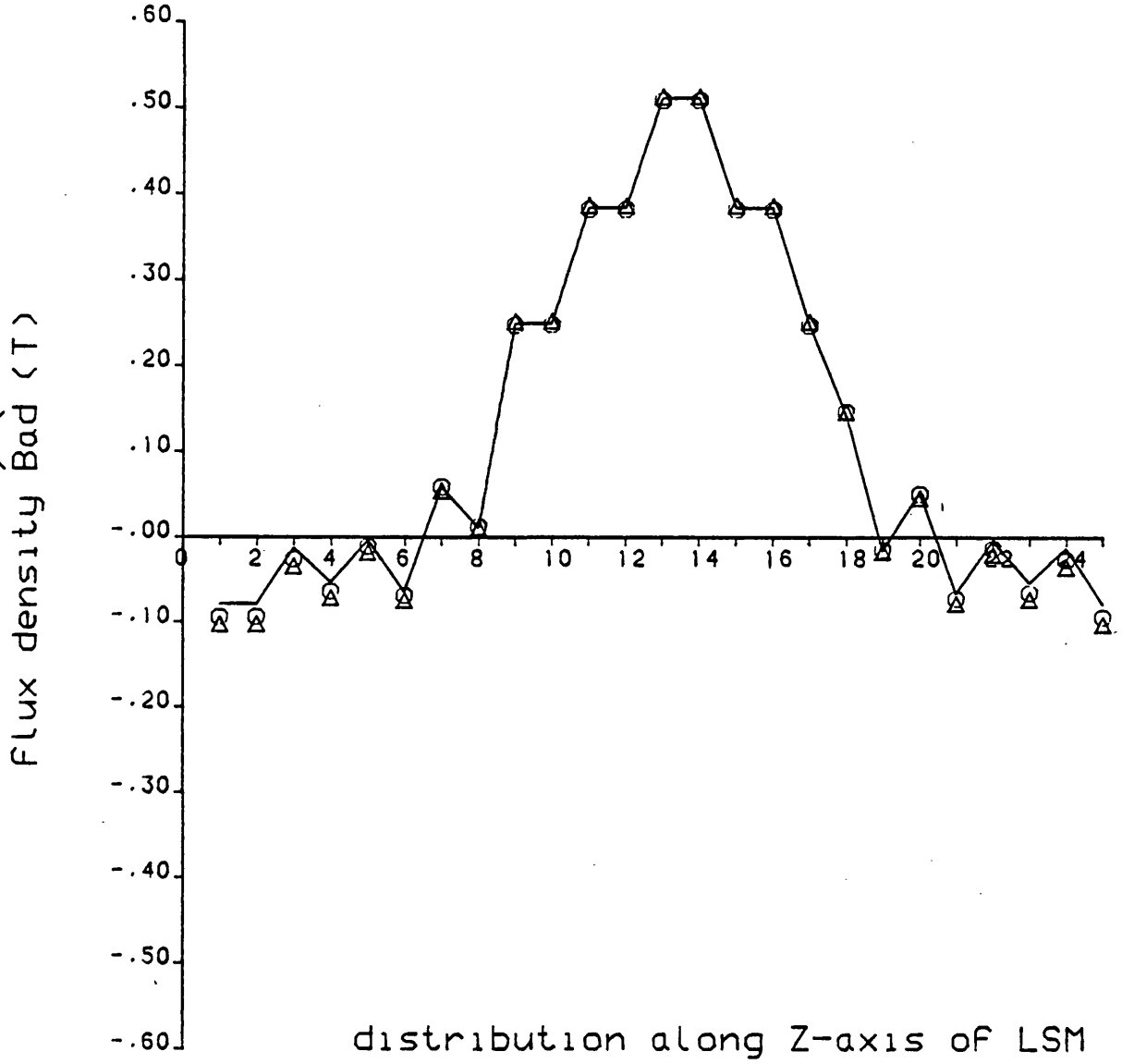

Fig. 2.7.17 D-axis space distribution of air gap flux density due to an armature current of (9.7A) rms

Δ Δ Δ Δ Δ represents flux density at D_2D_1 of Fig. 2.7.2

——— " " " " C_2C_1 " " "

o o o o o " " " " B_2B_1 " " "

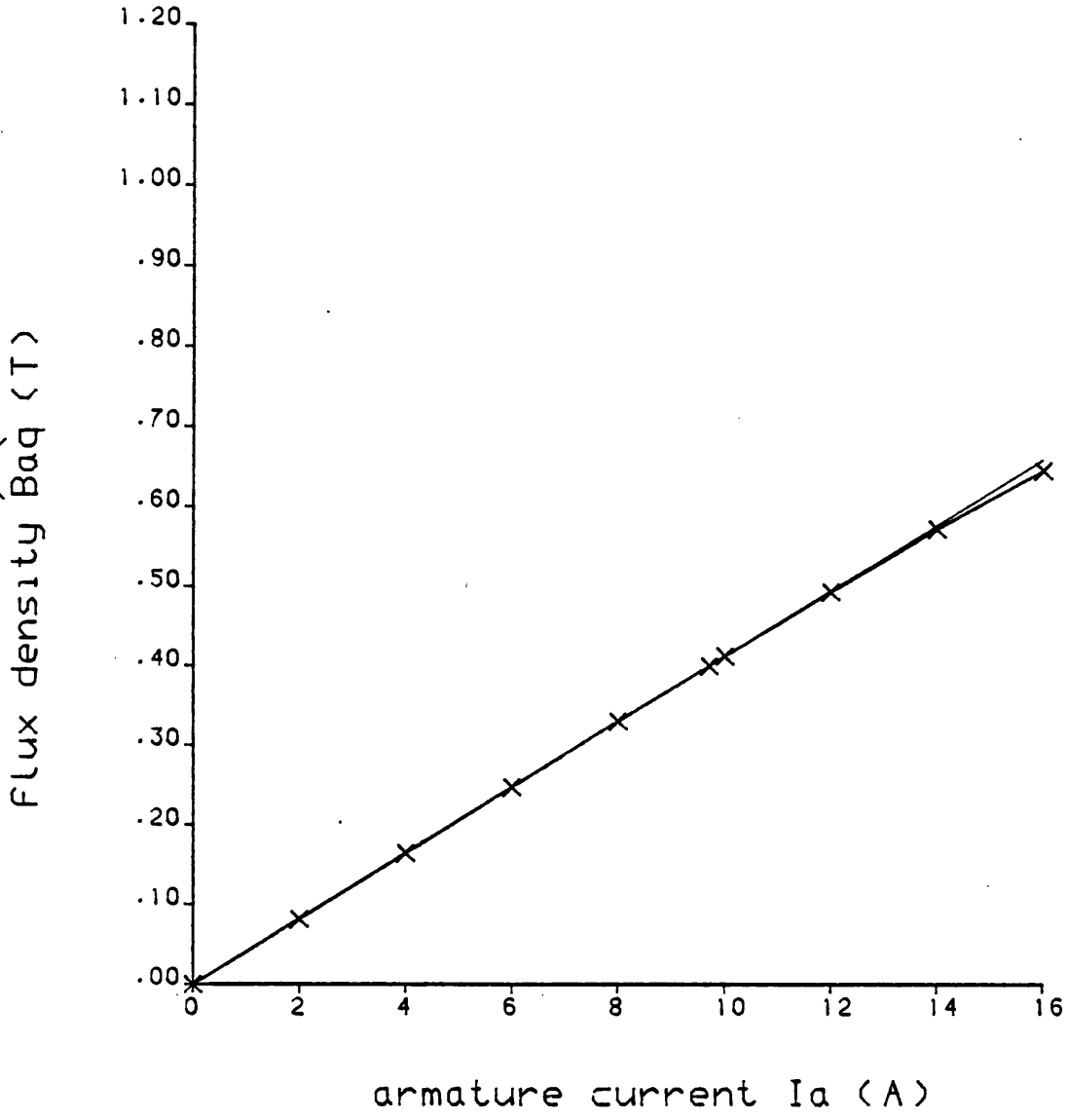

Fig. 2.7.18 Q-axis air gap flux density due to an armature current, and air gap line

———— air gap line

x–x–x–x–x computing

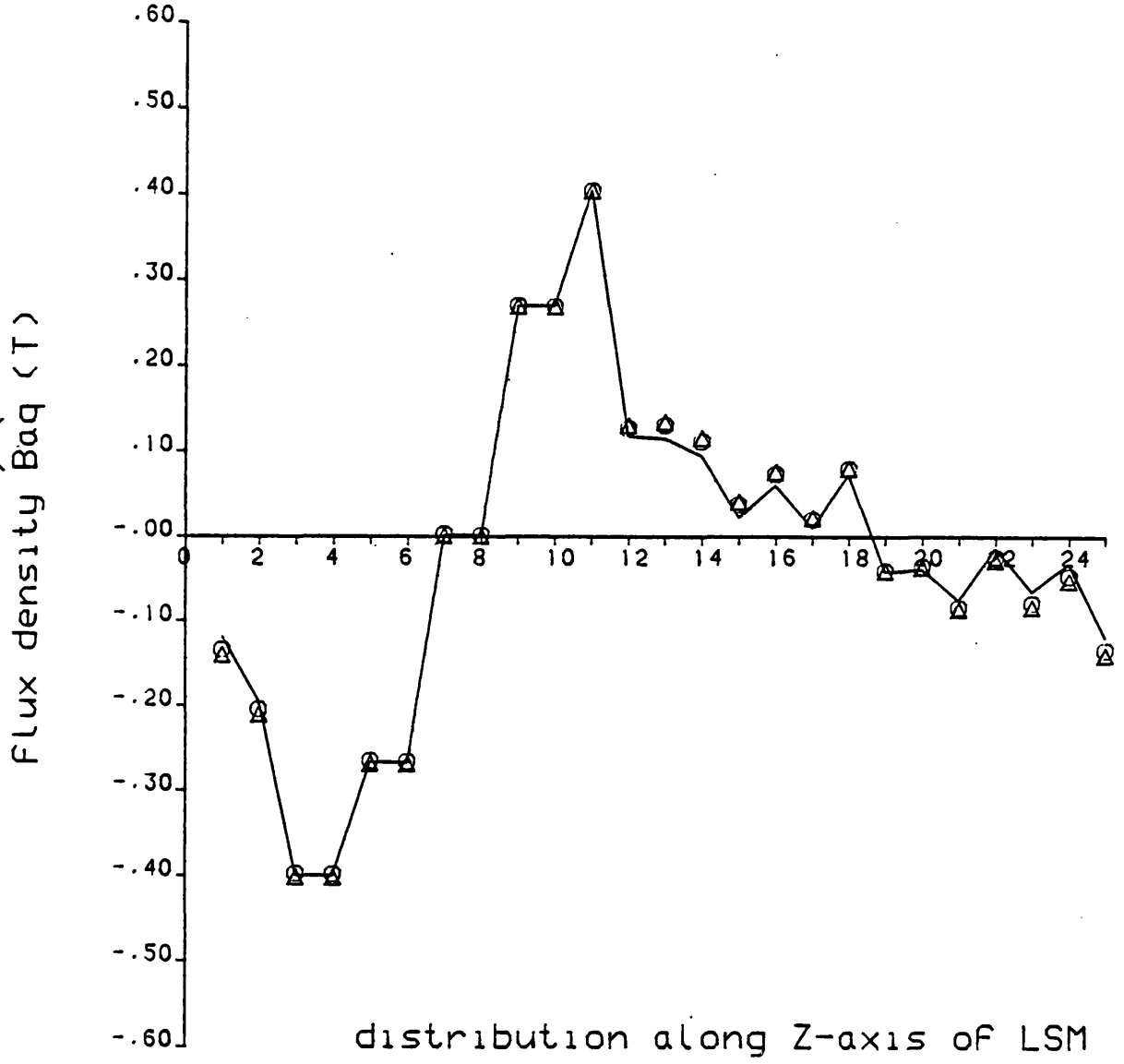

Fig. 2.7.19 Q-axis space distribution of air gap flux density due to an armature current of (9.7A) rms

Δ Δ Δ Δ Δ represents the flux density at D_2D_1 of Fig. 2.7.2

——— " " " " " C_2C_1 " " "

o o o o o " " " " " B_2B_1 " " "

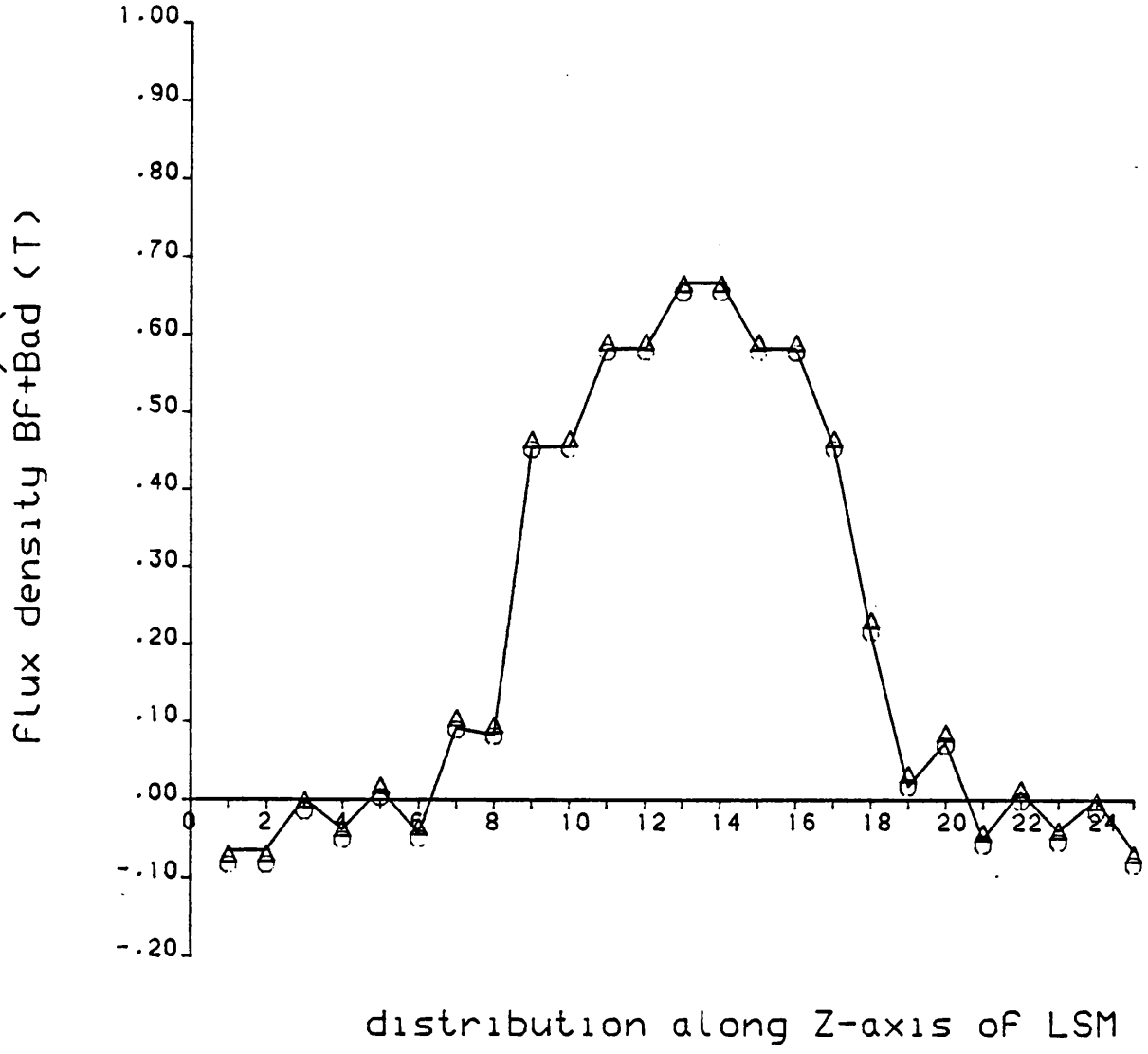

Fig. 2.7.20 Space distribution air gap flux density resulting from the field current of (5A) and armature current of (9.7A) rms at the torque angle of (0^{o})

Δ Δ Δ Δ Δ represents the flux density at D_2D_1 of Fig. 2.7.2

——— " " " " " C_2C_1 " " "

o o o o o " " " " " B_2B_1 " " "

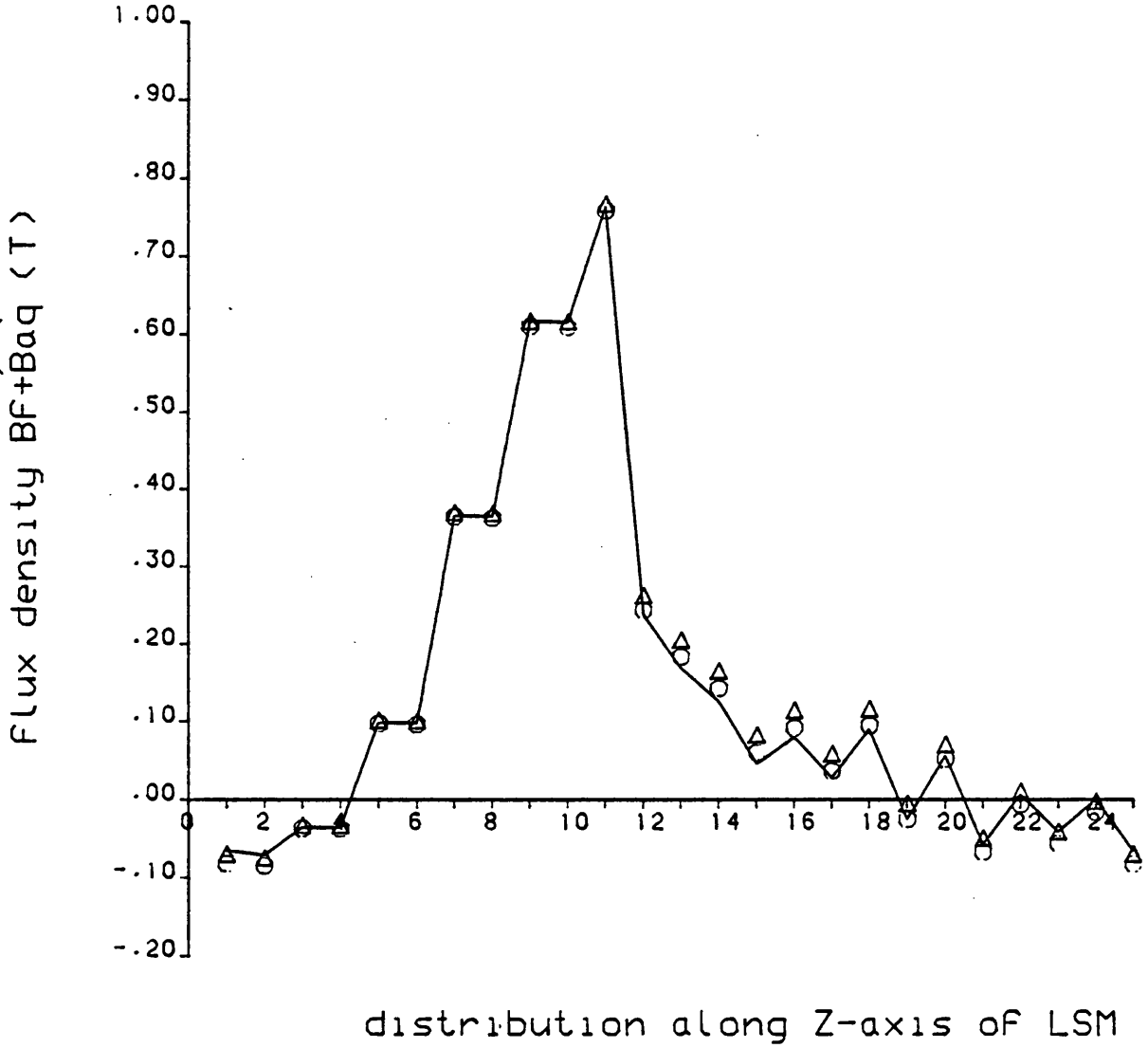

Fig. 2.7.21 Space distribution air gap flux density resulting from the field current of (5A) and armature current of (9.7A) rms at the torque angle of 90^{o}

Δ Δ Δ Δ Δ represents the flux density at D_2D_1 of Fig. 2.7.2

——— " " " " " C_2C_1 " " "

o o o o o " " " " " B_2B_1 " " "

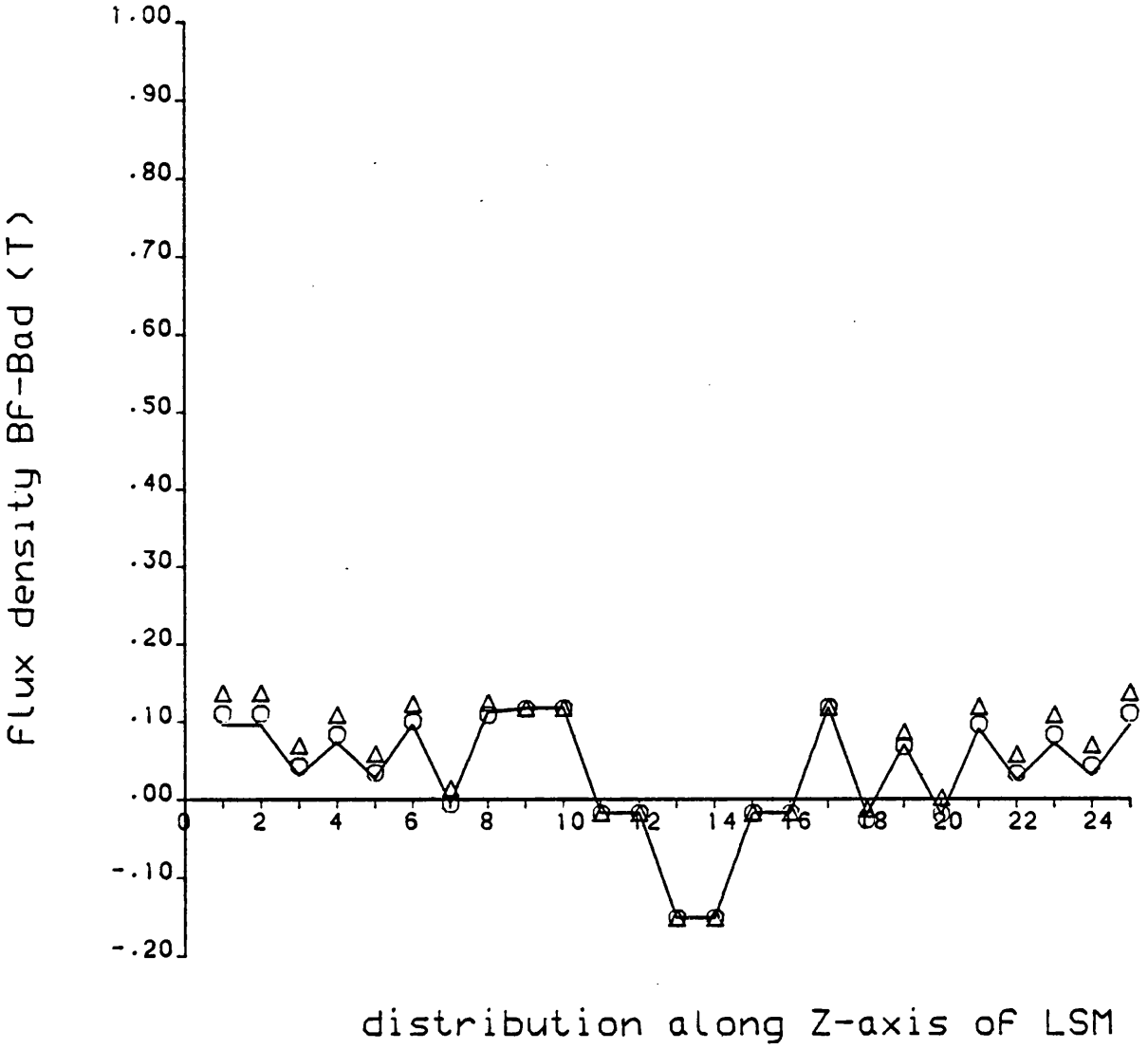

Fig. 2.7.22 Space distribution air gap flux density resulting from the field current of (5A) and armature current of (9.7A) rms at the torque angle of (180^{o})

Δ Δ Δ Δ Δ represents the flux density at D_2D_1 of Fig. 2.7.2

——— " " " " " C_2C_1 " " "

o o o o o " " " " " B_2B_1 " " "

2.9 Appendices

2.9.1 Simple air gap calculation

2.9.1.1 Introduction

The straight line tangent to the lower portion of the mangetizing curve is known as the air gap line. This indicates the mmf required to overcome the reluctance of the air gap. If there were no effects of saturation, the air gap line and magnetizing curve would coincide. The departure of the curve from the airgap line is therefore an indication of the degree of saturation present. In the absence of saturation the flux density in the air gap is directly proportional to the mmf and is inversely proportional to the length of the path in the air gap, i.e.

$$B = \frac{\mu_o}{g} \times \text{mmf} \qquad 2.9.1.1$$

where mmf = magnetomotive force

B = flux density

g = air gap length

μ_o = permeability of free space

2.9.1.2 Air gap flux density due to field current (B_f)

Referring to Fig. 2.7.2, the mmf of field winding drives the flux across two air gaps, each of which has a length of g. The mmf required to overcome the reluctance of each air gap is

$$\text{mmf (for field winding)} = \frac{Z_f I_f}{2}$$

where

Z_f = number of turns of field winding

I_f = field current

Substituting this mmf in equation 2.9.1.1 gives the flux density B_f due to the field current as

$$B_f = \frac{\mu_o}{g} \frac{Z_f I_f}{2} \qquad 2.9.1.2$$

2.9.1.3 Air gap flux density due to armature current (B_a)

The mmf of the three phase armature winding is based on the fundamental term alone. Its magnitude can be expressed as[2.8]

$$\hat{\text{mmf}} \text{ (for armature winding)} = \frac{3(Z_a q K_w)}{\pi} \hat{I}_a \cos\theta$$

where

Z_a the number of turns per slot

q the number of slots per pole per phase

K_w the winding factor

$\hat{I}_a$ the peak value of armature current

This mmf is a sinusoidal function of the space angle θ, and its substitution in equation 2.9.1.1 gives

$$\hat{B}_a = \frac{\mu_o}{g} \cdot \frac{3(Z_a q K_w)}{\pi} I_a \sqrt{2} \cos\theta \qquad 2.9.1.3$$

where $\hat{B}_a$ is the peak value of the flux density due to the rms armature current I_a.

2.9.2 Dimensions of test machine

Fig. 2.9.2.1 shows the main dimensions of the test machine. Details of the windings and slotting are given below:

series conductors per armature winding slot (Z_a)	= 58
series conductors of field winding (Z_f)	= 400
slot per pole per phase (q)	= 2
coil pitch (slots)	= 4
slot-width/slot-pitch ratio	= 0.5
phase spread (σ)	= 60^o
chording angle (ε)	= 60^o
winding factor (K_w)	= 0.8366
slot type	= semiclosed

The calculation of winding factor is based on the following equations[2.8]

$$K_w = K_d.K_e \qquad 2.9.2.1$$

where K_d is the distribution factor. Its magnitude for the fundamental of the air-gap flux is

$$K_d = \frac{\sin \frac{1}{2} \sigma}{q \sin \frac{1}{2} (\sigma/q)} = \frac{\sin \frac{1}{2} (60)}{2 \sin \frac{1}{2} (60/2)} = 0.966$$

and K_e is the chording factor. Its magnitude for the fundamental air-gap flux is

$$K_e = \cos \frac{1}{2} (\varepsilon) = \cos \frac{1}{2} (60) = 0.866$$

Substituting the values of K_d and K_e in the equation 2.9.2.1 gives

$$K_w = 0.966 \times 0.866 = 0.8366$$

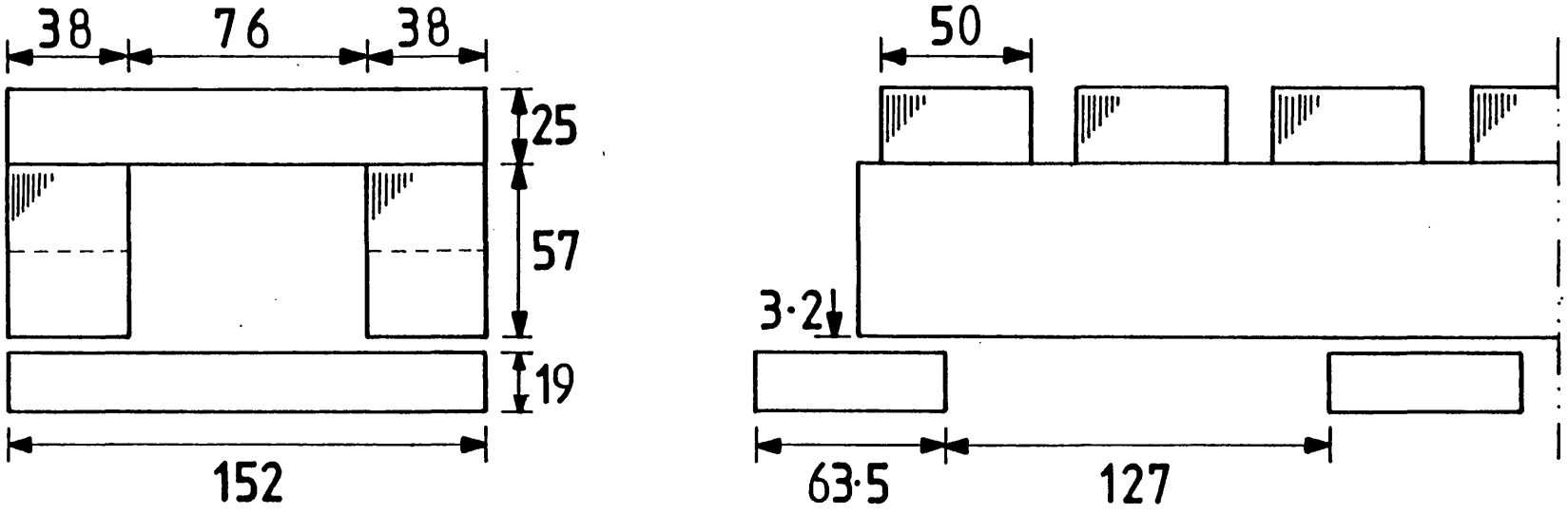

Fig 2·9·2·1 : Principal dimensions of test machine
(Dimensions in mm)

References

2.1 Silvester, P.:
"Modern Electromagnetic Fields", (Prenctice, Inc, Englewood Cliffs, N.J., 1968).

2.2 Zienkiewicz, O.C., Lyness, J. and Owen, D.J.R.:
"Three dimensional magnetic field determination using a scalar potential - a finite element solution", IEEE Trans. Magnetics, Mag 13, 1977, pp.1649-1656.

2.3 Mamak, R.S. and Laithwaite, E.R.:
"Numerical evaluation of inductance and ac resistance with particular reference to electrical machines", Proc.IEE, vol.108C, pp.252-258, Nov. 1960.

2.4 Trutt, F.C., Erderyi, E.A. and Hopkins, R.E.:
"Representation of the magnetization characteristic of dc machines for computer use", IEEE Trans., March 1968, pp.665-669.

2.5 Carpenter, C.J. and Djurovic, M.:
"Three dimensional numerical solution of eddy currents in thin plates", Proc.IEE, June 1975, vol.122, No.6, pp.681-688.

2.6 Eastham, J.F.:
"Iron-cored linear synchronous machines", Electronics and Power, 1977, 23, pp.239-242.

2.7 Simkin, J. and Trowbridge, C.W.:
"On the use of the total scalar potential in the numerical solution of field problems in electromagnetics", International Journal for Numerical Methods in Engineering, vol.14, pp.423-440.

2.8 Say, M.G.:

"Alternating Current Machines", (Fourth Edition, Pitman Publishing, 1977).

CHAPTER THREE

CALCULATION OF INDUCTANCE COEFFICIENTS AND INDUCED EMF

3.1 Introduction

The coefficients of self and mutual inductance will vary with current over a wide range in machines where iron forms an essential part of the construction. It is therefore necessary to examine the effects of saturation on the performance of the homopolar linear synchronous machine.

The open circuit saturation, or magnetization, curve of a synchronous machine is the relation between the mmf of the field winding and the resultant flux per pole. The curve is usually drawn by using induced armature voltage as ordinate and field current as abscissa. These quantities are proportional to the flux per pole and to the mmf of the field winding per pole respectively when the machine is operated at constant speed. The magnetisation curve can be used to predict the curve of mutual inductance between field and armature windings[3.14].

There are two important coefficients of armature reaction which are due to the saliency of the rotor. These are: the direct axis reactance X_d, that occurs when the axis of the armature mmf coincides with the pole axis; and the quadrature axis reactance X_q, that occurs when the axis of the armature mmf is in the centre of the interpolar space. Wieseman[3.8] has derived accurate coefficients by flux plotting for the calculation of the fundamental sine wave of flux produced in a salient pole machine by the concentrated field turns, and by a sinusoidally distributed armature reaction. By taking the ratio of these two coefficients, the necessary factor to convert the armature reaction ampere-turns into equivalent field ampere-turns has been derived[3.8] and used by Alger[3.3] to calculate the armature reactance.

The armature leakage reactance is defined as the difference between the total, or synchronous, armature reactance and the reactance of armature reaction[3.2-3.3]. The leakage flux in the air-gap which fails to reach the rotor of the homopolar LSM will be considered to be a part of the magnetising inductance.

In this chapter, the basic machine parameters L_{mf}, M_{af}, L_{md} and L_{mq} for homopolar linear synchronous machines will be investigated. To take saturation effects into account, the inductances will be calculated using a flux linkage method. This in turn uses flux plots which were obtained from the three dimensional nonlinear program described in Chapter 2.

In addition to the numerically calculated inductances, algebraic equations are developed to give a simple estimate of the values. To take the fringing effects into account, Carter's coefficients are used to calculate the effective pole length. The coefficient for poles of equal polarity is used for calculation of the field and d-axis inductances, and that for poles of opposite polarity is used for q-axis inductance. All harmonics in the mmf distribution of the DC and three phase armature windings are ignored with the exception of the fundamental component. Also, all harmonics due to non-uniform air-gap geometry were ignored.

3.2 Inductance Calculation by the Flux Linkage Method

3.2.1 Introduction

In order to determine accurate values for the LSM inductances, detailed flux plots for the machine are considered. The inductance is obtained directly from the plots using the flux linkage per ampere of current in the coil. This is expressed in the following well known relationship:

$$L = \frac{\lambda}{i} = \frac{N\phi}{i} \qquad 3.2.1$$

where

L: inductance

λ: flux linkage

N: number of turns

ϕ: flux produced by the coil

i: current through the coil

3.2.2 Self magnetising inductance of the field winding (L_{mf})

Fig. 3.2.1 shows a plan view of the air-gap branches of the homopolar LSM. In the Figure the small circles indicate the mmf sources that are due to the field winding transformation. From Chapter 2, the number of turns for each of these sources is N_f = 200 turns. Temporary symbols such as ℓ, m, r, 1, 2,..., and 25 as shown in Fig. 3.2.1 are used to explain the procedure being followed for calculation of the flux linkage so that each branch is described by letter and number. Considering the flux in the air-gap only, the flux linkage due to the field current is

$$\lambda_f = \sum_{k=1}^{25} \frac{(N_f\phi_f)_{\ell k}}{2} + (N_f\phi_f)_{mk} + \frac{(N_f\phi_f)_{rk}}{2}$$

where ϕ_f is the flux produced by field current I_f obtained from the 3-D program in Chapter 2. Since the network model of the homopolar LSM represents 1 pole pair, the magnetising inductance for 2p poles is:

$$L_{mf} = \frac{2p \sum_{k=1}^{25} \frac{(N_f\phi_f)_{\ell k}}{2} + (N_f\phi_f)_{mk} + \frac{(N_f\phi_f)_{rk}}{2}}{I_f} \qquad 3.2.2$$

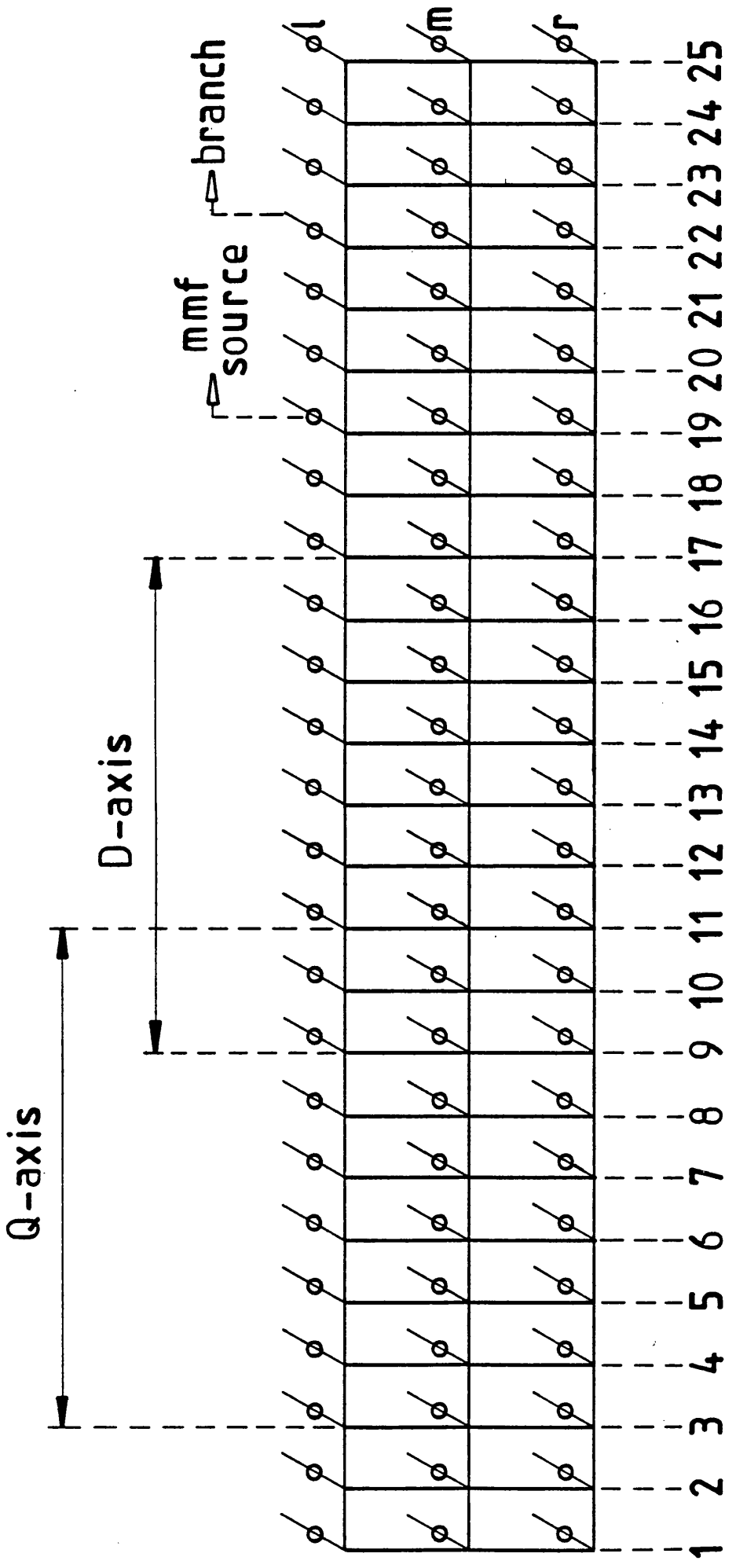

Fig 3·2·1 : Three dimensional air-gap branches of homopolar LSM

The self-inductance against field current curve obtained using this method is shown in Fig. 3.2.2. The same inductance calculated using the analytical methods of section 3.4.1 (equation 3.4.1.5) is also shown in this Figure.

3.2.3 Self magnetising inductances of the armature winding (L_{md} and L_{mq})

The elementary representation and the transformation of the three phase winding of the homopolar LSM is shown in Figures 2.7.11 and 2.7.13 in Chapter 2. Keeping the same connection to the armature winding, L_{md} and L_{mq} can be calculated when the rotor is set on either the d-axis or the q-axis as shown in Fig. 3.2.1. The connections to the armature winding are shown in Fig. 3.2.3. This circuit is similar to that used in reference 3.14 for measuring the q-axis inductance. Flux linkage was measured at terminals xx, and the reading value was multiplied by a convenient factor (1/2) to give the phase inductance.

A similar procedure to that described in section 3.2.2 for calculating L_{mf} is employed in this case. The flux linkage of the armature winding, whether the rotor is in the d-axis or q-axis position, can be written:

$$(\hat{\lambda})_{xx} = \sum_{k=1}^{25} \frac{(N_a \hat{\phi}_a)_{\ell k}}{2} + (N_a \hat{\phi}_a)_{mk} + \frac{(N_a \hat{\phi}_a)_{rk}}{2}$$

where N_a is the number of turns of the transformed armature winding and which can easily be obtained from Fig. 2.7.13, and $\hat{\phi}_a$ is the peak value of flux due to armature current $\hat{I}_a$. The values of $\hat{\phi}_a$ through the 3D network branches have been found in Chapter 2.

The corresponding magnetising inductance at terminals xx of Fig. 3.2.3 is expressed using equation 3.2.1 as:

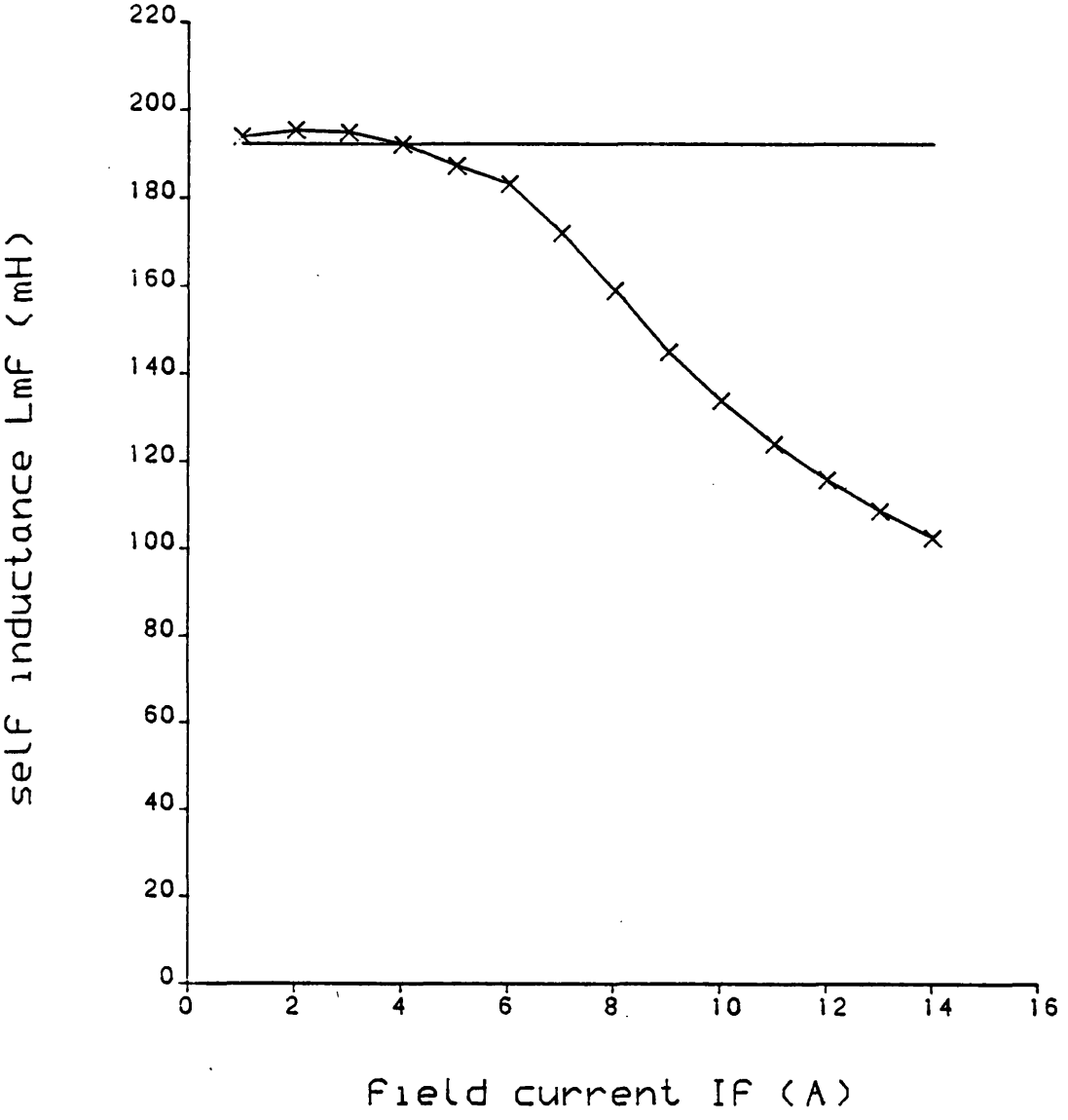

Fig. 3.2.2 Field winding self magnetising inductance for linear or cylindrical LSM

———— simple air gap calculation

x–x–x–x–x computing

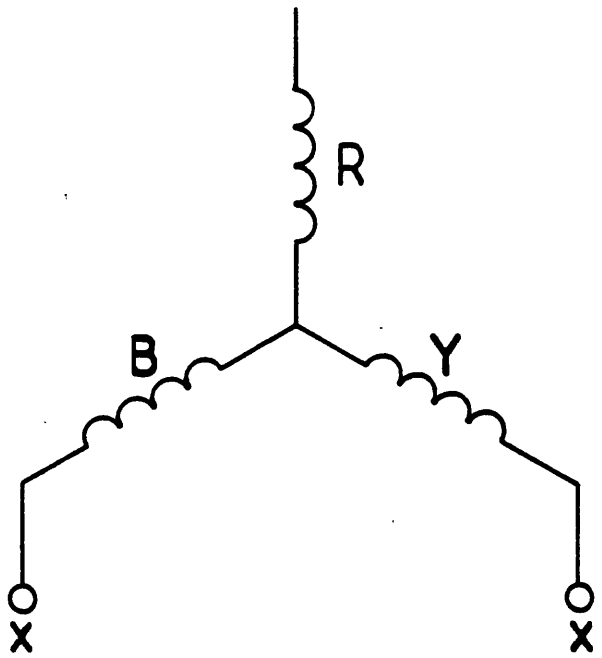

Fig 3·2·3 : The equivalent circuit of 3-phase armature connection for LSM

$$(L_{md,q})_{xx} = \frac{2p \sum_{k=1}^{25} \frac{(N_a \hat{\phi}_a)_{\ell k}}{2} + (N_a \hat{\phi}_a)_{mk} + \frac{(N_a \hat{\phi}_a)_{rk}}{2}}{\hat{I}_a}$$

By using a multiplication factor[3.14] which is equal to (1/2), the magnetising inductance per phase is written

$$L_{md,q} = \frac{p \sum_{k=1}^{25} \frac{(N_a \hat{\phi}_a)_{\ell k}}{2} + (N_a \hat{\phi}_a)_{mk} + \frac{(N_a \hat{\phi}_a)_{rk}}{2}}{\sqrt{2}\, I_a} \qquad 3.2.3$$

Complete sets of self magnetising inductances due to different armature currents, with the rotor positioned on the d-axis and q-axis are shown in Figures 3.2.4 and 3.2.5 respectively. In these figures the simply calculated air-gap inductances are also found using equations 3.4.2.2 and 3.4.3.1.

The induced rms voltage per phase per angular frequency ($E/\omega = L_{md,q} I_a$) for the d-axis and q-axis obtained using the inductances are compared with the measured voltages taken on the cylindrical version of the homopolar LSM are shown in Figures 3.2.6 and 3.2.7.

3.2.4 Mutual inductance M_{af}

The reciprocity of mutual inductance effects has been established in reference 3.14 by experiments. It has been shown that for the same saturation conditions the mutual inductance between the field and armature is equal to that between the armature and field. It is more convenient to energise the field winding and calculate the flux linkage with the armature winding and this approach has been adopted.

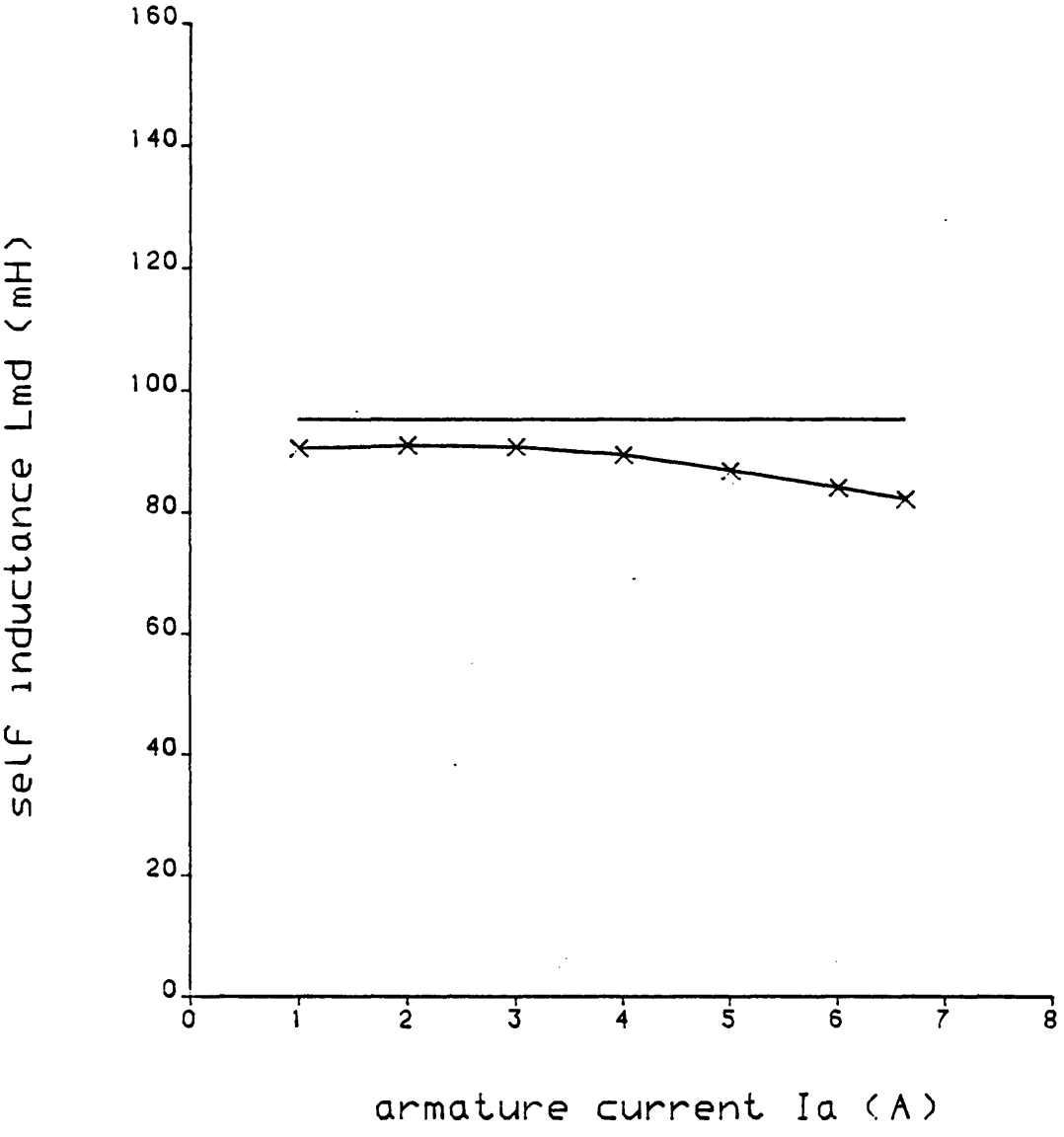

Fig. 3.2.4 D-axis magnetising inductance for round homopolar LSM

———— simple air gap calculation

x—x—x—x—x computing

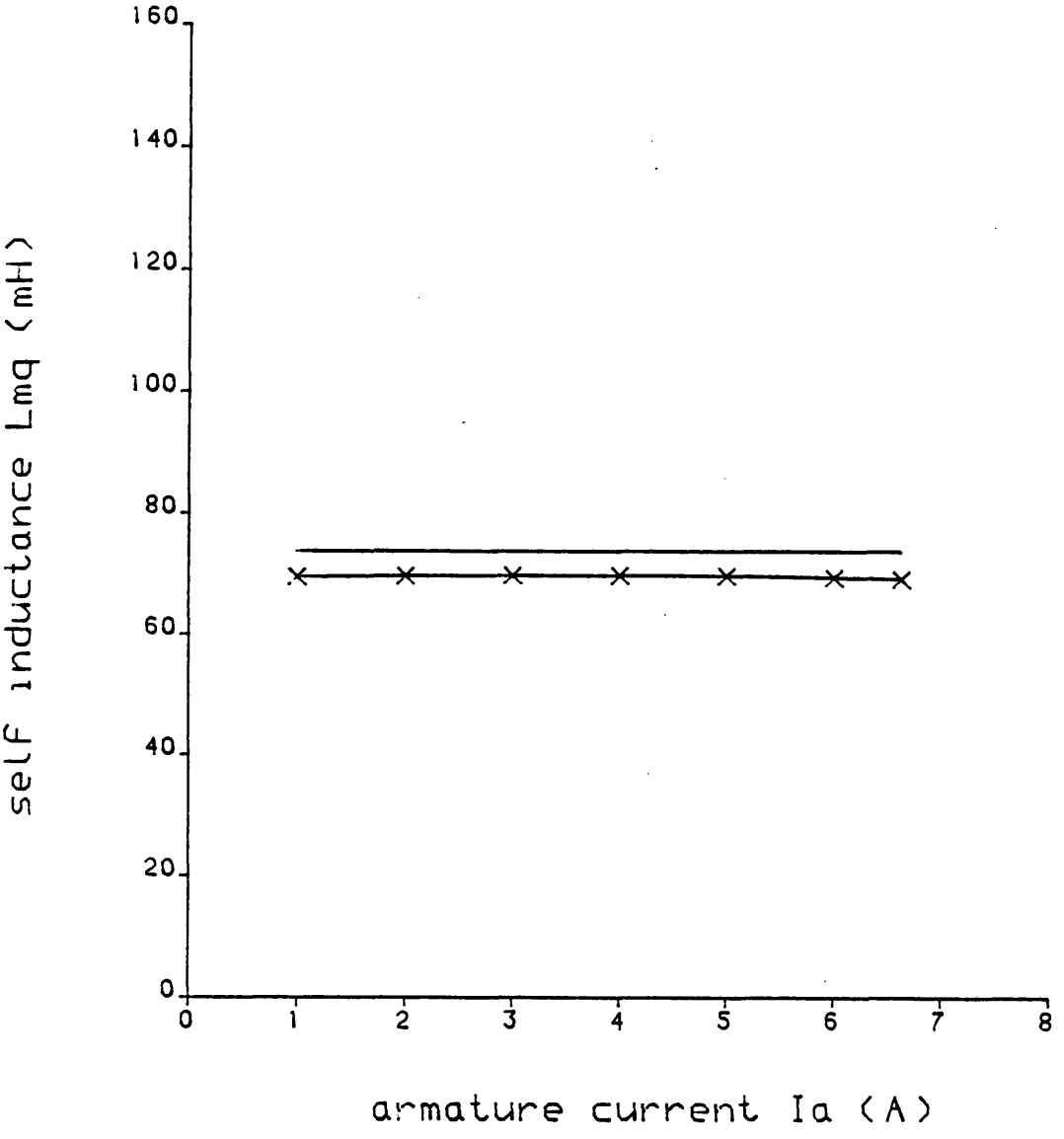

Fig. 3.2.5 Q-axis magnetising inductance for round homopolar LSM

———— simple air-gap calculation

x—x—x—x—x computing

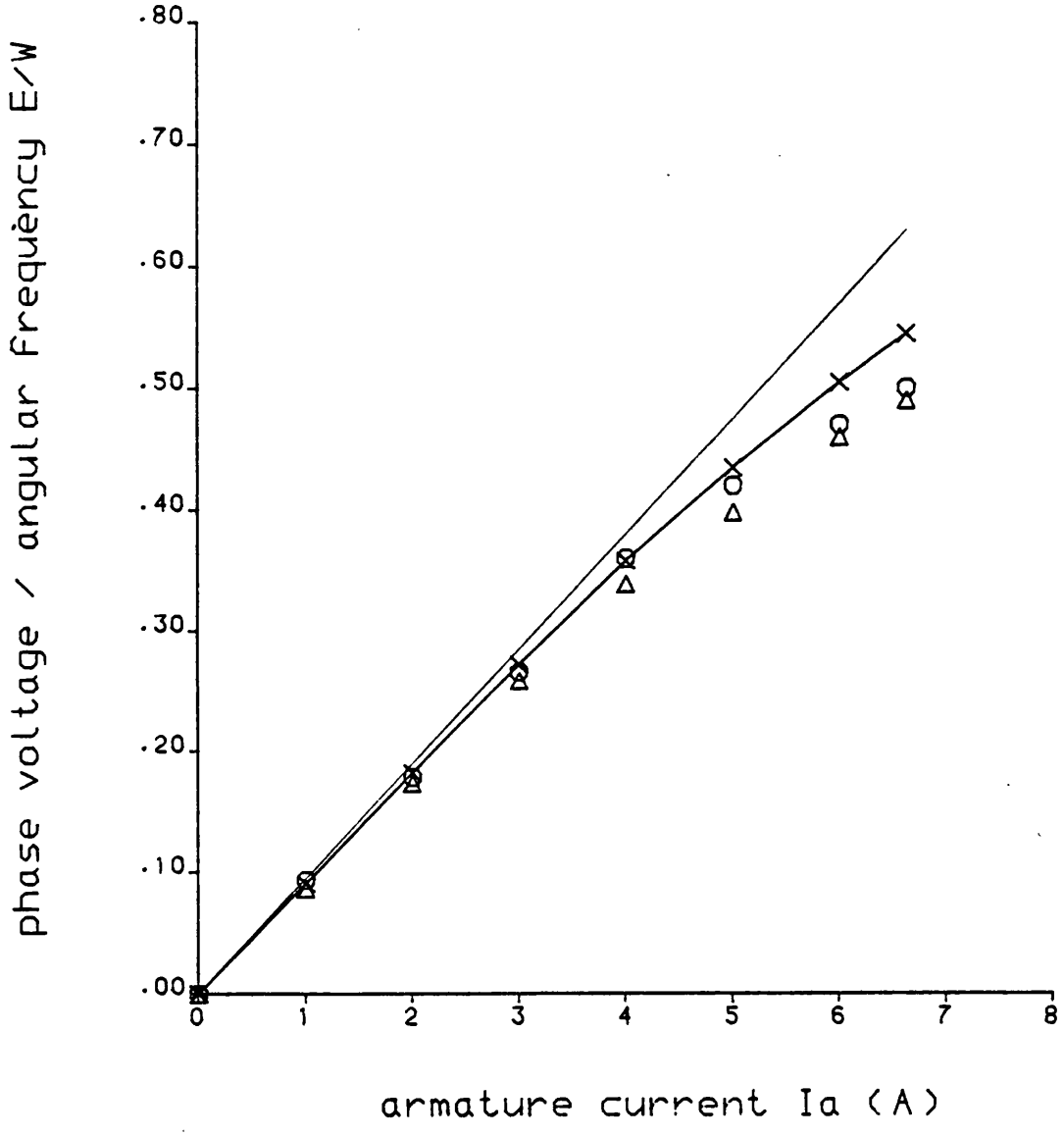

Fig. 3.2.6 D-axis phase voltage for round homopolar LSM

———— simple air-gap calculation

x-x-x-x-x computing

o o o o o measurement at 16.67 Hz

Δ Δ Δ Δ Δ measurement at 83.33 Hz

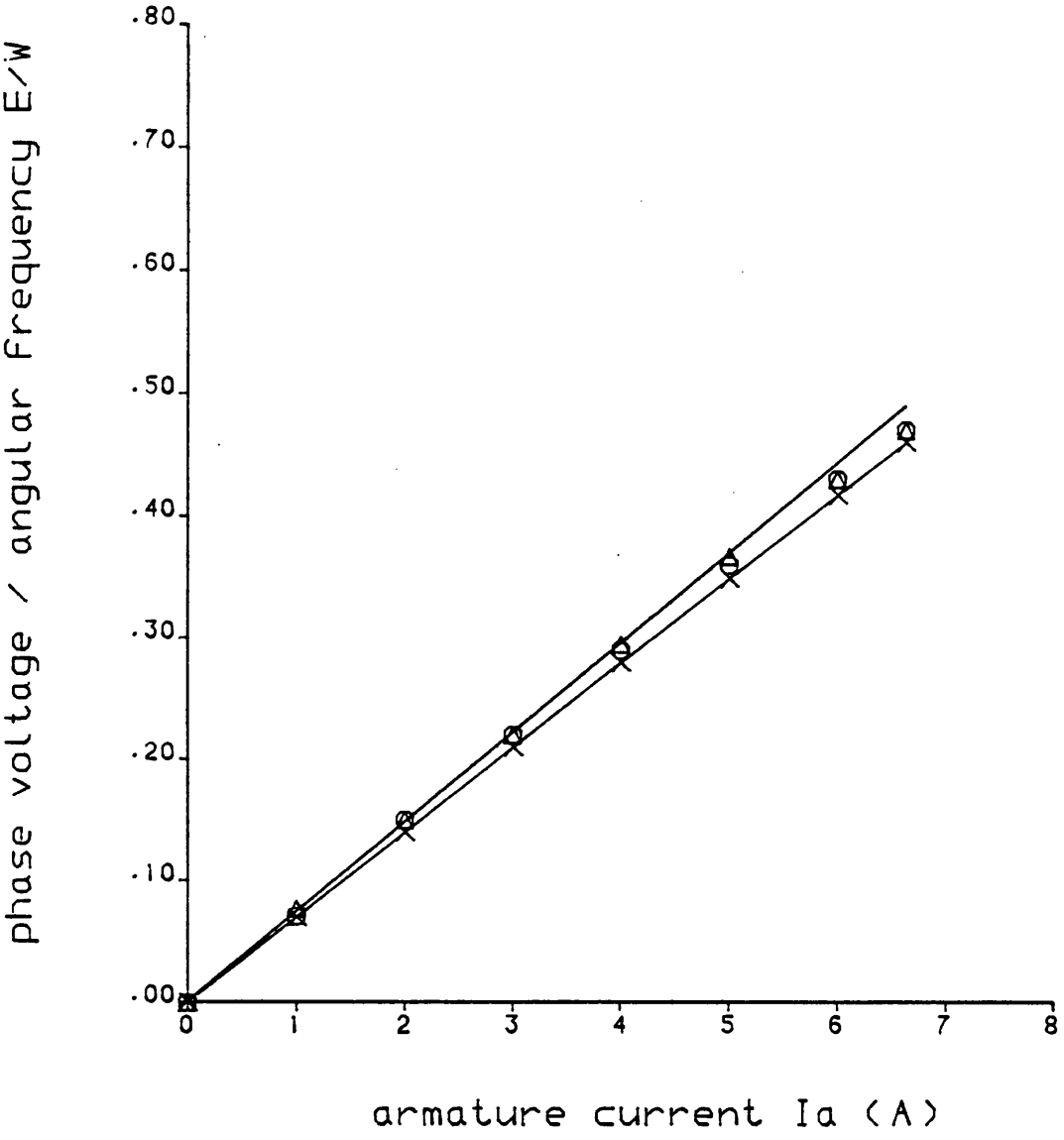

Fig. 3.2.7 Q-axis phase voltage for round homopolar LSM

———— simple air-gap calculation

x—x—x—x—x computing

o o o o o measurement at 16.67 Hz

Δ Δ Δ Δ Δ measurement at 83.33 Hz

In order to calculate M_{af} the armature circuit was assumed to be connected as shown in Fig. 3.2.3. The flux linkage calculated at terminals x-x must be multiplied by a factor $(1/\sqrt{2})$ (see Ref. 3.14) in order to give the correct value per phase.

The flux values used in section 3.2.2 were used for this case. It should be noticed that the rotor must be set in the d-axis position. Referring to Fig. 3.2.1, the flux linkage of the air-gap for 1 pair pole is expressed in terms of ϕ_f and N_a as

$$(\lambda_{af})_{xx} = \sum_{k=1}^{25} \frac{(N_a\phi_f)_{\ell k}}{2} + (N_a\phi_f)_{mk} + \frac{(N_a\phi_f)_{rk}}{2}$$

The mutual inductance at terminals xx for 2P poles is

$$(M_{af})_{xx} = \frac{2P \sum_{k=1}^{25} \frac{(N_a\phi_f)_{\ell k}}{2} + (N_a\phi_f)_{mk} + \frac{(N_a\phi_f)_{rk}}{2}}{\sqrt{2}\, I_f}$$

By using the multiplication factor $(1/\sqrt{2})$, mentioned above, the mutual inductance per phase can be written

$$M_{af} = \frac{P \sum_{k=1}^{25} \frac{(N_a\phi_f)_{\ell k}}{2} + (N_a\phi_f)_{mk} + \frac{(N_a\phi_f)_{rk}}{2}}{I_f} \qquad 3.2.4$$

The mutual inductance obtained by this equation is compared with that obtained from the simplified method (eq. 3.4.1. 4) in Fig. 3.2.8. To confirm this calculation the phase voltage $(E/\omega = M_{af}I_f)$ is also determined and compared with measured values from the homopolar LSM as shown in Fig. 3.2.9.

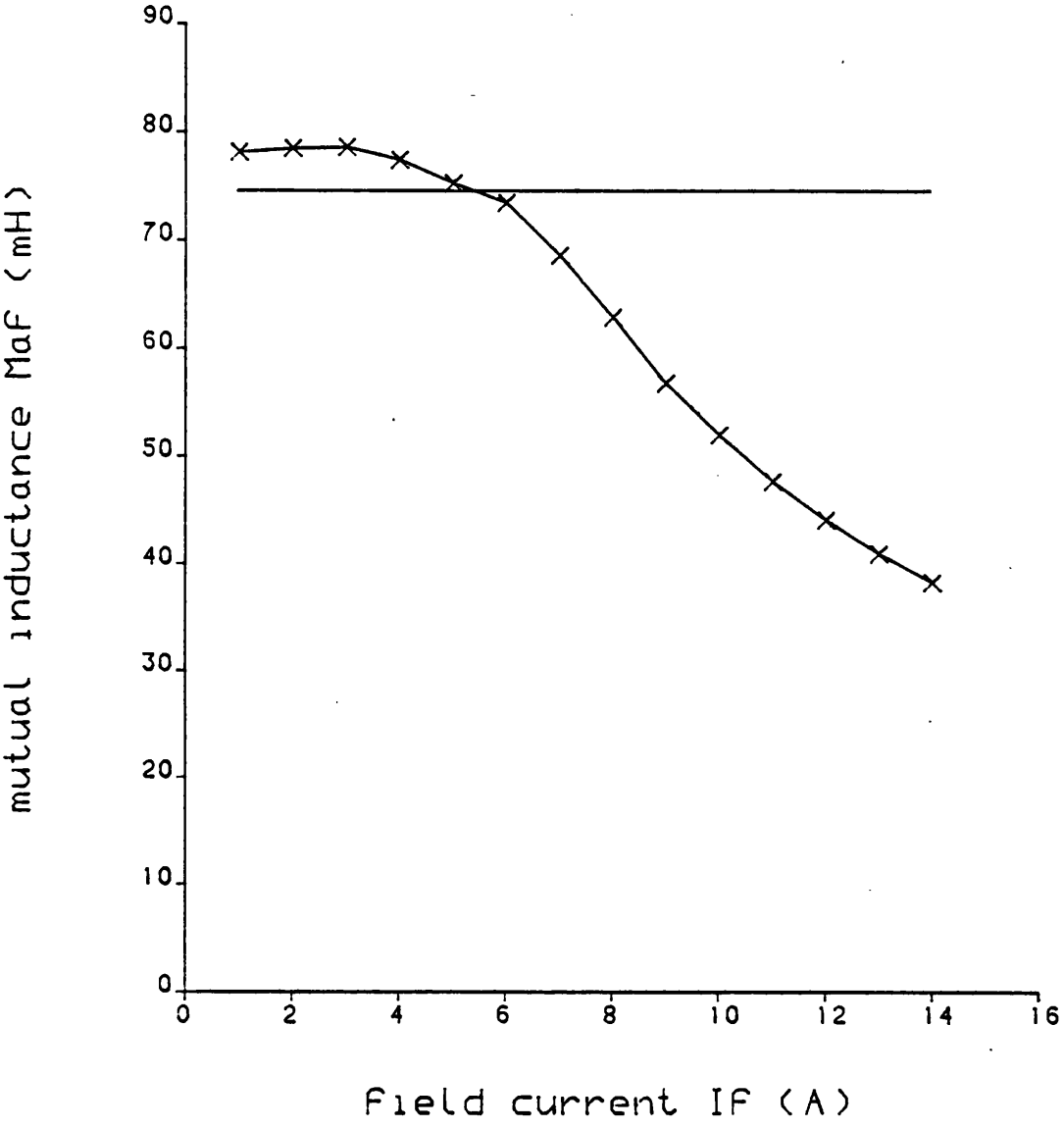

Fig. 3.2.8 Mutual inductance between field and armature winding for round homopolar LSM

———— simple air-gap calculation

x—x—x—x—x computing

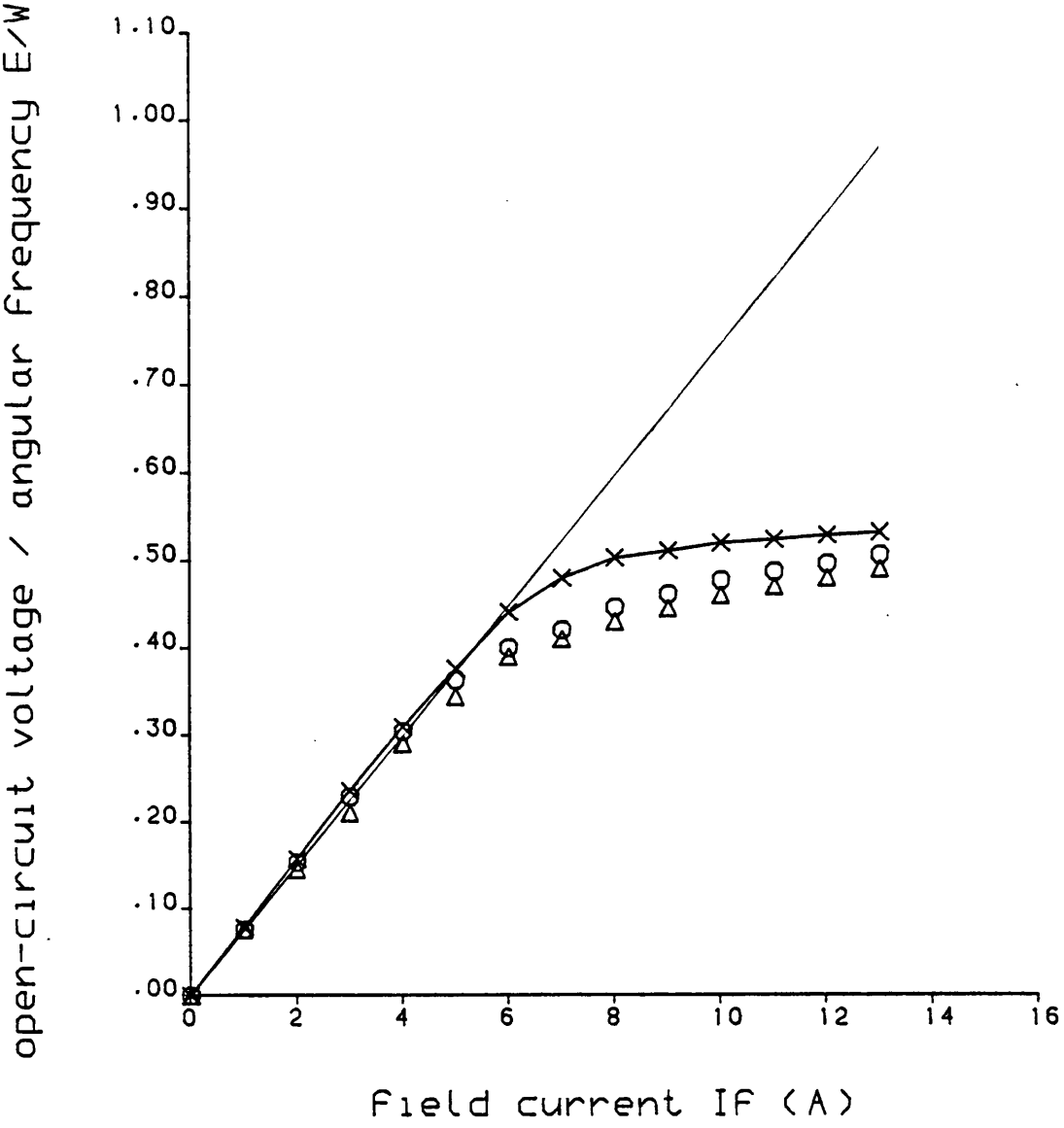

Fig. 3.2.9 Open-circuit characteristic for round homopolar LSM

———— simple air-gap calculation

x-x-x-x-x computing

o o o o o measurement at 16.67 Hz

Δ Δ Δ Δ Δ measurement at 83.33 Hz

3.2.5 Calculation of the inductance components which are considered in the normal force prediction

The calculation of the magnetising inductances of the homopolar LSM using the flux-linkage method based upon a knowledge of the flux distribution in the air-gap. The method has been verified by a comparison of calculated and measured values for generated voltage. There are two components of the air-gap flux; leakage flux and the flux that couples with the field winding. This latter component is responsible for force production and it is calculated by the following method

According to Fig. 3.2.1 the inductances which govern the normal force calculation are found from equations 3.2.2 and 3.2.3 by changing the variation of k to be from 9 to 17 for the d-axis and from 3 to 11 for the q-axis instead of 1 to 25 for both cases. Thus

$$L_{mf} = \frac{2P \sum_{k=9}^{17} \frac{(N_f\phi_f)_{\ell k}}{2} + (N_f\phi_f)_{mk} + \frac{(N_f\phi_f)_{rk}}{2}}{I_f} \qquad 3.2.5.1$$

$$L_{md} = \frac{P \sum_{k=9}^{17} \frac{(N_a\hat{\phi}_a)_{\ell k}}{2} + (N_a\hat{\phi}_a)_{mk} + \frac{(N_a\hat{\phi}_a)_{rk}}{2}}{\sqrt{2}\, I_a} \qquad 3.2.5.2$$

$$L_{mq} = \frac{P \sum_{k=3}^{11} \frac{(N_a\hat{\phi}_a)_{\ell k}}{2} + (N_a\hat{\phi}_a)_{mk} + \frac{(N_a\hat{\phi}_a)_{rk}}{2}}{\sqrt{2}\, I_a} \qquad 3.2.5.3$$

The results of these equations are compared with those obtained from a simple air-gap calculation made using equations 3.4.1.7 , 3.4.2.3 and 3.4.3.2. The results are shown in Figures 3.2.10, 3.2.11 and 3.2.12.

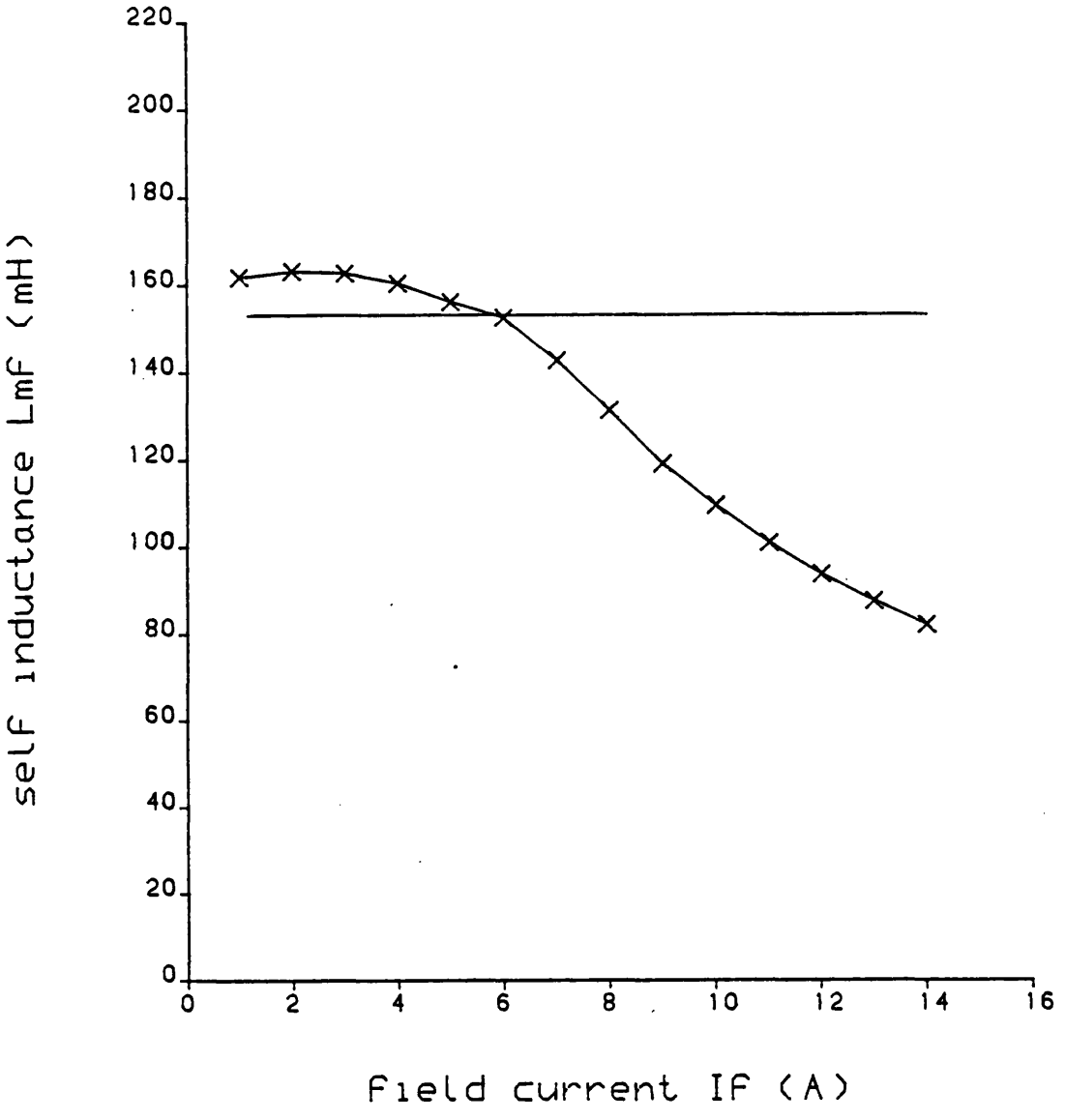

Fig. 3.2.10 Field winding self magnetising inductance for homopolar LSM using actual pole length

———— simple air-gap calculation

x-x-x-x-x computing

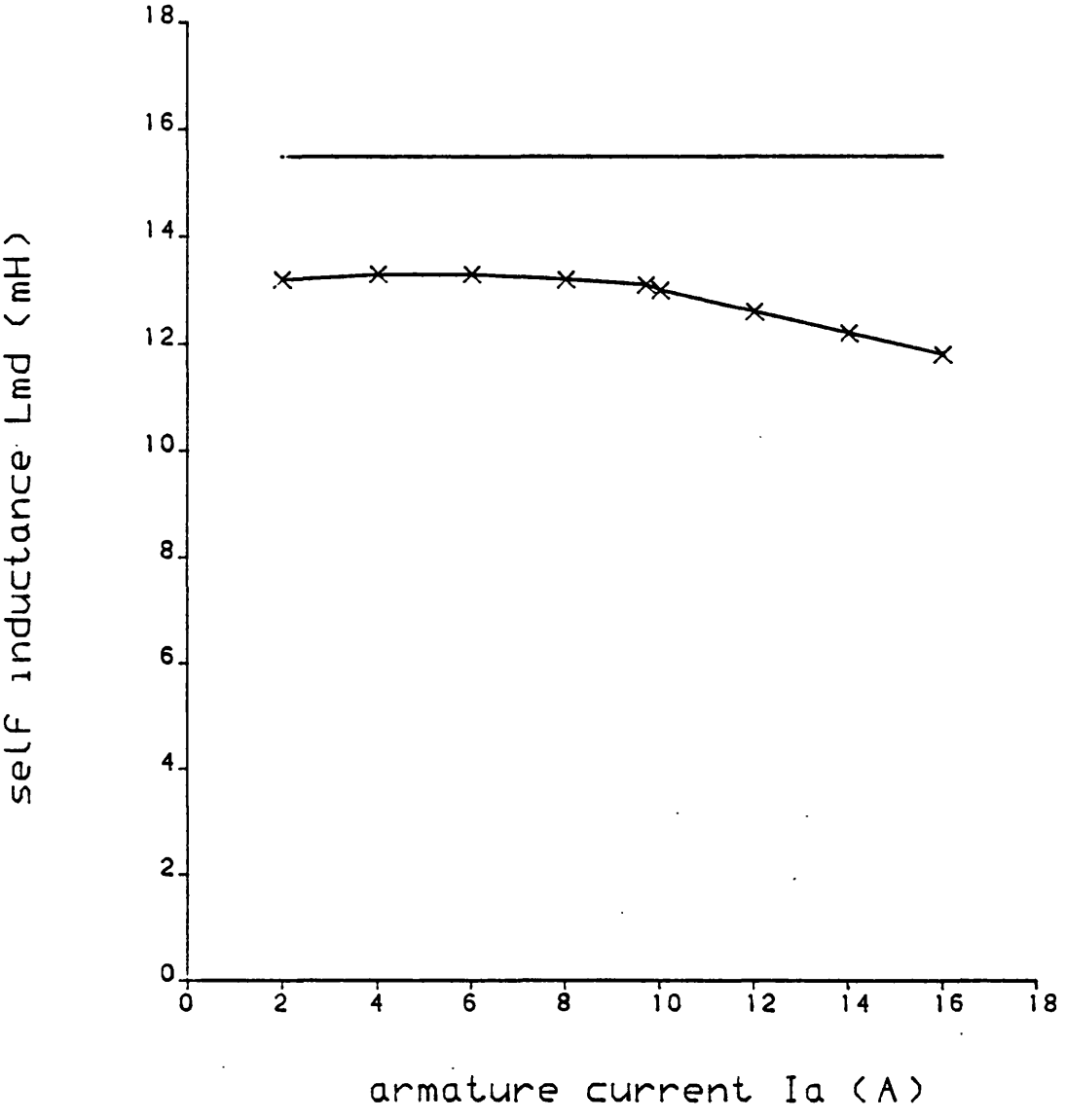

Fig. 3.2.11 D-axis magnetising inductance for homopolar LSM using actual pole length

——————— simple air-gap calculation

x—x—x—x—x computing

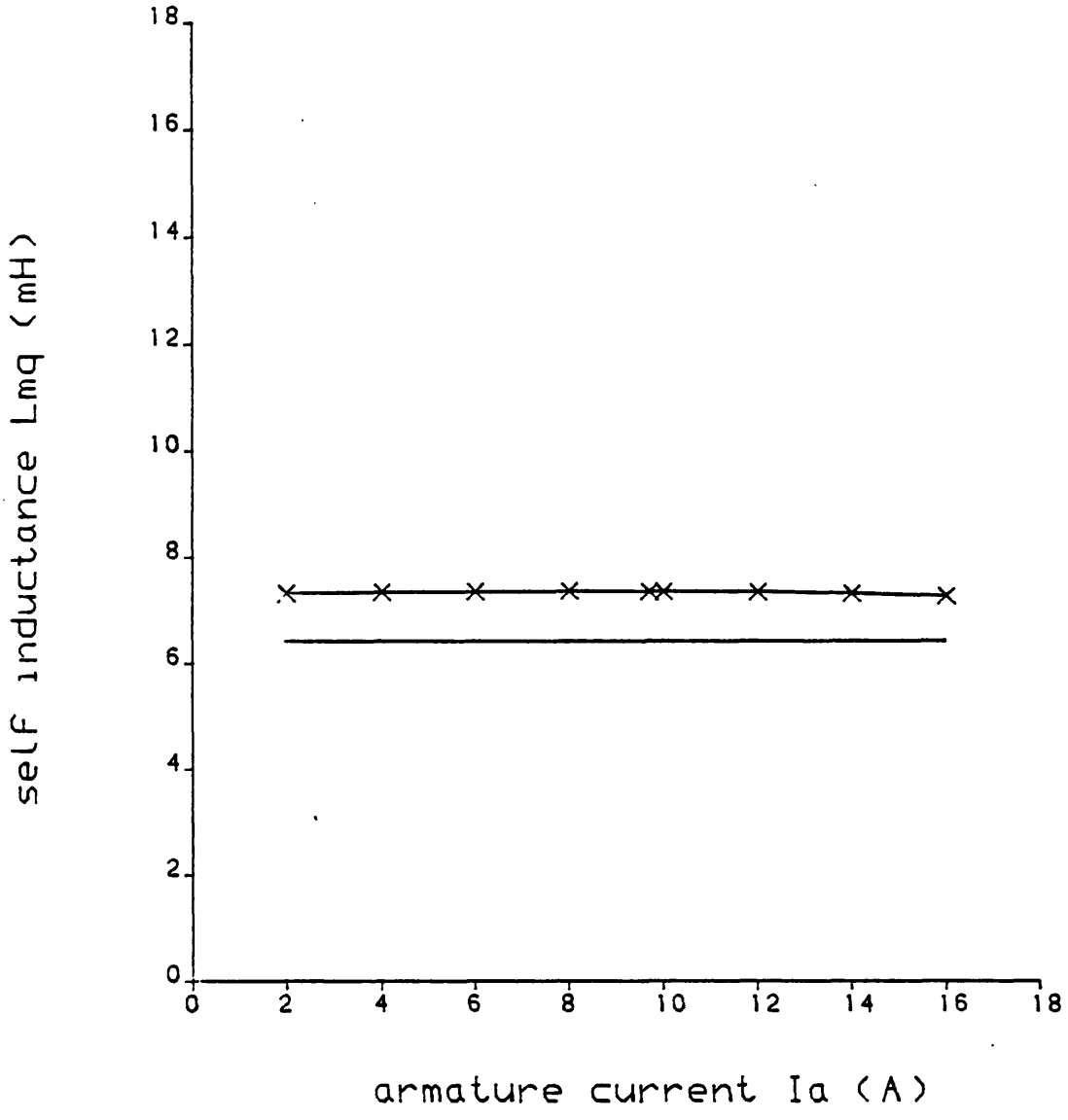

Fig. 3.2.12 Q-axis magnetising inductance for homopolar LSM using actual pole length

———— simple air-gap calculation

x—x—x—x—x computing

A comparison between the normal force obtained using these inductances and measured values will be the subject of the next chapter.

3.3 Discussion and Conclusion

The reason for the values of computed inductance being higher than those given by the simple air-gap calculation (Fig. 3.2.12) is that the fringing flux around the rotor, particularly in the q-axis position is very high. This can be seen clearly by examination of the flux density distribution shown in Fig. 2.7.19. However, the difference between other impedances calculated using the field model and the simple air-gap calculation is considered small enough to justify this use of the simpler method in initial design.

In addition to the variation of mutual inductance (M_{af}) between the field and the armature windings with rotor position, there is a variation with field current (I_f) due to saturation (Fig. 3.2.8). After an initial rise, the mutual inductance decreases very slowly, and when a field current of I_f = 6A is reached, the curve falls off quite rapidly. Because both M_{af} and L_{mf} are proportional to the flux ϕ_f, which is set by field current I_f, the curve of L_{mf} displays a similar behaviour to that of the M_{af} curve as can be seen in Fig. 3.2.2.

The variation of phase voltage with the variation of armature current when the field current is zero and the rotor is in the d-axis is shown in Fig. 3.2.6. The voltage is linear for armature currents up to 3A. Beyond this point the effect of saturation causes L_{md} to slowly decrease (Fig. 3.2.4).

When the rotor is in the q-axis the inductance L_{mq} is constant (Fig. 3.2.5). This is due to the much larger effective air-gap seen by flux in the q-axis.

The above results demonstrate that the field model gives a method for calculating the LSM inductances when saturation is present. It is much more accurate than previous methods which have had to resort to the use of saturation factors[3.2-3.16]. Furthermore, the leakage reactance which results from the air-gap flux that fails to cut the rotor[3.13] has been considered. It may be said that this component of armature leakage reactance has a variation with the relative positions of the iron parts of the LSM, and its value in the quadrature axis is higher than that in the direct axis.

3.4 Appendices

3.4.1 Field winding mutual and self inductance

Fig. 3.4.1 shows the assumed distribution of the air-gap flux density when the field current is I_f. The fringing of the flux at the pole edges has been accounted for in an approximate manner by the use of an effective pole length (ℓ_{1d}). This was calculated using Carter's coefficient for poles of the same polarity (see section 3.4.4). The use of Carter's coefficient in this case is not strictly justified. because of the shallowness of the poles. However its use does give reasonable results[3.17].

In order to calculate the voltage induced in the armature winding the fundamental component of the waveform of Fig. 3.4.1 is used. This is:

$$b_f = \hat{B}_f \sin \frac{\pi x}{\tau_p}$$

where

$$\hat{B}_f = \frac{1}{\tau_p} \int_{\frac{\tau_p - \ell_{1d}}{2}}^{\frac{\tau_p + \ell_{1d}}{2}} B_f \sin \frac{\pi x}{\tau_p} \, dx = \frac{2B_f}{\pi} \sin \frac{\pi \ell_{1d}}{2\tau_p} \qquad (3.4.1.1)$$

The air-gap flux density is

$$B_f = \frac{\mu_o Z_f I_f}{2g} \qquad (3.4.1.2)$$

where $Z_f I_f$ is the field winding mmf.

The pole flux is

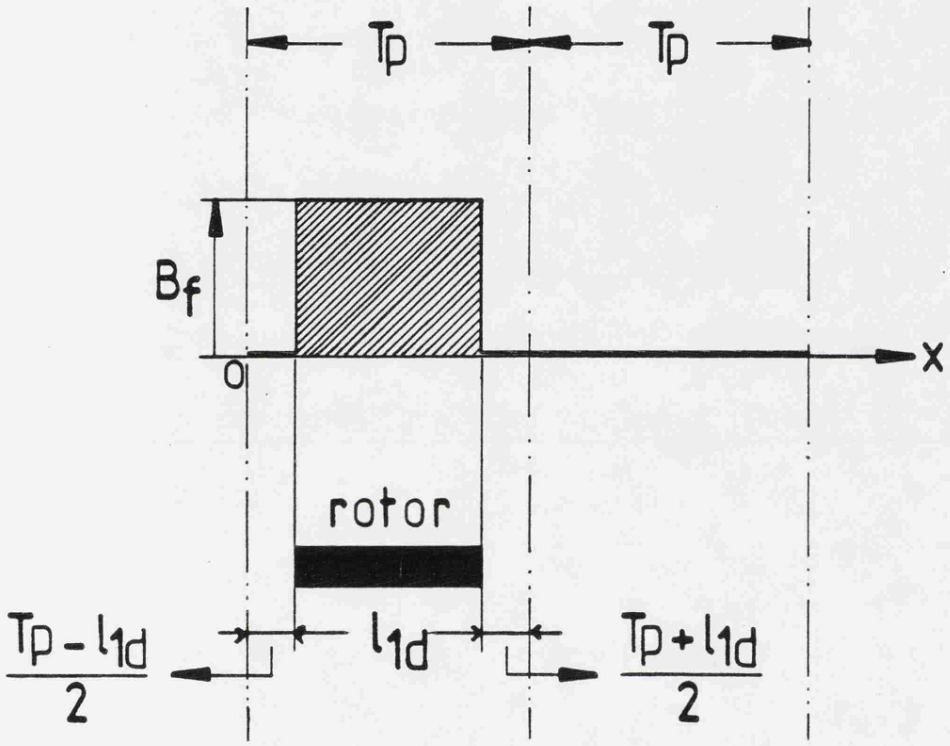

Fig 3·4·1 : Flux density distribution with field excited .

$$\phi_f = \frac{2}{\pi} \hat{B}_f \tau_p w$$

or $$\phi_f = \frac{2\mu_o w \tau_p z_f I_f}{\pi^2 g} \sin \frac{\pi \ell_{1d}}{2\tau_p} \qquad (3.4.1.3)$$

when B_f and $\hat{B}_f$ are eliminated using equations (3.4.1.1) and (3.4.1.2).

The peak induced emf per pole pair is:

$$\hat{E}_1 = \omega (Z_a q k_w) \phi_f$$

where Z_a = series conductors per armature slot

q = slots per pole and phase

k_w = winding factor

The rms induced emf for P pole-pairs on each armature winding and with both windings connected in series is

$$E = 2P\hat{E}_1/\sqrt{2} = \sqrt{2}\, P\omega(Z_a q k_w)\phi_f$$

or

$$E = \frac{\omega\, 2\sqrt{2}\, \mu_o w \tau_p z_f (z_a q k_w) P\, I_f}{\pi^2 g} \sin \frac{\pi \ell_{1d}}{2\tau_p}$$

The phase induced voltage can also be expressed in the form

$$E = \omega M_{af} I_f$$

so that the mutual inductance between the field and armature windings is:

$$M_{af} = \frac{2\sqrt{2}\, \mu_o w \tau_p z_f (z_a q k_w) P}{\pi^2 g} \sin \frac{\pi \ell_{1d}}{2\tau_p} \qquad (3.4.1.4)$$

In order to calculate the field winding self inductance (L_{mf}) the total flux linkage with the winding is required. This is:

$$\lambda_f = \frac{\mu_o w z_f^2 \ell_{1d} P}{2g} I_f$$

and the field self inductance is therefore:

$$L_{mf} = \frac{\mu_o w z_f^2 \ell_{1d} P}{2g} \qquad (3.4.1.5)$$

The normal force components may be evaluated by considering the rate of change of stored energy with a change in gap. An estimate of the force can be obtained by neglecting the change in energy in the fringe and leakage fields. This is accomplished by using the actual pole length in the inductance expressions (3.4.1.4) and (3.4.1.5) which now become

$$M_{af} = \frac{2\sqrt{2}\, \mu_o w \tau_p z_f (z_a q k_w) P}{\pi^2 g} \sin \frac{\pi \ell}{2\tau_p} \qquad (3.4.1.6)$$

$$L_{mf} = \frac{\mu_o w z_f^2 \ell P}{2g} \qquad (3.4.1.7)$$

3.4.2 Armature d-axis self inductance (L_{md})

For this case (Fig. 3.4.2) the fundamental component of the air-gap flux density distribution is:

$$b_d = \hat{B}_d \sin \frac{\pi x}{\tau_p}$$

where

$$\hat{B}_d = \frac{1}{\tau_p} \int_{(\tau_p - \ell_{1d})/2}^{(\tau_p + \ell_{1d})/2} B_a \sin^2 \frac{\pi x}{\tau_p} dx = \frac{B_a}{2} \left[\frac{\ell_{1d}}{\tau_p} + \frac{1}{\pi} \sin \left(\frac{\pi \ell_{1d}}{\tau_p} \right) \right]$$

(3.4.2.1)

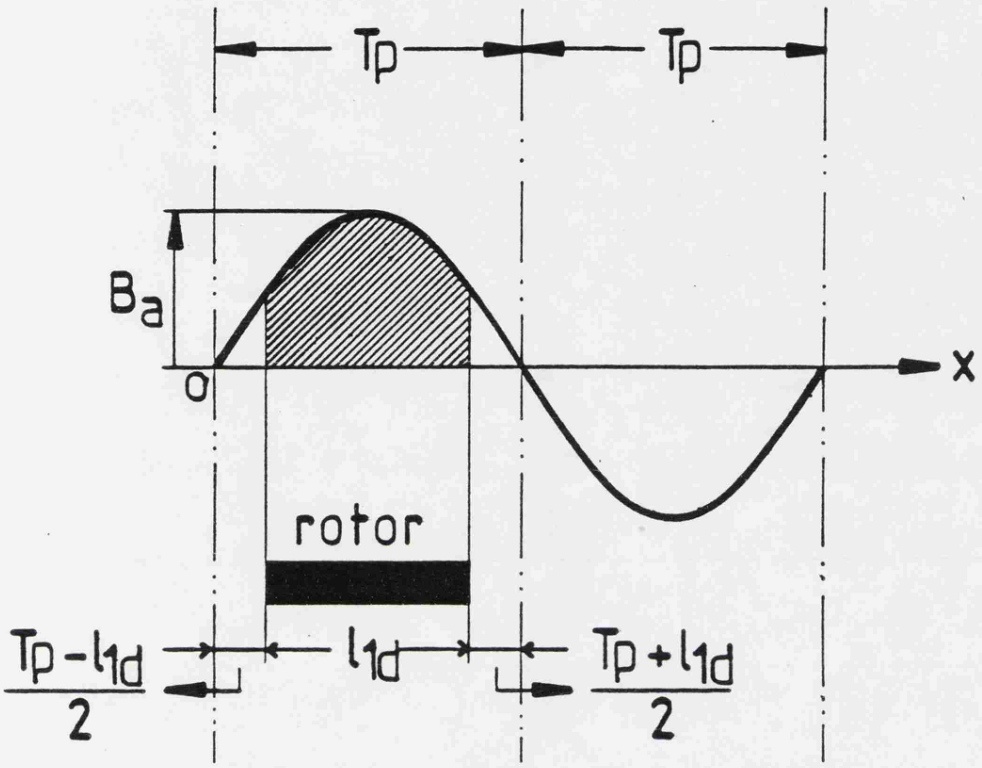

Fig 3·4·2 : d-axis flux density distribution with armature excited .

In this expression the effective pole length ℓ_{1d} has again been used since the poles are of the same polarity.

The peak flux density at the peak armature current ($\hat{I}$) is

$$B_a = \frac{\mu_o}{g} \cdot \frac{3(z_a q k_w)}{\pi} \hat{I}$$

Substituting this into (3.4.2.1) gives:

$$\hat{B}_d = \frac{3\mu_o (z_a q k_w)\hat{I}}{2\pi g} \left[\frac{\ell_{1d}}{\tau_p} + \frac{1}{\pi} \sin \left(\frac{\pi \ell_{1d}}{\tau_p} \right) \right]$$

The pole flux is:

$$\phi_d = \frac{2}{\pi} \hat{B}_d \tau_p w$$

and the peak induced emf per pole pair is then:

$$\hat{E}_1 = \omega (z_a q k_w) \phi_d$$

The peak induced emf for P pole-pairs on each armature winding and with both windings connected in series is

$$\hat{E} = 2P\hat{E}_1 = 2P\omega (z_a q k_w) \phi_d$$

or

$$\hat{E} = \frac{\omega 6 \mu_o w \tau_p (z_a q k_w)^2 P \hat{I}}{\pi^2 g} \left[\frac{\ell_{1d}}{\tau_p} + \frac{1}{\pi} \sin \left(\frac{\pi \ell_{1d}}{\tau_p} \right) \right]$$

The phase induced voltage can also be expressed in the form

$$\hat{E} = \omega L_{md} \hat{I}$$

so that the inductance is

$$L_{md} = \frac{6\mu_o w \tau_p (z_a q k_w)^2 P}{\pi^2 g} \left[\frac{\ell_{1d}}{\tau_p} + \frac{1}{\pi} \sin \left(\frac{\pi \ell_{1d}}{\tau_p} \right) \right] \qquad (3.4.2.2)$$

When estimating the force the actual pole length is used. Equation (3.4.2.2) now becomes

$$L_{md} = \frac{6\mu_o w \tau_p (z_a q k_w)^2 P}{\pi^2 g} \left[\frac{\ell}{\tau_p} + \frac{1}{\pi} \sin \left(\frac{\pi \ell}{\tau_p} \right) \right] \qquad (3.4.2.3)$$

3.4.3 Armature q-axis self inductance (L_{mq})

The air-gap flux density distribution for this case (Fig. 3.4.3) has two components. The larger component (B_a) appears where the pole is present. Its magnitude is given by

$$B_a = \frac{\mu_o}{g} \cdot \frac{3(z_a q k_w)}{\pi} \hat{I}$$

as in Section 3.4.2.

In addition to the larger, main flux distribution there is a smaller, leakage flux component (B'_a). This flux passes between adjacent poles on the same armature winding. The magnitude of B'_a can be estimated by assuming that the exposed portion of the armature winding can be treated as an open-sided machine[3.13]. In this case the flux is assumed to cross a gap of length (g') where

$$g' = \frac{\tau_p}{\pi}$$

The q-axis magnetising inductance is evaluated using the same procedure as adopted in Section 3.4.2. In this case, however, the effective pole length (ℓ_{1q}) is calculated for poles of opposite polarity. The inductance value is

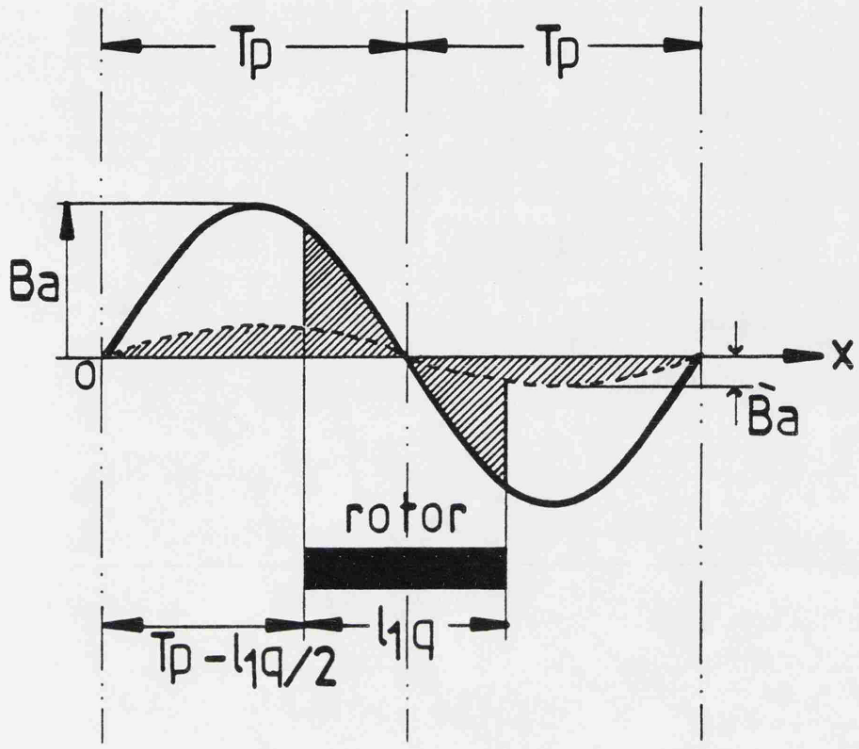

Fig 3·4·3 : q-axis flux density distribution with armature excited .

$$L_{mq} = \frac{6\mu_o w \tau_p (z_a q k_w)^2 p}{\pi^2} \left\{ \left(\frac{1}{g} - \frac{1}{g'} \right) \left[\frac{\ell_{1q}}{\tau_p} - \frac{1}{\pi} \sin \left(\frac{\pi \ell_{1q}}{\tau_p} \right) \right] + \frac{2}{g'} \right\} \qquad (3.4.3.1)$$

When calculating attractive force, the rate of change of inductance with gap is required. Since the leakage flux is independent of gap and the change in fringing flux is being ignored, equation (3.4.3.1) can be simplified to

$$L_{mq} = \frac{6\mu_o w \tau_p (z_a q k_w)^2 p}{\pi^2 g} \left[\frac{\ell}{\tau_p} - \frac{1}{\pi} \sin \left(\frac{\pi \ell}{\tau_p} \right) \right] \qquad (3.4.3.2)$$

3.4.4 Carter's coefficients

Carters's coefficients are used in this chapter to calculate the effective pole length in order to take fringing effects into account. The calculation of the field and d-axis inductances require the use of the coefficient for poles of the same potential, and that of the q-axis inductance the use of the coefficient for poles of opposite potential.

As shown in Figures 3.4.4 and 3.4.5 width (w_1) is added to the pole length to account for the fringing flux at the edge of the pole. This width can be expressed[3.18] in terms of the air-gap fraction λ.

$$w_1 = \lambda g \qquad (3.4.4.1)$$

where g is the air-gap length.

3.4.4.1 Poles of the same polarity

Fig. 3.4.4 shows two poles of the same polarity where s is the distance between these two poles. According to Carter, the fraction λ of the length of the air-gap is given by

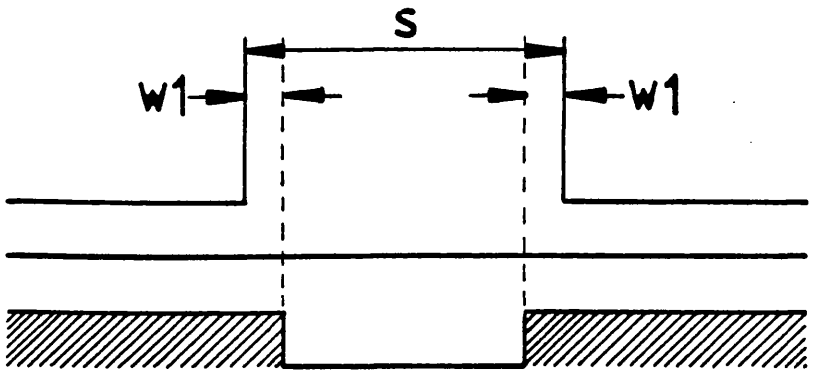

Fig 3·4·4 : Poles of same potential

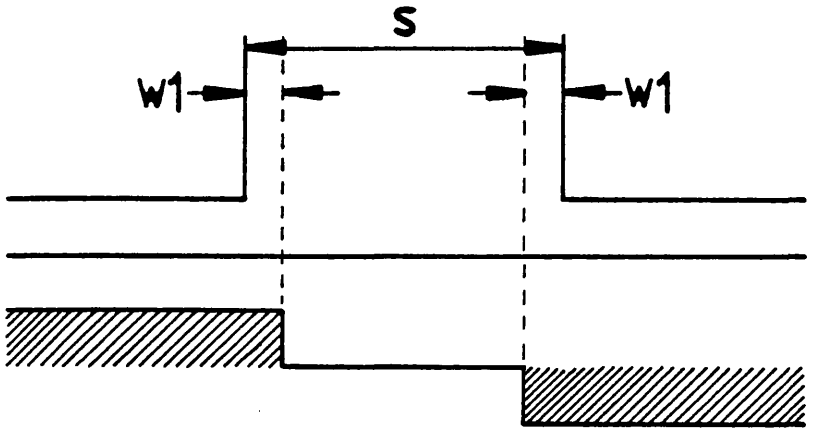

Fig 3·4·5 : Poles of opposite potential

$$\lambda = \left(\frac{s}{2g}\right) - \frac{1}{90}\left(\frac{s}{2g}\right)\tan^{-1}\left(\frac{s}{2g}\right) + \frac{2.3}{\pi}\log\left[1 + \left(\frac{s}{2g}\right)^2\right] \quad (3.4.4.2)$$

The machine under consideration has the following dimensions:

ℓ = 0.0635 m, the actual pole length

s = 0.127 m

g = 3.175×10^{-3} m

using equation 3.4.4.2 and then 3.4.4.1, w_1 is found to be

$$w_1 = 8.096 \times 10^{-3} \text{ m}$$

therefore

$$\ell_{1d} = \ell + 2w_1 = \underline{0.0797 \text{ m}}$$

where ℓ_{1d} is the effective pole length taking the fringing effects into account.

3.4.4.2 Poles of opposite polarity

The two poles of opposite polarity, shown in Fig. 3.4.5 are considered when calculating the q-axis inductance. The fraction λ of the length of the air-gap for this case is[3.18]:

$$\lambda = \frac{1}{90}\left(\frac{s}{2g}\right)\tan^{-1}\left(\frac{2g}{s}\right) + \frac{2.3}{\pi}\log\left\{\frac{1}{4}\left[1 + \left(\frac{s}{2g}\right)^2\right]\right\} \quad (3.4.4.3)$$

Using this expression with equation 3.4.4.1, the effective pole length ℓ_{1q} is found to be

$$\ell_{1q} = \ell + 2w_1 = \underline{0.0769 \text{ m}}$$

References

3.1 Rankin, A.W.:
"The direct and quadrature axis equivalent circuits of the synchronous machines", AIEE Transactions, vol.64, 1945, pp.861-868.

3.2 Kilgore, L.A.:
"Calculation of synchronous machine constants reactances and time constants affecting transient characteristics", Transactions AIEE, vol.50, 1931, pp.1201-1214.

3.3 Alger, P.L.:
"The calculation of the armature reactance of synchronous machines", Transactions AIEE, vol.47, 1928, pp.493-513.

3.4 Park, R.H. and Robertson, B.L.:
"The reactances of synchronous machines", Transactions AIEE, vol.47, 1928, pp.514-536.

3.5 Rankin, A.W.:
"Per-unit impedances of synchronous machines", Transactions AIEE, vol.64, 1945, pp.839-841.

3.6 Rankin, S.W.:
"Per-unit impedances of synchronous machines - II", Transactions AIEE, vol.42, 1923, pp.839-841.

3.7 Doherty, R.E.:
"A simplified method of analyzing short-circuit problems", Transactions AIEE, vol.42, 1923, pp.841-849.

3.8 Wieseman, R.W.:

"Graphical determination of magnetic field, practical applications to salient-pole synchronous machine design", Transactions AIEE, vol.46, 1927, pp.141-154.

3.9 Park, R.H.:

"Two reaction theory of synchronous machine, Part I, Generalized method of analysis", Transactions AIEE, vol.48, 1929, pp.716-730.

3.10 Kilgore, L.A.:

"Effect of saturation on machines reactances", Transactions AIEE, vol.54, 1935, pp.545-550, and Disc. 1935, pp.1113-1118.

3.11 Shepherd, R.V. and Kilbourne, C.E.:

"The quadrature synchronous reactance of salient pole synchronous machines", Transactions AIEE, vol.62, 1943, pp.684-689, and Disc. p.926.

3.12 Fuchs, E.F. and Erdelyi, E.A.:

"Determination of waterwheel alternator steady state reactances from flux plot", IEEE Summer Power Meeting, July 1971, pp.2510-2527, Paper No. TP596.

3.13 Laithwaite, E.R.:

"Induction Machines for Special Purposes", Newnes, 1966.

3.14 Jones, E.V.:

"The Unified Theory of Electrical Machines", 1967.

3.15 Kimbark, E.W.:

"Power System Stability Synchronous Machines", 1968.

3.16 Rader, L.J. and Litscher, E.C.:
"Some aspects of inductance when iron is present", Transactions AIEE, vol.62, 1943, pp.684-689.

3.17 Balchin, M.J. and Eastham, J.F.:
"Characteristics of a heteropolar linear synchronous machine with passive secondary", IEE J. Electr. Power Appl. (GB), vol.2, No.6, pp.213-218, (Dec 1979).

3.18 Carter, F.W.:
"Note on air-gap and interpolar induction", Journal IEE, 1900, vol.29, pp.925-933.

CHAPTER 4

CALCULATION OF MECHANICAL FORCES

4.1 Introduction

One method for finding the forces acting on material in a magnetic field starts with the principle of conservation of energy. Electrical energy input and the increase in the magnetic energy are calculated and it is assumed that the difference of these quantities gives the work done by magnetic forces on bodies which are displaced. This procedure was followed by Doherty and Park in reference 4.1.

Conservation of energy considerations were used in reference 4.2 to estimate the forces produced in a heteropolar LSM. The expressions developed for this machine are applied in section 4.2 to give an estimate of the forces in the homopolar LSM under saturated conditions.

Section 4.3 gives an approximate method for calculating rate of change of stored energy, and hence force, directly from a flux plot.

The other method used for force calculations relies on the concept of "Maxwell Stress". Carpenter[4.3-4.4] has used Maxwell's stresses to calculate mechanical forces on iron members situated in a magnetic field. The stress distribution has to be integrated over a closed surface surrounding the member of interest. In section 4.4 of this chapter the LSM forces are calculated by surrounding the rotor poles with a closed surface.

4.2 Calculation of Mechanical Forces by using Inductances

4.2.1 Introduction

The force between two circuits is derived from conservation of energy considerations as[4.1]

$$f_x = \frac{1}{2} I_1^2 \frac{dL_1}{dx} + I_1 I_2 \frac{dM}{dx} + \frac{1}{2} I_2^2 \frac{dL_2}{dx} \qquad 4.2.1.1$$

Where I_1 and I_2, L_1 and L_2 are the currents and inductance coefficients of the two circuits and *M*, the mutual inductance between them. f_x is the component of force in the x direction.

4.2.2 Calculation of normal force

To calculate the normal force for the homopolar LSM, it is more convenient to use the following expression developed in reference 4.2.

$$F_n = \frac{I_f^2}{2g} L_{mf} + \frac{3I_a^2(L_{md} + L_{mq})}{4g} + \frac{3I_f I_a}{g} M_{af} \cos \delta_i + \frac{3I_a^2(L_{md} - L_{mq})}{4g} \cos 2\delta_i \qquad 4.2.2.1$$

This expression uses the approximation that each of the air-gap inductances depends only on the inverse of g.

The inductance coefficients for a particular case (and in the absence of end effects) are evaluated using either a simple air-gap calculation or from a field plot.

The comparison between calculated forces and those measured at low speed has been made for each of the following cases:

1. Armature current zero

$$F_n = \frac{1}{2g} L_{mf} I_f^2 \qquad 4.2.2.2$$ shown in Fig.4.2.2.1

2. Field current zero

$$F_n = \frac{3I_a^2}{4g} \left[(L_{md} + L_{mq}) + (L_{md} - L_{mq}) \cos 2\delta_i \right] \qquad 4.2.2.3$$

This equation has two following cases:

a) δ_i, torque angle is equal to 0^o (D-axis)

$$F_n = \frac{3}{2g} L_{md} I_a^2 \qquad 4.2.2.4 \text{ , Fig.4.2.2.2}$$

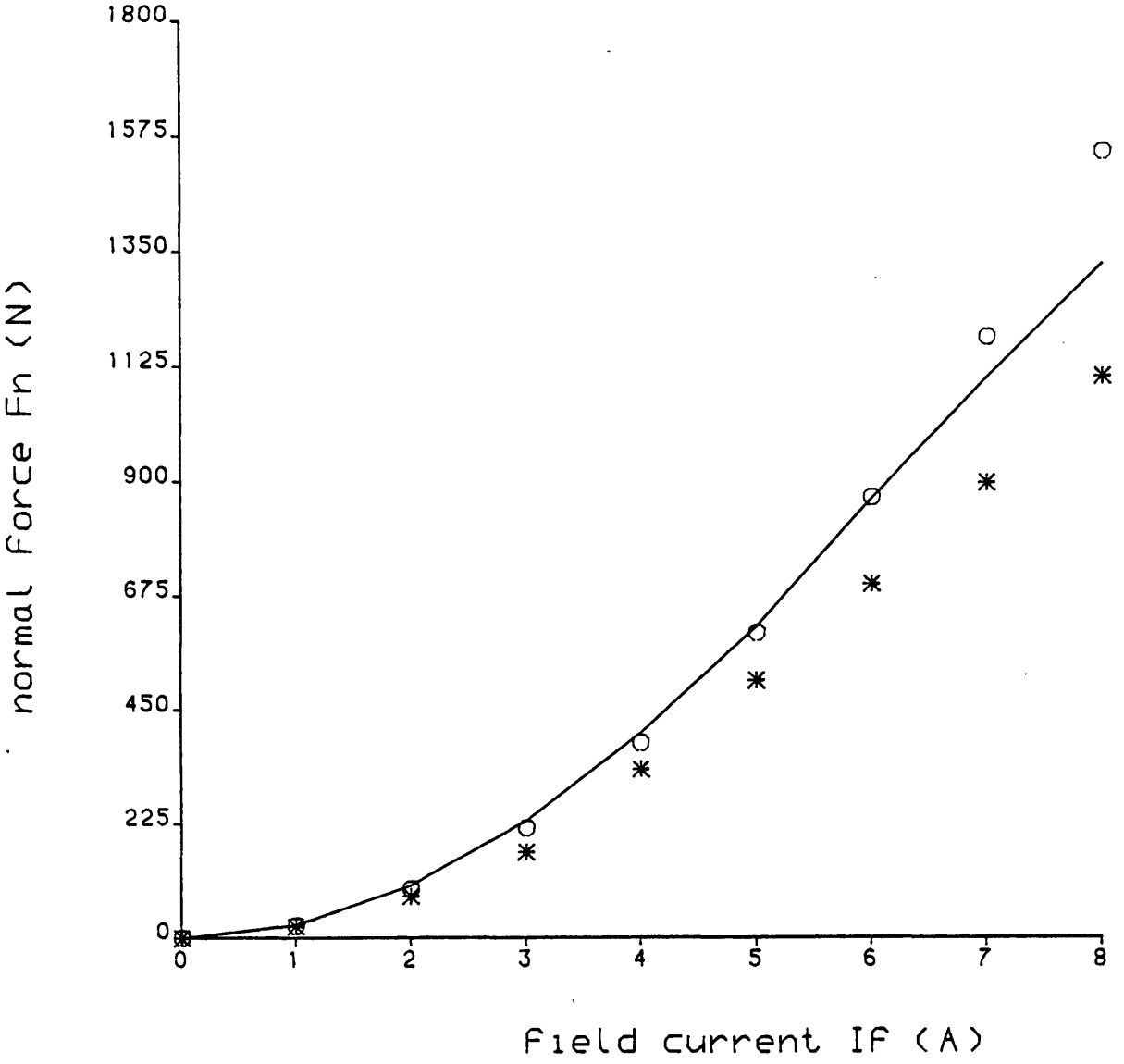

Fig. 4.2.2.1 Normal force due to field current by the use of inductance L_{mf}

o o o o o simple air-gap calculation

———— computing

* * * * * measurement at 16.67 Hz

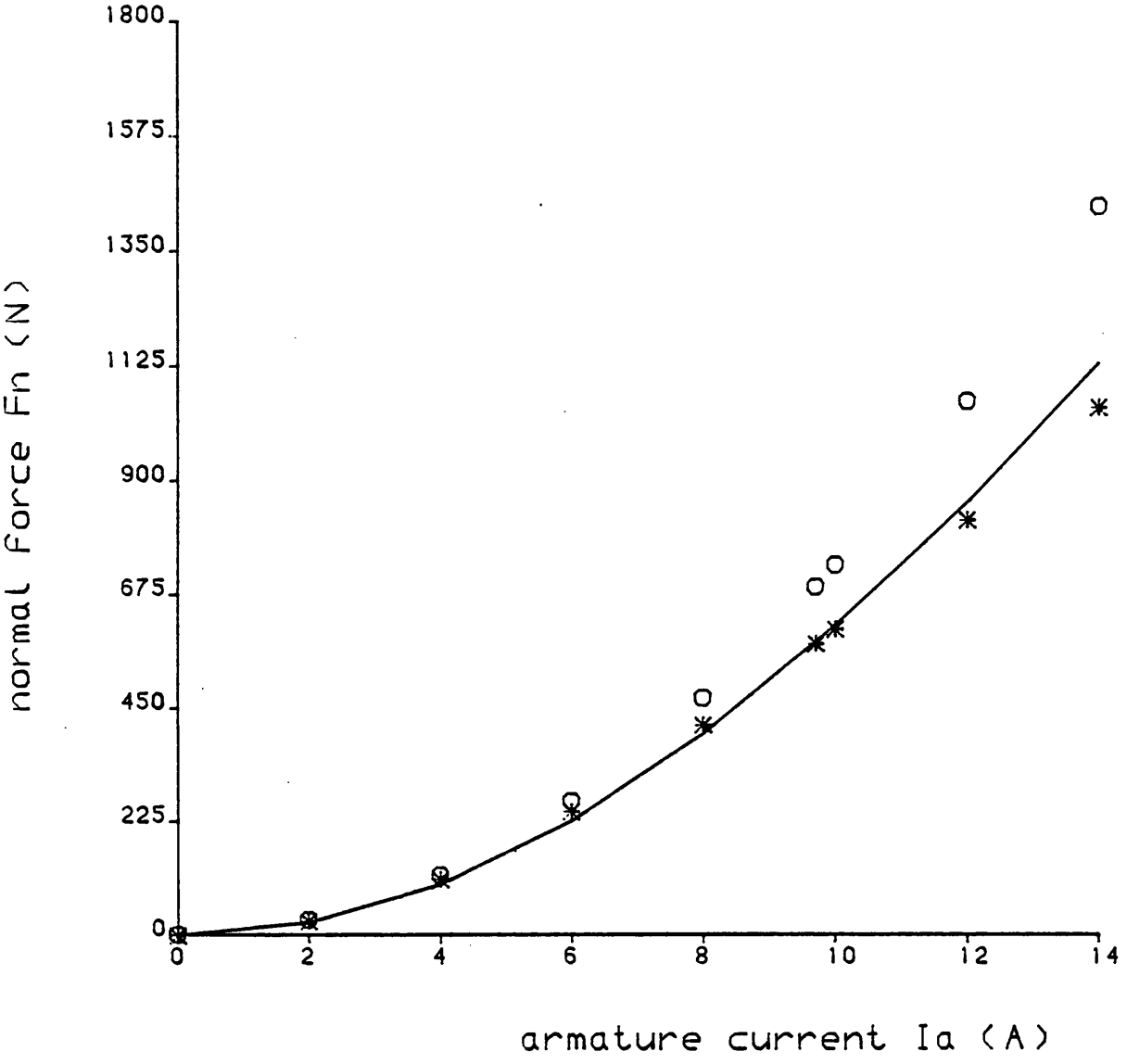

Fig. 4.2.2.2 D-axis normal force due to armature current by the use of inductance L_{md}

o o o o o simple air-gap calculation

——————— computing

* * * * * measurement at 16.67 Hz

b) δ_i, torque angle is equal to 90^o (Q-axis)

$$F_n = \frac{3}{2g} L_{mq} I_a^2 \qquad 4.2.2.5 \text{ , Fig.4.2.2.3}$$

3. In the case when both field and armature currents are applied, the inductance must be recalculated since the saturation conditions have altered. This case is not shown.

4.2.3 Calculation of thrust force

An expression for thrust in terms of winding currents and torque angle can be obtained by equating air-gap power to mechanical output. The following expression was derived in reference 4.2 .

$$F_T = \frac{3\pi}{\tau_p} M_{af} I_f I_a \sin \delta_i + \frac{3\pi}{2\tau_p} (L_{md} - L_{mq}) I_a^2 \sin 2\delta_i \qquad 4.2.3.1$$

By using constant currents of 5 amps and 9.7 amps, respectively, for the field and armature windings, and also considering the air-gap values of inductance coefficients M_{af}, L_{md} and L_{mq} corresponding to those currents, which were obtained in the previous chapter, the equation 4.2.3.1 gives the thrust as a function of the single variable δ_i as shown in Fig.4.2.3.1. The dependence is seen to consist of a fundamental term and a second harmonic. The second harmonic term represents the reluctance power due to saliency, and is present even when the excitation is removed. It depends upon the difference between d-axis and q-axis inductances and thus disappears in a non-salient pole machine. It should be noted that, theoretically, the maximum thrust would occur at a torque angle δ_i of 90^o. At this angle, the theoretical maximum thrust is $3\pi M_{af} I_f I_a / \tau_p$.

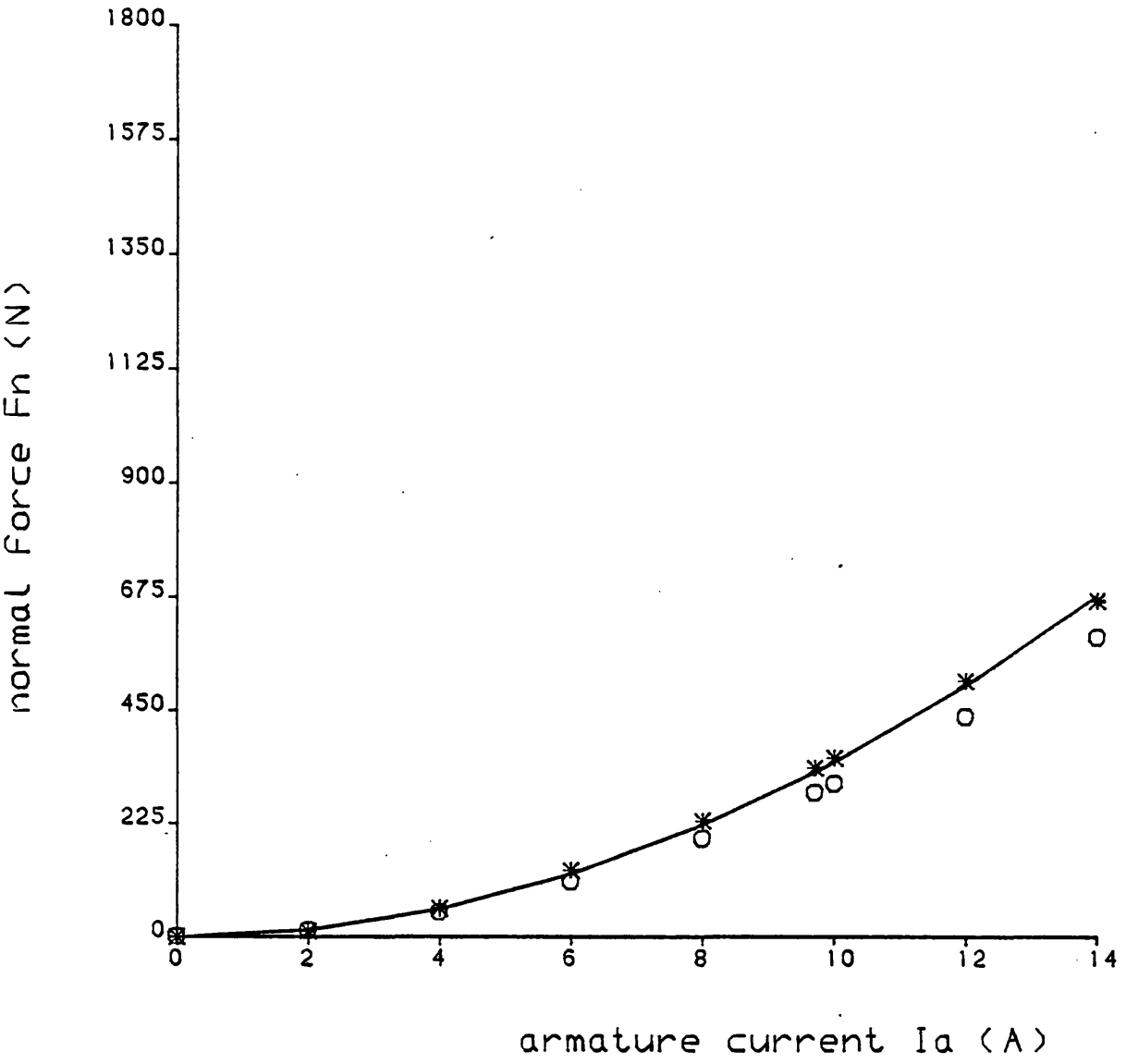

Fig. 4.2.2.3 Q-axis normal force due to armature current by the use of inductance L_{mq}

o o o o o simple air-gap calculation

——————— computing

* * * * * measurement at 16.67 Hz

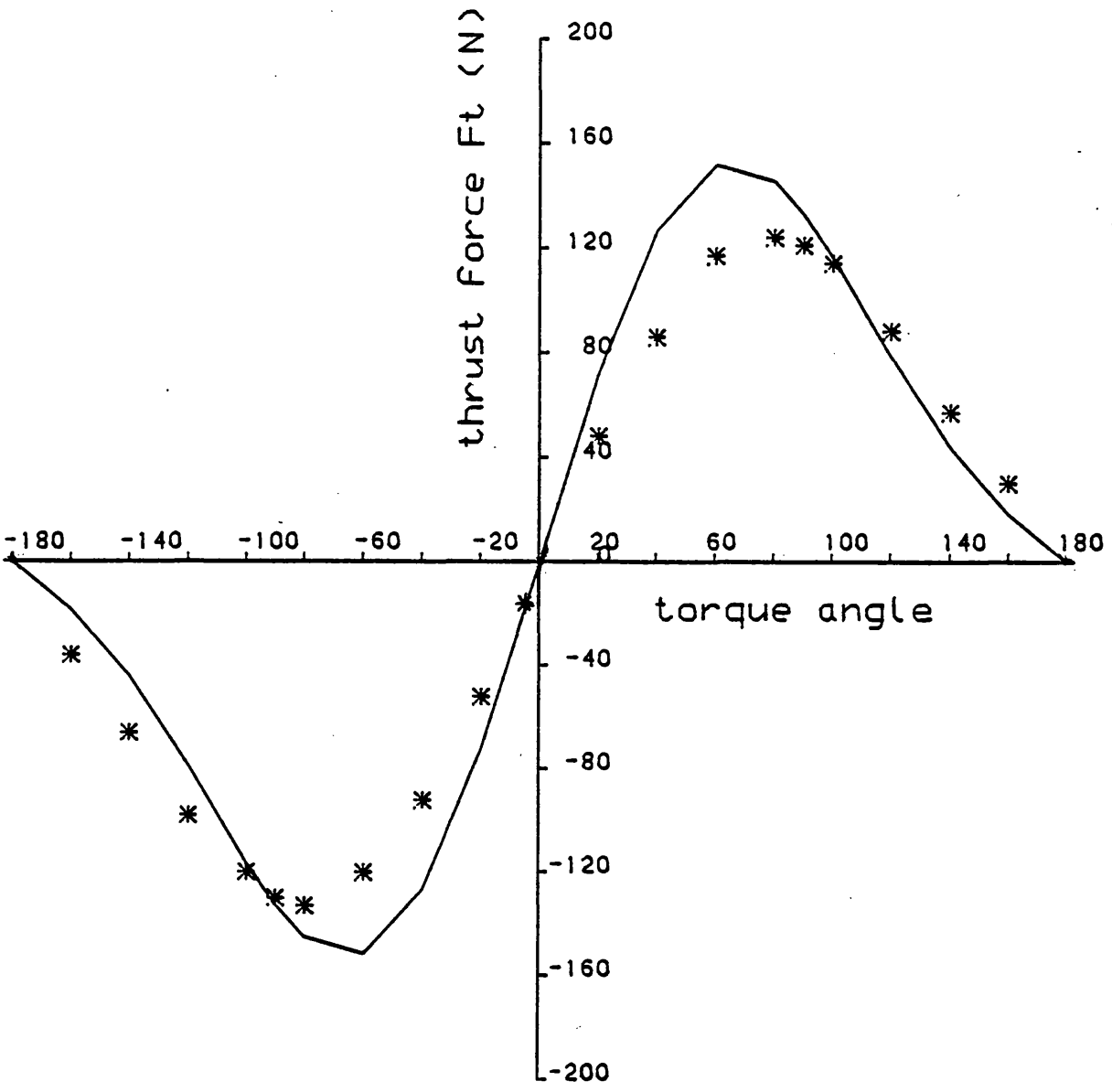

Fig. 4.2.3.1 Thrust force due to field current of 5 amps and armature current of 9.7 amps by the use of inductance coefficients

———— simple air-gap calculation

* * * * * measurement

4.3 Calculation of Normal Force by the Use of Flux Plot

The use of the three dimensional flux plot obtained in chapter 2 to calculate the normal force for homopolar linear synchronous machines is based on the engineering approximation[4.5] in which the non-linear relation between the excitation and the resultant flux was assumed to be linearised in a small neighbourhood of the operating point. In reference 4.5 , the linearisation was accomplished by using the assumption that the reluctivity in each mesh calculated for a particular operating condition remained constant in a small region around the operating point and the total flux was found by adding the flux linkages of each turn. However, for certain currents applied to field, armature, or both windings, a similar procedure is considered to determine the total of normal force F_n by the summation of forces f_n acting on each mesh of the rotor surface as shown in figures 4.3.1 and 4.3.2. It should be noted that the rotor surface under consideration is assumed to be that surface which is lying against the stator face.

One of the normal forces f_n can be written by reducing equation 4.2.1.1 to be for a single circuit

$$f_n = \frac{1}{2} I^2 \frac{L}{g} \qquad 4.3.1$$

Assuming that the flux density remains constant over the gap length g allows the inductance to be defined in a simplified manner as

$$L = \frac{N\phi}{I} \qquad 4.3.2$$

By solving the equations 4.3.1 and 4.3.2, the normal force f_n can be found in terms of the flux

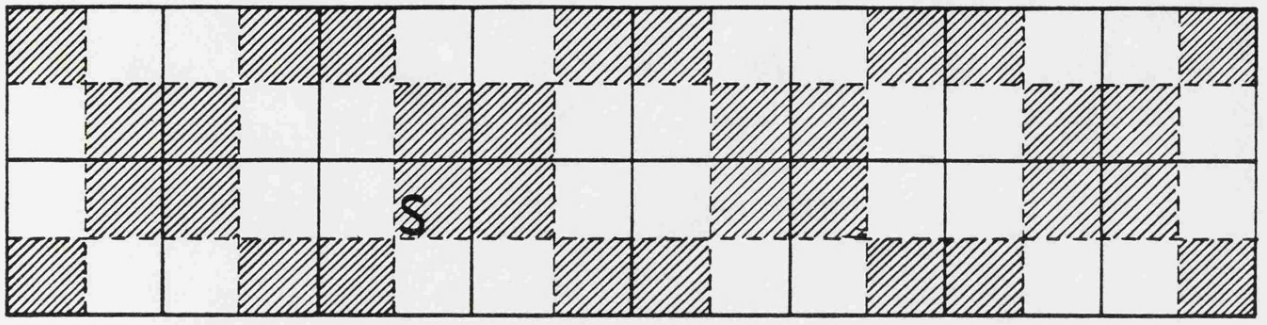

Fig 4·3·1 : The mesh over rotor surface .

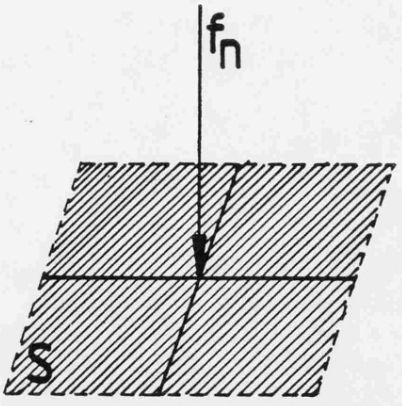

Fig 4·3·2 : Normal force f_n acting on one mesh .

$$f_n = \frac{NI\phi}{2g}$$

Therefore, the total force F_N is

$$F_n = 2p \sum_{i=1}^{n} (f_n)_i = \frac{2p}{2g} \sum_{i=1}^{n} (NI\phi)_i \qquad 4.3.3$$

where

n : the number of meshes on the rotor surface

p : the number of pole pairs

NI : the mmf of the air-gap branches

ϕ : the flux through the branch which is produced by NI

By using the values of three-dimensional flux which were obtained in Chapter 2, equation 4.3.3 gives the normal force which acts between the stator and the rotor of the homopolar LSM for such cases as shown in the following figures (4.3.3, 4.3.4 and 4.3.5).

Equation 4.3.3 was used to calculate the normal force F_N when both the field and armature currents were applied for the following cases.

$\delta_i = 0^o$ $F_{NO} = 1800.6$ N

$\delta_i = 90^o$ $F_{N90} = 694.9$ N

$\delta_i = 180^o$ $F_{N180} = 36.2$ N

In order to save computer time an estimation of the forces for other torque angles was made using the following method. Equation 4.2.2.1 can be simplified to

$$F_{N\delta_i} = a + b \cos \delta_i + c \cos 2\delta_i \qquad 4.3.4$$

where a, b and c are constants and their values are found to be

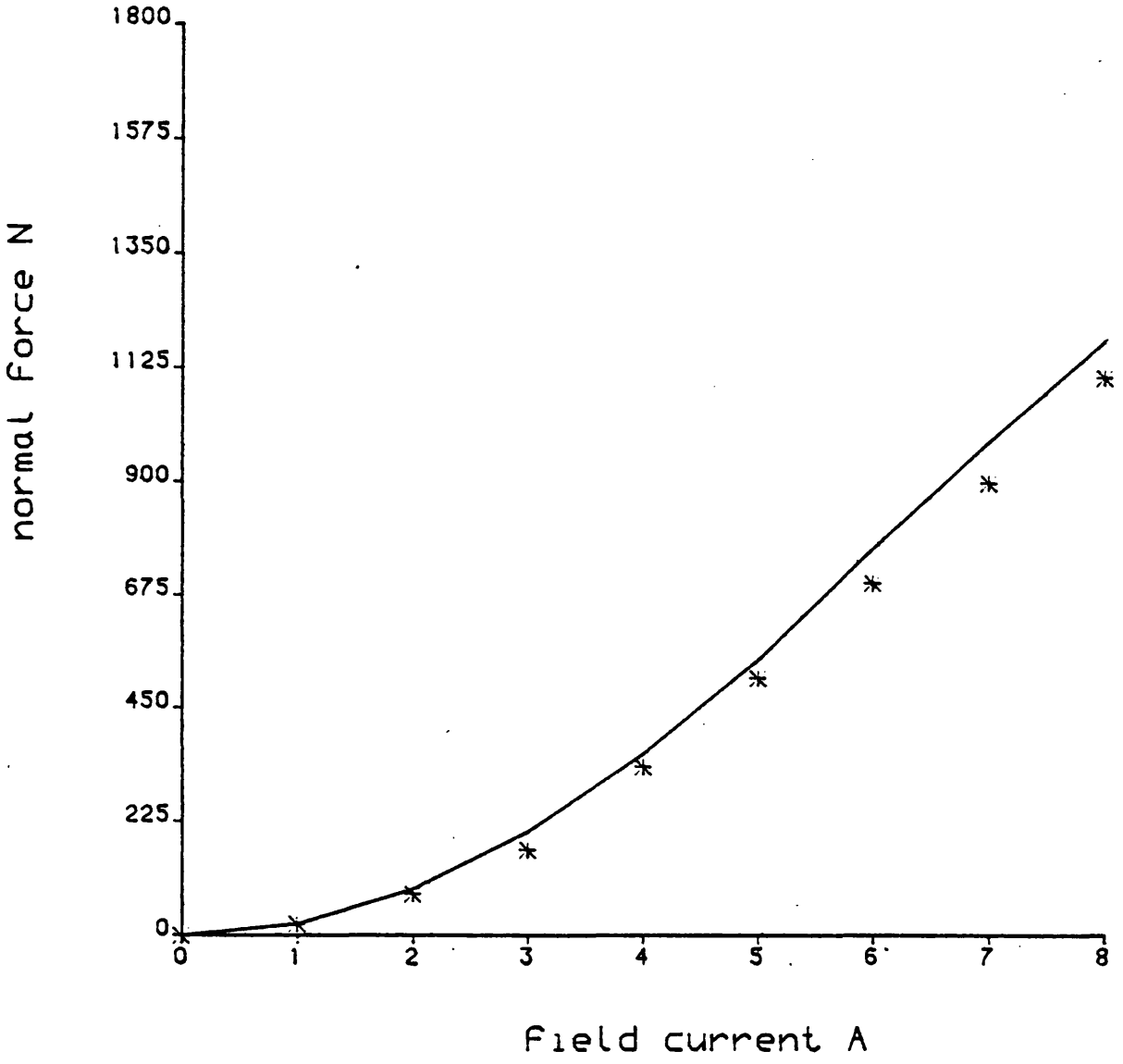

Fig. 4.3.3 Normal force due to field currents by the use of flux plots

———— computing

* * * * * measurement at 16.67 Hz

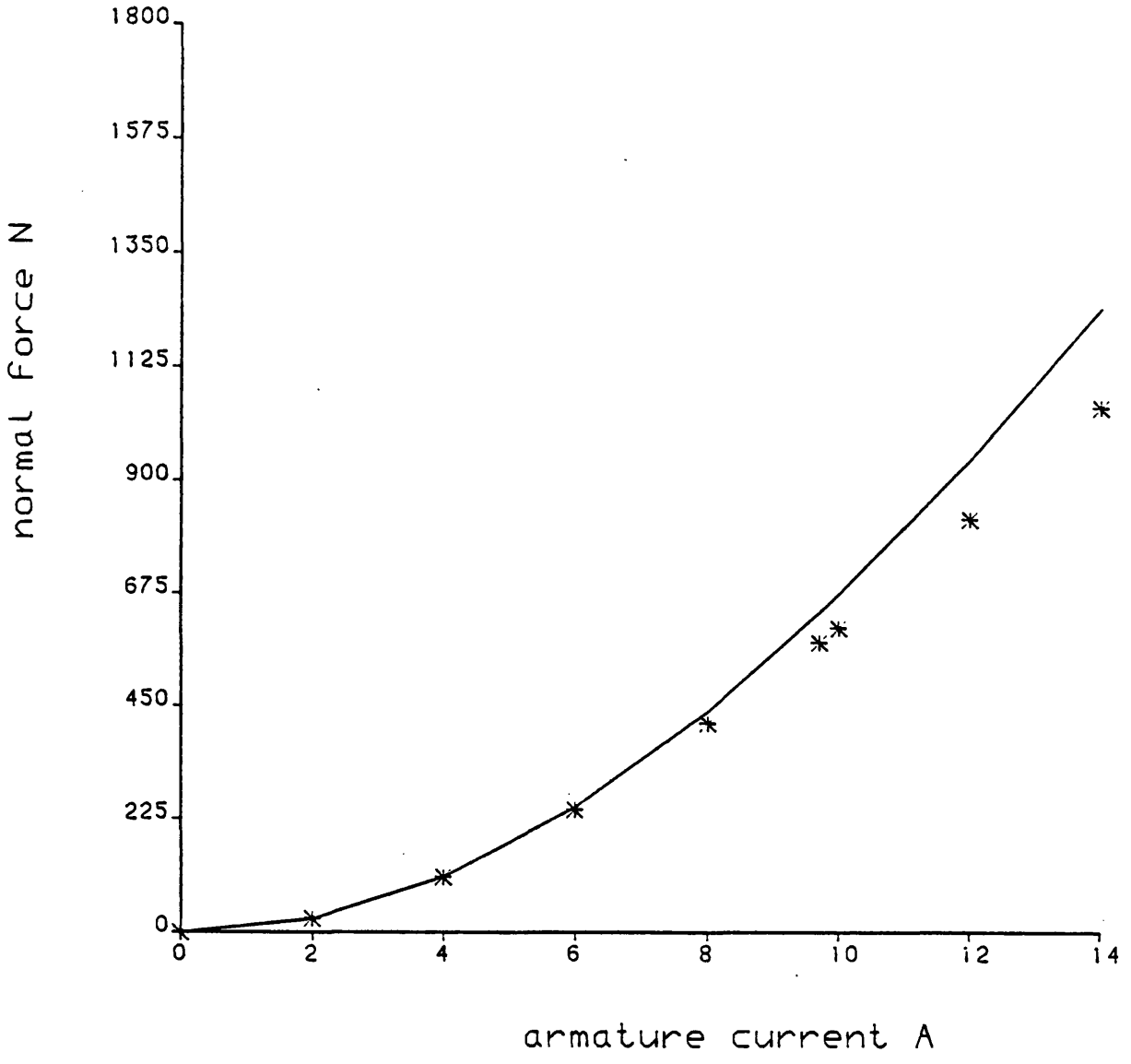

Fig. 4.3.4 D-axis normal force due to armature current by the use of flux plots

——————— computing

* * * * * measurement at 16.67 Hz

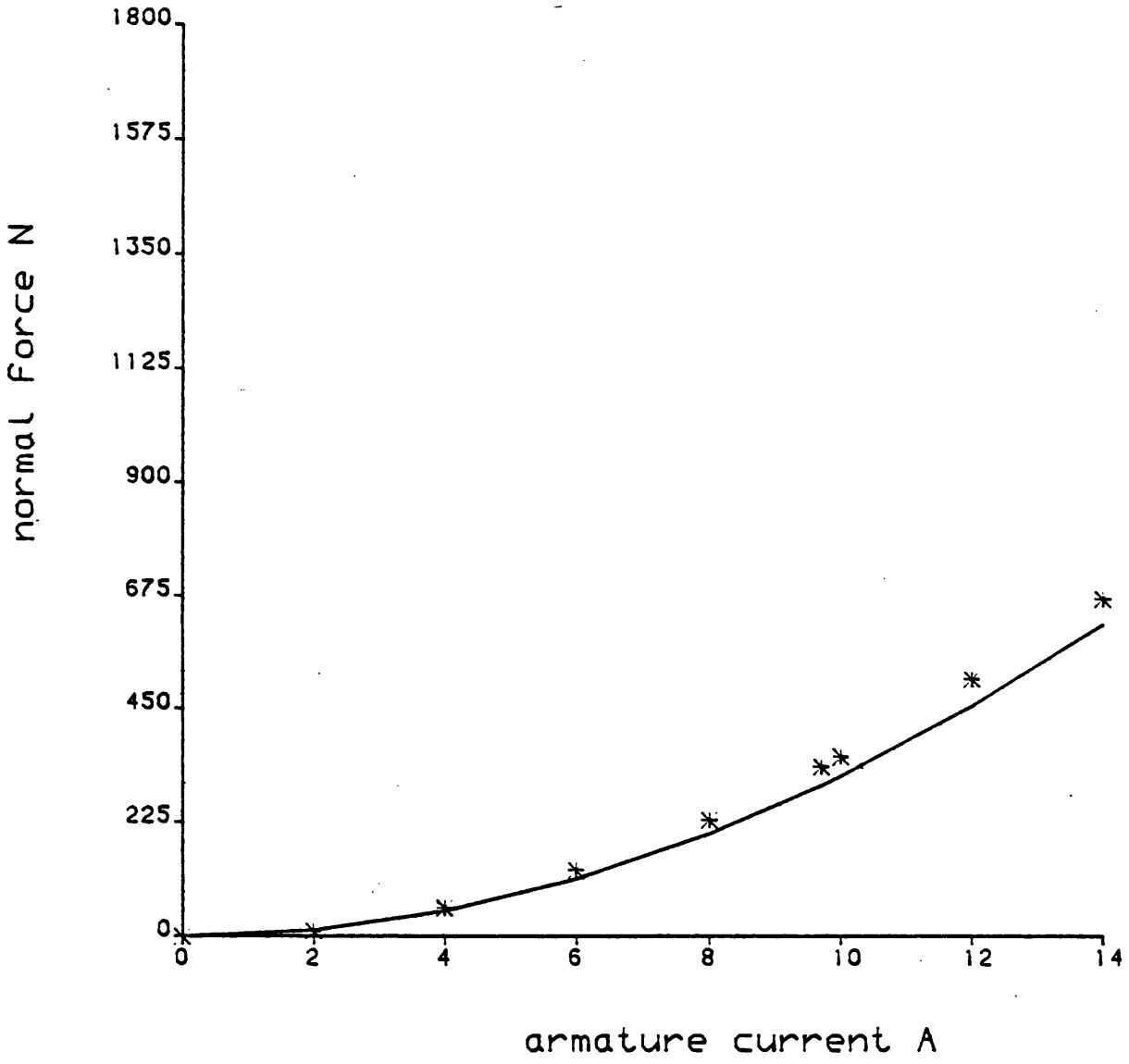

Fig. 4.3.5 Q-axis normal force due to armature current by the use of flux plots

——————— computing

* * * * * measurement at 16.67 Hz

$a = 806.6525$

$b = 882.185$ for $I_f = 5$ amps and $I_a = 9.7$ amps

$c = 111.7725$

Substituting these values in equation 4.3.4 gives

$$F_{N\delta_i} = 806.6525 + 882.185 \cos \delta_i + 111.7725 \cos 2\delta_i$$

By changing the torque angle from -180^o to $+180^o$, the corresponding normal forces can be obtained and these are shown in figure 4.3.6.

4.4 Maxwell's Stress for Mechanical Force Calculation

4.4.1 Introduction

In reference 4.3 it is shown how mechanical forces can be calculated by using the concept of Maxwell stress. The method is general and takes saturation into account since force is calculated directly from a field distribution. Carpenter[4.3] has solved a saturated problem by integrating over the surface near the saturated iron by following a zig zag path along the field equipotential and flux lines. He has also solved problems by integrating scalar potential over a surface[4.4].

In this section, the three dimensional flux distribution of the homopolar LSM which was obtained in chapter 2 is used for force predictions using the Maxwell Stress Method.

4.4.2 The basic equations

According to reference 4.6, there are two Maxwell's equations giving the stresses at a point in space. The first is a tensile stress along the line of force at each point which equals BH N/m^2. The second is a compressive stress in every direction at each point which equals

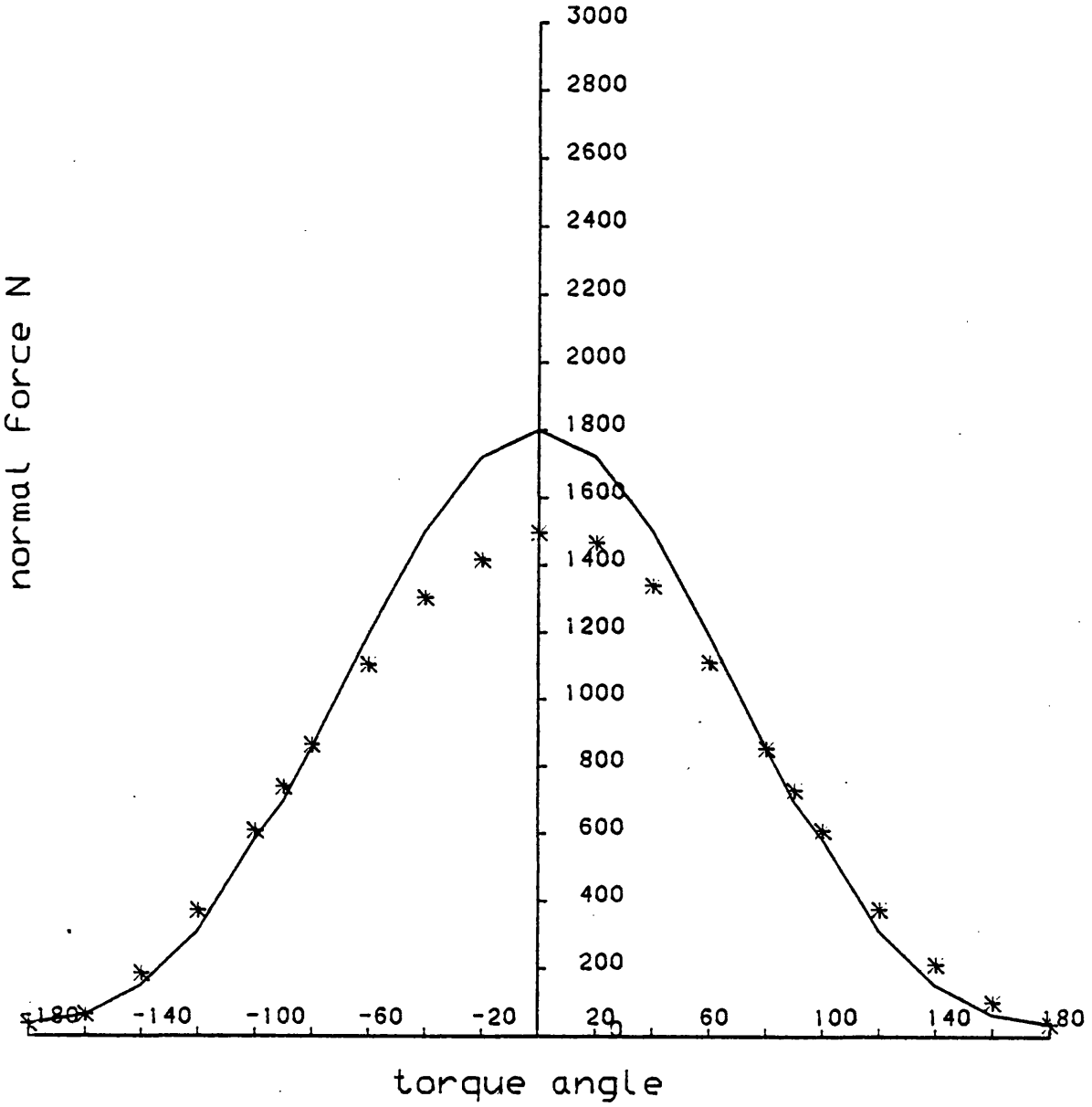

Fig. 4.3.6 Normal force of homopolar LSM due to field current of 5 amps and armature current of 9.7 amps by the use of flux plots

———— computing

* * * * * measurement at 16.67 Hz

$\mu_o H^2/2$ N/m^2. These equations are[4.4]

$$f_n = \frac{1}{2\mu_o} (B_n^2 - B_t^2)\ \delta s \qquad 4.4.2.1$$

$$f_t = \frac{1}{\mu_o} B_n B_t\ \delta s \qquad 4.4.2.2$$

Equation 4.4.2.1 gives the normal force component f_n directed positively outwards when used to find the force on what is inside the surface as distinct from the equal but opposite result on what is outside it.

Equation 4.4.2.2 gives the tangential force component f_t in the direction B_t when B_n is positive.

The only restrictions on the surface surrounding the body are that it must be closed and it must not pass through any iron. This means the permeability must be unity every where on the surface. It may also be noted that a surface is closed at infinity because the flux density is zero from the view point of Maxwell's stress.

4.4.3 Calculation of normal force

In three dimensions the surface for the application of Maxwell's stress for the homopolar LSM is shown in Fig. 4.4.3.1a. The surface is chosen to lie just outside the track pole and it extends to infinity in a direction X perpendicular on the paper as shown in Fig. 4.4.3.1b. The Maxwell's surface is also chosen to pass through mesh nodes[4.4] as shown in Fig.4.4.3.2. The use of this surface is very convenient for the calculation of the normal forces F_{nx}, F_{ny} and F_{nz} in the three directions x, y and z respectively.

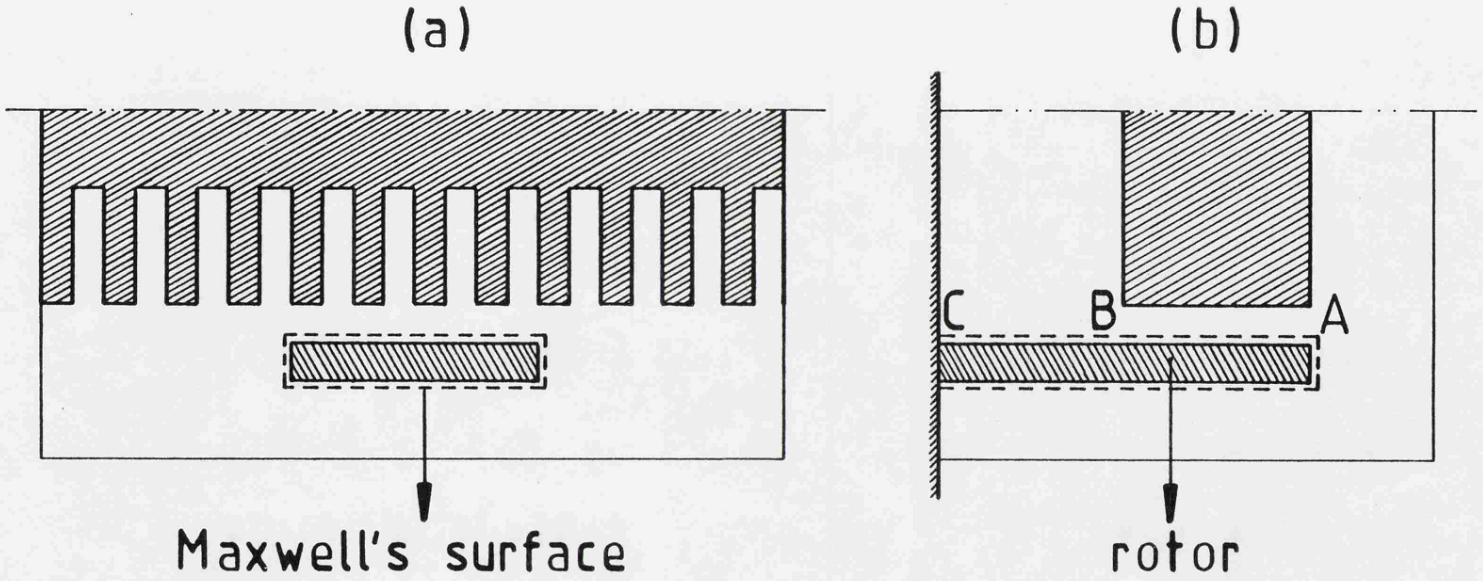

Fig 4·4·3·1 : Maxwell's surface surrounding the rotor of LSM .

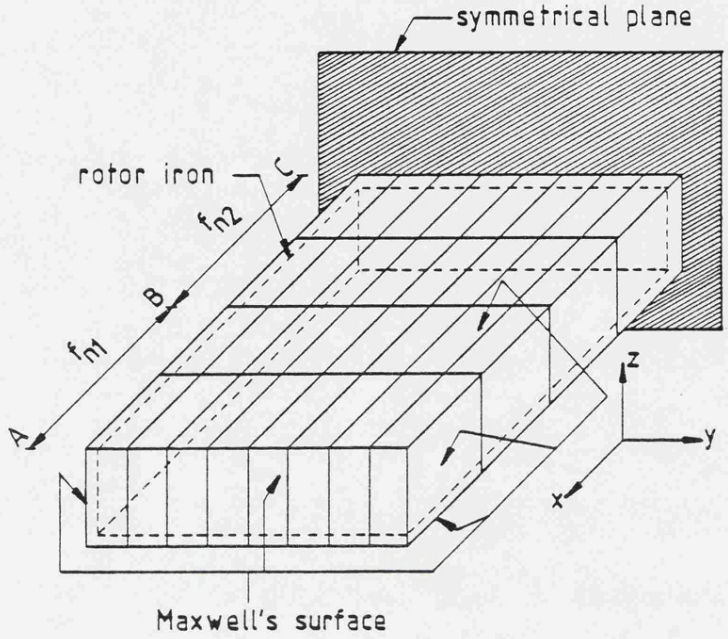

Fig 4·4·3·2 : 3-D Maxwell's surface surrounding rotor iron completely to form a closed surface .

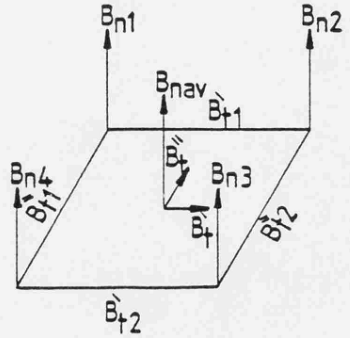

Fig 4·4·3·3 : Normal and tangential components of flux density (one mesh)

The average values of normal and tangential components, which are used in equation 4.4.2.1, are located at the centre point of a mesh as illustrated in Fig.4.4.3.3. The expressions for the average force values are

$$B_{nav} = \frac{B_{n1} + B_{n2} + B_{n3} + B_{n4}}{4}$$

$$B_{tav} = \sqrt{B'^{2}_{tav} + B''^{2}_{tav}}$$

where

$$B'_{tav} = \frac{B'_{t1} + B'_{t2}}{2}$$

$$B''_{tav} = \frac{B''_{t1} + B''_{t2}}{2}$$

The primes and double primes in the above expressions indicate two directions at right angles, both tangential to the surface. Because the tangential flux B_{tav} will be small compared with the normal flux B_{nav}, a good approximation can be obtained by neglecting B^{2}_{tav} in the equation 4.4.2.1. This is now reduced to

$$f_n = \frac{B^{2}_{nav}}{2\mu_o} \delta S \qquad 4.4.3.1$$

The difficulty associated with the use of average values of normal components of flux densities is that there is a big difference in values of flux densities between parts "AB" and "BC" on the surface shown in Fig.4.4.3.1 . This difference is shown in a two-dimensional view in Fig.4.4.3.4

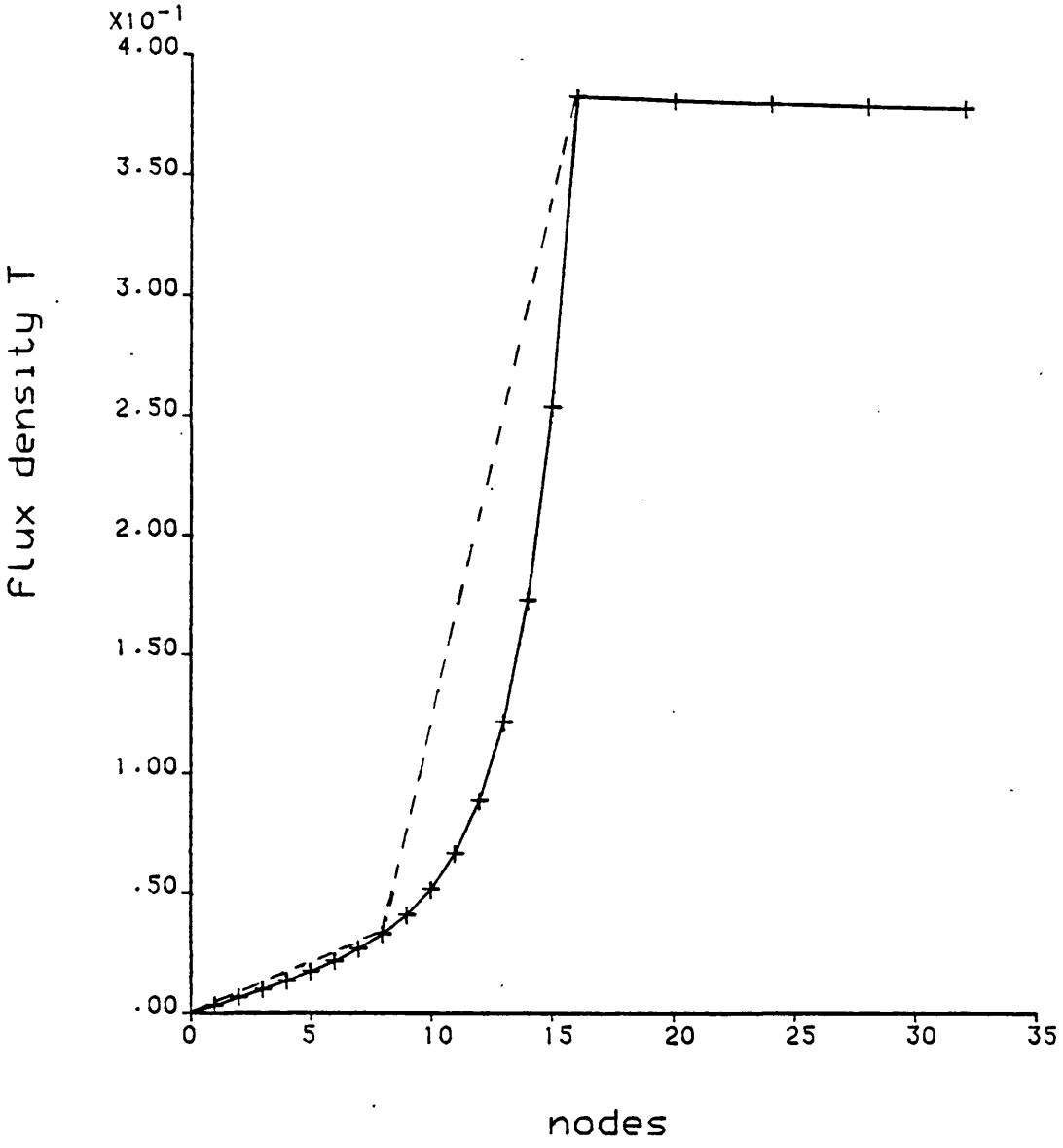

Fig. 4.4.3.4

——— Distribution after increasing the number of branches

- - - - " before " " " " "

To avoid generating a large amount of data necessary for a finer mesh in 3D, a 2-dimensional programme (NEW82E) was used to calculate a correction factor (f_c) for the average value of flux density. The results from the coarse and fine meshes are shown in Fig.4.4.3.4.

The normal forces acting on the surface BC, before and after the increase in the number of branches was calculated, and the correction factor was found to be equal (0.56). The expression for normal force becomes:

$$f_n = f_{n1} + 0.56\, f_{n2} \qquad 4.4.3.2$$

where

f_{n1} = the normal force acts on the surface of part AB

f_{n2} = " " " " " " " " " " BC

By using both of the equations 4.4.3.1 and 4.4.3.2 and integrating over the complete surface (Fig.4.4.3.2) the following forces were calculated.

i) F_{ny}, the normal force in the direction y was found to be very small in the following cases:

1. field current only
2. armature current only in both D and Q axes
3. field and armature windings excited with rotor in D axis

The reason that the forces in the three cases just mentioned, are very small is that the forces acting on the vertical sides of the Maxwell surface (Fig.4.4.3.2), in the direction y, are almost equal and opposite each other because of the symmetry of the flux pattern. However, when the rotor is in the Q axis and when both field and armature are excited the flux pattern is not symmetrical. This gives a resultant F_{ny} force. Table 4.4.3.1 shows the values of calculated forces, F_{ny}, for the cases

Current	F_{ny} (Newton)
I_f = 5 amps	.07457
I_a = 9.7 amps d-axis	.394
I_a = 9.7 amps q-axis	2.02
I_f = 5 amps & I_a = 9.7 amps d-axis	2.966
I_f = 5 amps & I_a = 9.7 amps q-axis	25.48

Table 4.4.3.1

described above considering a field current of 5 amps and an armature current of 9.7 amps. It should be noted that a small thrust would be generated, without the field being excited, because of the effect of variable reluctance.

ii) F_{nz}, the normal force in the direction z, is the resultant of the two forces acting in opposition on the upper and lower faces of the Maxwell surface (Fig.4.4.3.2). By following the same procedure as was used to calculate F_{ny}, all the results of F_{nz}, for different cases of field and armature currents, were obtained. A comparison between the calculated F_{nz} and those measured at 16.67 Hz is shown in figures 4.4.3.5, 4.4.3.6, 4.4.3.7 and 4.4.3.8. In order to plot these curves, a similar approximation to that which was used in section 4.3 of this chapter was employed to establish the normal forces F_{nz} for different torque angles. Forces F_{nz0}, F_{nz90} and F_{nz180}, which were found using the Maxwell surface and the three dimensional flux density distributions. The constant values of a, b, and c in equation 4.3.4 were determined to be

$$a = 689.98,\ b = 677.48 \text{ and } c = 15.55$$

The normal force F_{nz} for different torque angles can be expressed in terms of this angle as

$$F_{n\delta_i} = 689.98 + 677.48 \cos \delta_i + 15.55 \cos 2\delta_i$$

This force is shown in Fig.4.4.3.8 and compared with measured results.

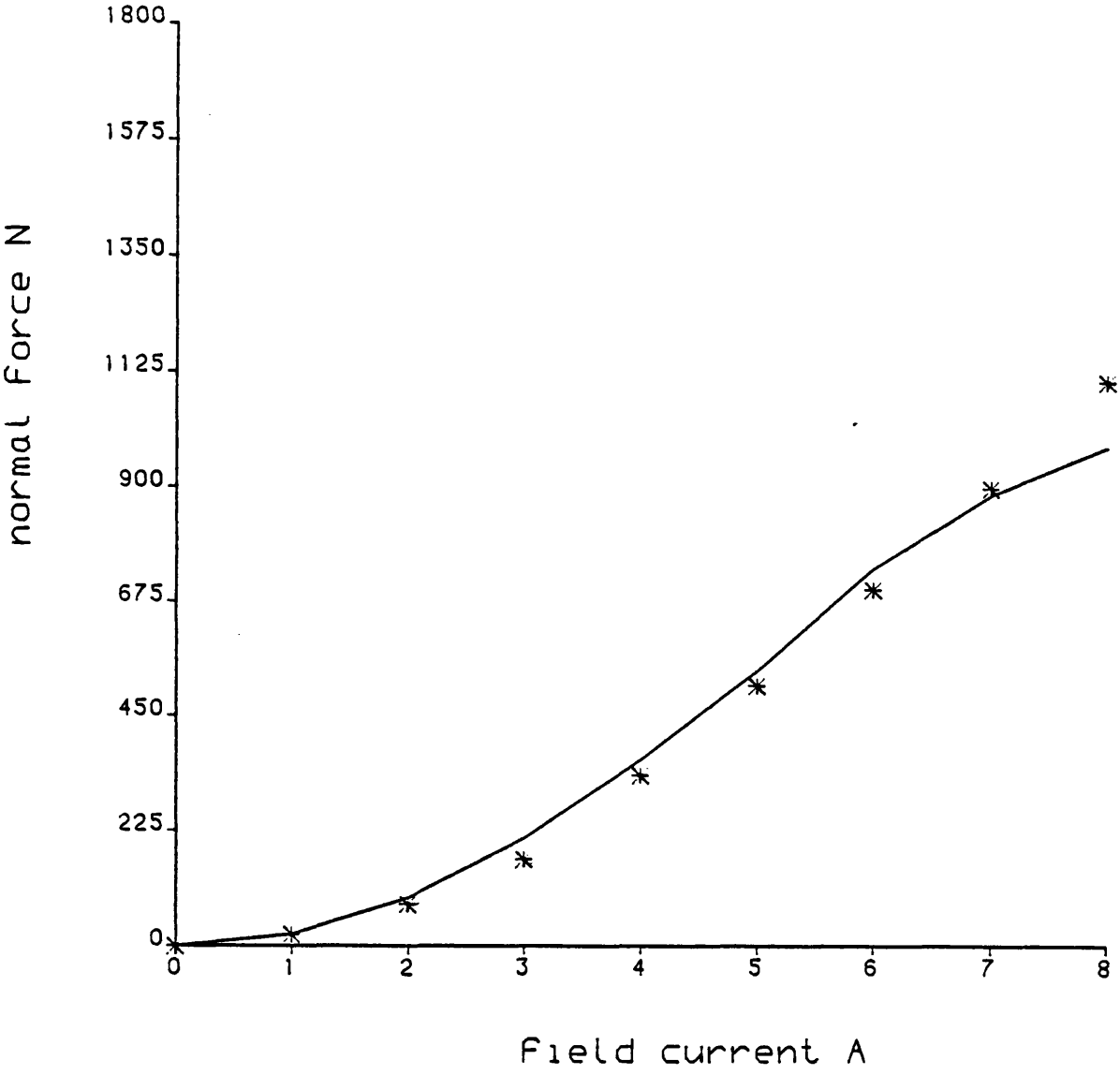

Fig. 4.4.3.5 Normal force due to field current by the use of Maxwell's stress

——— computing

* * * * measurement at 16.67 Hz

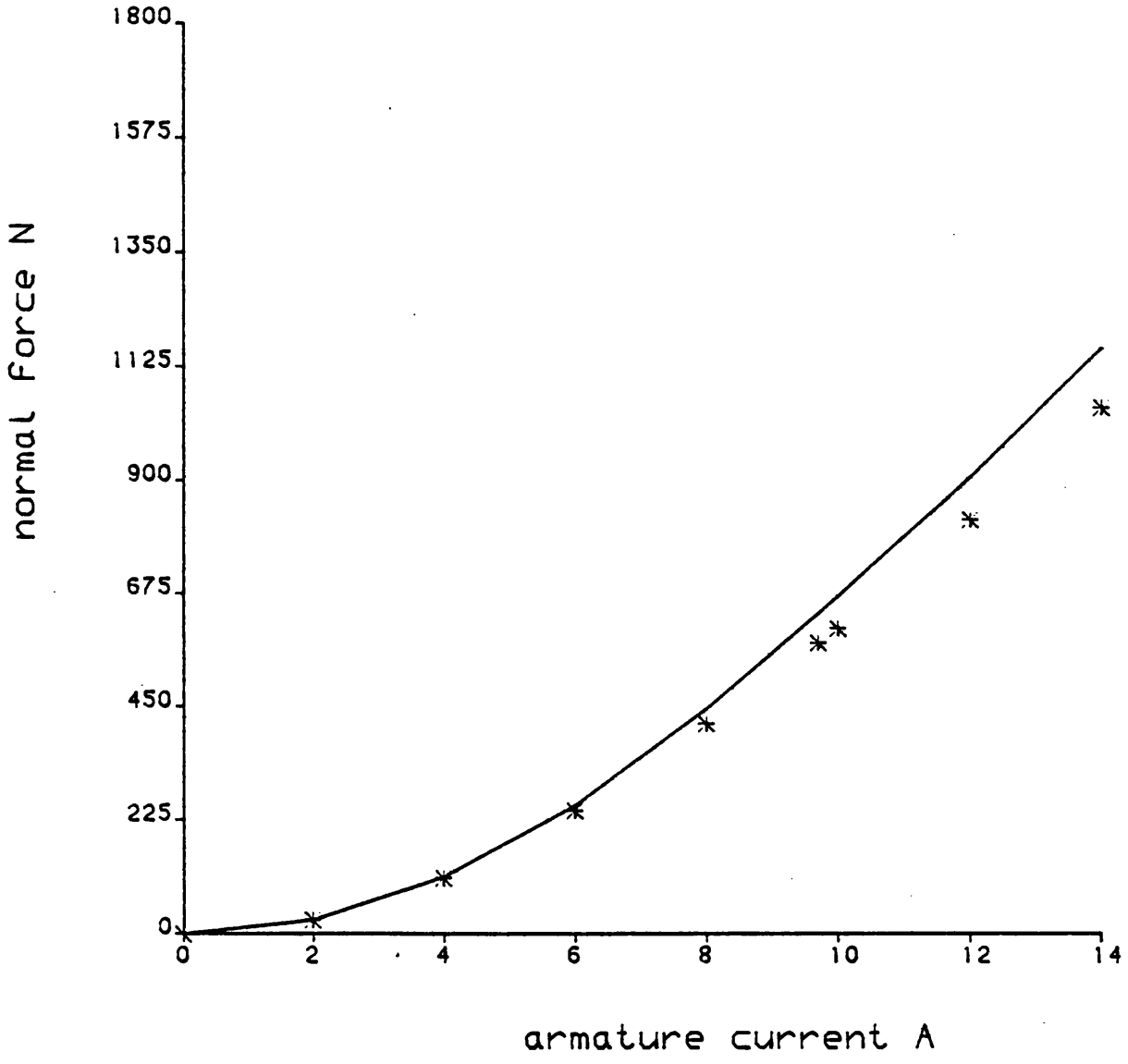

Fig. 4.4.3.6 D-axis normal force due to armature current by the use of Maxwell's stress

———— computing

* * * * * measurement at 16.67 Hz

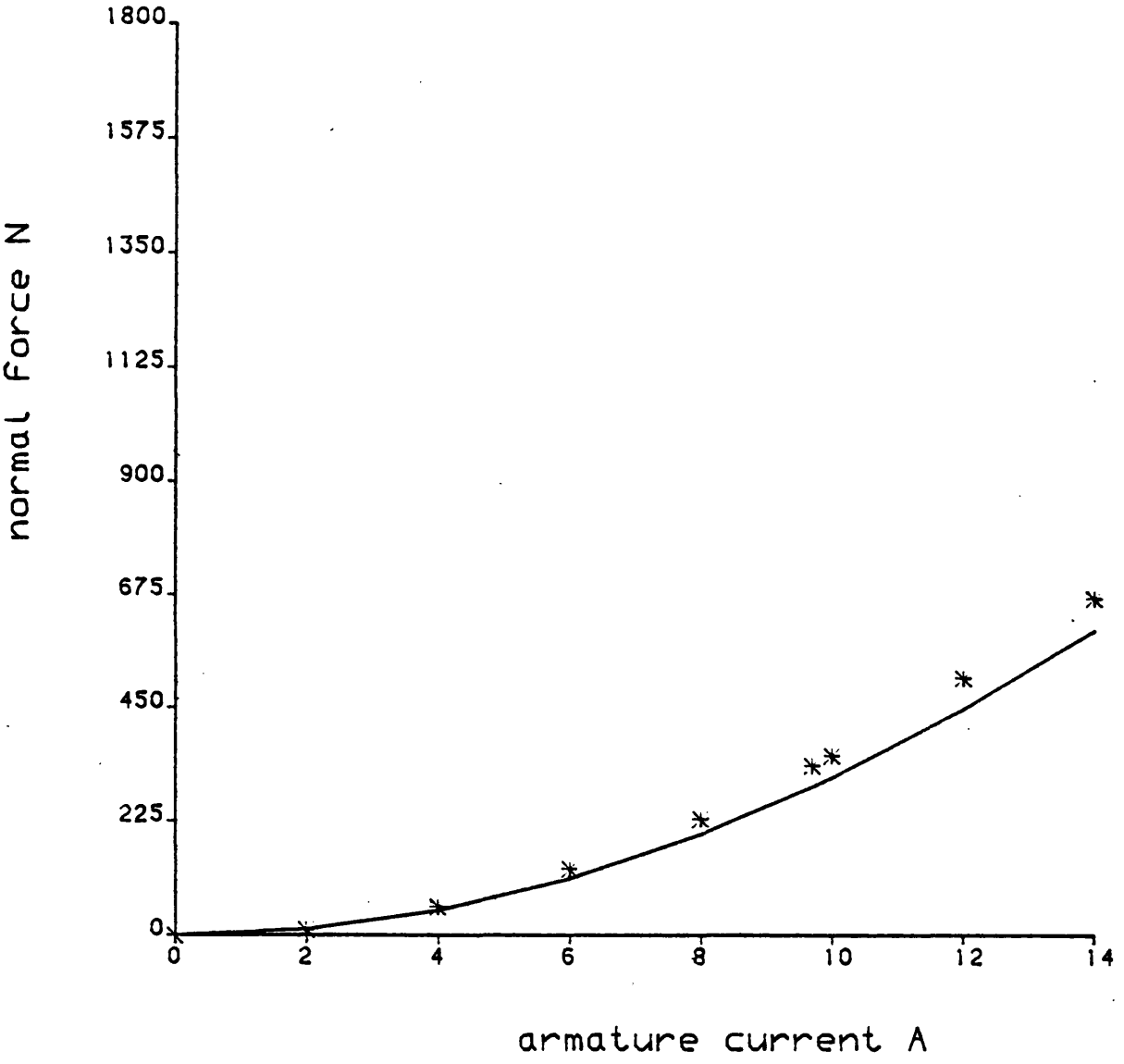

Fig. 4.4.3.7 Q-axis normal force due to armature current by the use of Maxwell's stress

——————— computing

* * * * * measurement at 16.67 Hz

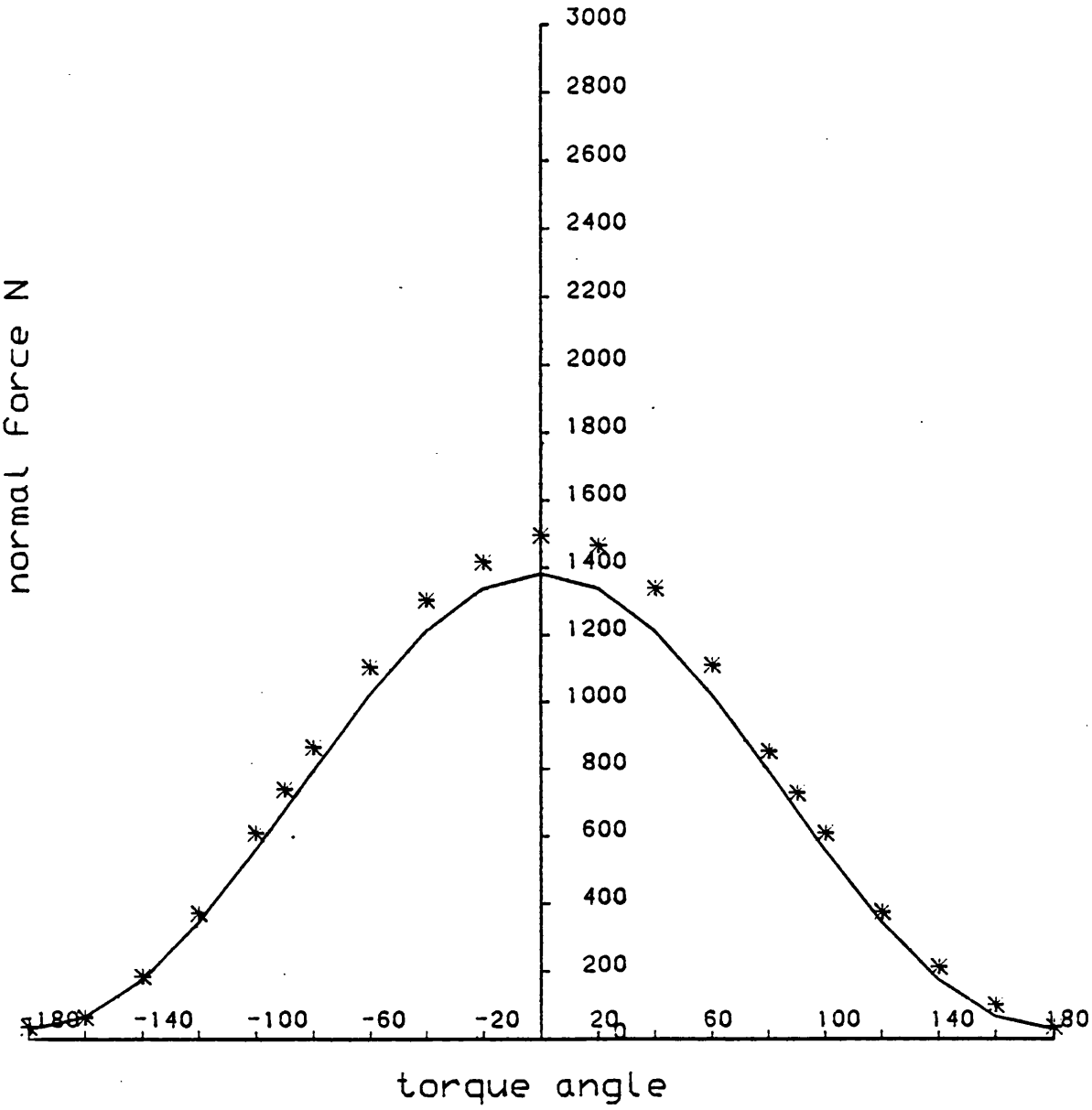

Fig. 4.4.3.8 Normal force of homopolar LSM due to field current of 5 amps and armature current of 9.7 amps by the use of Maxwell's stress

——————— computing

* * * * * measurement at 16.67 Hz

iii) F_{nx} the normal force in the direction x, is the resultant of two forces acting opposite each other on the front and back of the Maxwell surface (Fig.4.4.3.2). Because of the symmetry, these two forces are equal and they cancel each other to give zero force in the x-direction.

4.4.4 Calculation of Thrust Force

Two ways are available to calculate the thrust force on the rotor of the homopolar synchronous machine by using Maxwell's stress:

a) by calculation the resultant F_{ny} of normal forces which are acting on the right and left sides of the Maxwell surface (Fig.4.4.3.2).

b) by calculation the tangential forces which are acting on the top and bottom of the Maxwell surface (Fig.4.4.3.2).

The force F_{ny} was found in section (4.4.3) to be small compared with the predicted thrust given in section (4.2.3). In order to calculate the tangential force the tangential flux density is required. This is very small on the top surface of the rotor. In order to obtain a reliable value for the B_nB_t product the Maxwell surface was extended to touch the stator surface as shown in Fig.4.4.4.1. As in the previous section the average values of B_n and B_t were found and equation 4.4.2.2 was used to calculate the thrust force F_t as shown in table 4.4.4.1.

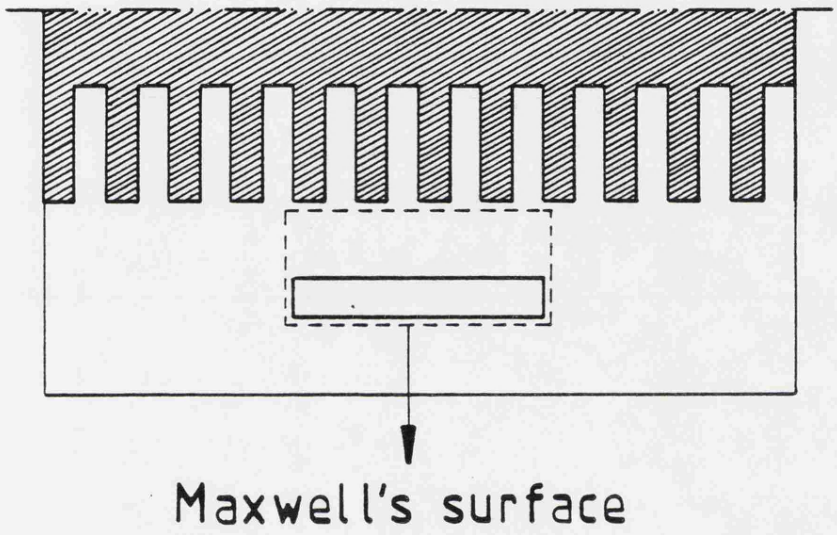

Fig 4·4·4·1 : Maxwell's surface to be extended for thrust force calculation .

Current	F_T (Newton)
I_f = 5 amps	.1127
I_a = 9.7 amps d-axis	.0755
I_a = 9.7 amps q-axis	.7184
I_f = 5 amps & I_a = 9.7 amps d-axis	7.184
I_f = 5 amps & I_a = 9.7 amps q-axis	113.88

Table 4.4.4.1

4.5 Discussion and Conclusions

Various methods have been described in this chapter for the calculation of normal force produced in a homopolar linear synchronous motor taking saturation effects into account. Maxwell's stress method seems to be the most accurate and easy to use.

Under saturated conditions the Maxwell stress method predicts forces somewhat less than the experimental values as shown in Fig. 4.4.3.5. for field currents of 7 amps and 8 amps, and in Fig. 4.4.3.8 for torque angle of 0^{o}. This is because the calculation was based on the square of the flux density.

The comparison between measurement and calculation shows the accuracy of prediction is acceptable for both inductance and flux linkage methods except for those values of saturation when both the field and armature currents are applied.

An examination of the machine force characteristics (Fig. 4.2.3.1 and Fig. 4.4.3.8) suggests that operation at a fixed torque angle of 90^{o} offers two main advantages. The first is that maximum motoring and braking force is available (Fig. 4.2.3.1). Secondly, there is a minimum of interaction between the lift force produced by the field current and the component due to the armature.

The normal force is dependent only upon the magnitude of the normal component of air-gap flux density. This flux component is an index of the magnetic iron loading and increases with the increasing armature voltage, decreasing frequency and speed, and decreasing air-gap length. Because of polar eddy currents the total flux will be reduced from the magnetostatic value. This has the effect of making the normal force speed dependent.

The tangential component of force F_{nx} perpendicular to the direction of motion arises only when stator is laterally displaced with respect to the track. Maxwell's method may be used to calculate this lateral force by considering the flux density distribution obtained for different displacements between the stator and rotor of the homopolar LSM.

The homopolar linear synchronous machine is capable of providing lift, guidance and propulsion simultaneously, but its end winding leakage for large pole pitches is very big. This machine provides also an alternative to the linear induction machine for application in modern ground transport. Both machines suffer from short stator effects which are due to the eddy currents induced in the iron of the track. These effects can be reduced by increasing the resistivity of the secondary by using laminations or by a suitable choice of material. The increase of complexity of the track structure may cause an increase in cost. However, there are many possibilities that have been discussed in reference 4.2 to improve the performance of linear synchronous machines.

References

4.1 Doherty, R.E. and Park, R.H.:
"Mechanical force between electric circuits", Trans.AIEE, 1926, 45, pp.240-252.

4.2 Balchin, M.J. and Eastham, J.F.:
"Characteristics of a heteropolar linear synchronous machine with passive secondary", IEE J. Electr. Power App. (GB), vol.2, No.6, pp.213-218 (Dec 1979).

4.3 Carpenter, C.J.:
"Surface-integral methdds of calculating forces on magnetised iron parts", Proc.IEE, 1960, 107C, pp.19-28.

4.4 Carpenter, C.J.:
"Numerical solution of magnetic fields in the vicinity of current-carrying conductors", Proc.IEE, 1967, vol.114, No.11, pp.1793-1800.

4.5 Fuchs, E.F. and Erdelyi, E.A.:
"Determination of waterwheel alternator steady-state reactances from flux plot", IEEE Summer Power Meeting, July 1971, pp.2510-2527, Paper no. TP596.

4.6 Carpenter, C.J.:
"Mechanical forces in AC fields", Imperial College of Science and Technology, Easter Course on Electromagnetics of Electrical Machines, 1972, Lecture 18.

CHAPTER FIVE

EXPERIMENTAL WORK

5.1 Introduction

In order to check the accuracy of the linear homopolar synchronous machine model, it is necessary to compare its predictions with measurements. The test results presented in this chapter are for the machine which was described in chapter 2.

A simple stationary model was used to check the levels of flux density predicted by the three-dimensional program TESTF. In this model the synchronised behaviour was simulated by feeding the windings of the machine with direct current[5.1].

Dynamic tests were conducted on both linear and cylindrical forms of homopolar synchronous machine. In the linear form the longitudinal edge effect produces loss and it also affects the distribution of air-gap flux-density. In order to eliminate the edge effect a cylindrical homopolar machine was used. This machine had exactly similar dimensions to those of the linear machine.

5.2 Description of Test Model

The apparatus built to perform the steady-state measurements is shown in (plate 1).* In this model the main components were a dc drive motor, an alternator and the two test machines. The shafts of the dc drive motor, the alternator and the cylindrical homopolar test machine were coupled together. The shaft of the alternator and that of the LSM drum were linked with a toothed belt. This ensured synchronous operation and the necessary speed reduction.

The stators of both round and linear machines were of "C-core" construction (see Fig. 1.5) and were constructed with laminations in order to reduce eddy currents. The laminations of the two side limbs lay in planes defined by the direction of motion and the normal to the secondary surface. The laminations of the top limbs lay in planes that are transverse to the direction of rotation and normal to the secondary. A non conducting stainless steel frame was used to support these laminations. A sufficient distance was left between the motors and the rest of the steel structure in order that the leakage flux paths were not disturbed.

Both stators of the test machines were identical in dimensions, construction and arrangement of windings, except for the number of turns on the armature winding. The cylindrical machine had 70 turns per coil whilst the linear version had 29 turns. Each coil spanned 2/3 of a pole. The slots of both machines were of the semi-closed type so as to minimise tooth ripple loss. The number of slots was 24 and each machine had 4 poles. In both machines the dc windings had 400 turns.

* The plate shows a heteropolar machine mounted in the test apparatus.

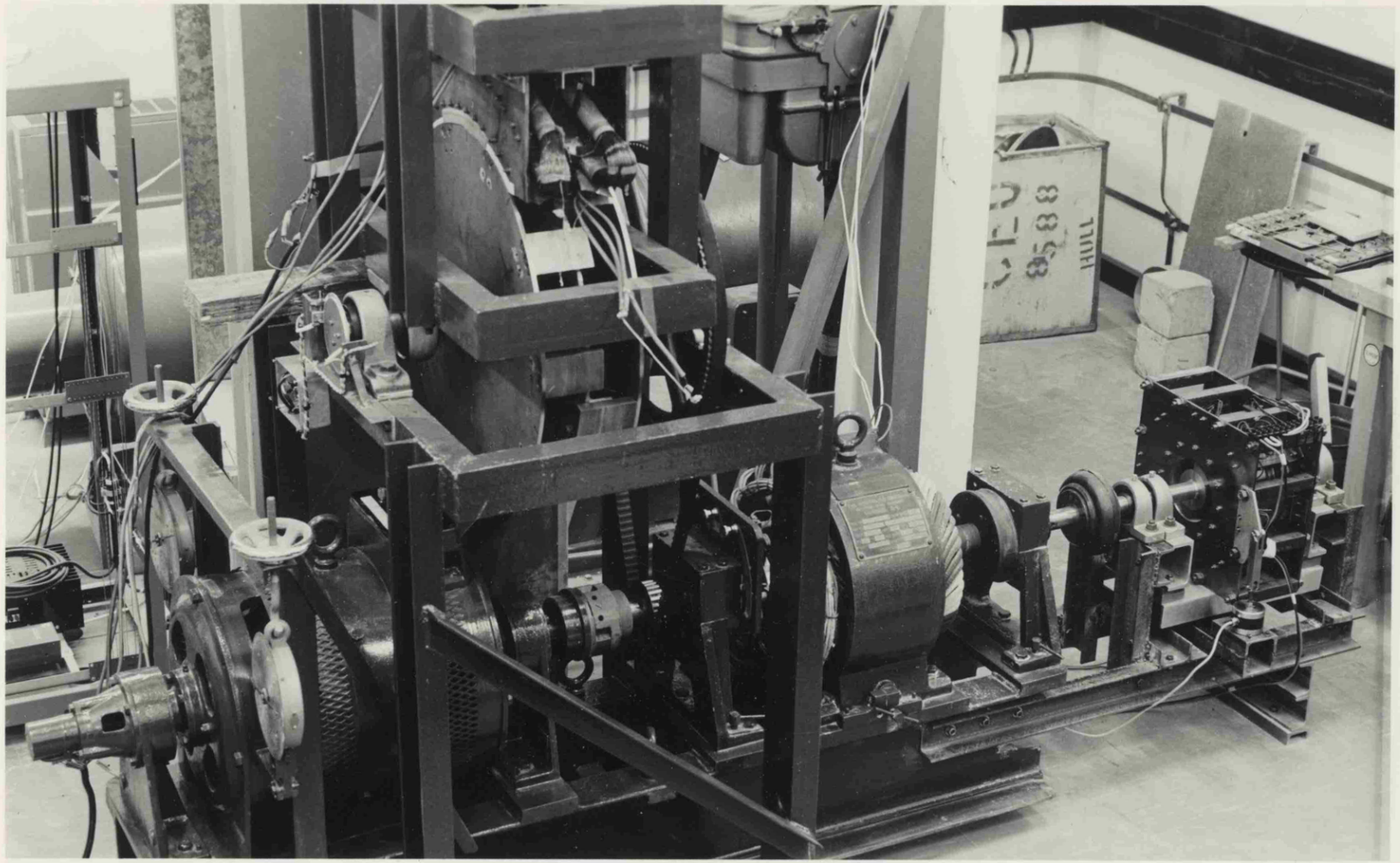

Plate 1 : General view of experimental apparatus

The secondaries of the test machines were made of solid mild steel. In the round version the mild steel blocks were secured to a non-conducting stainless steel shaft. In the linear version discs of stainless steel having low conductivity were constructed to support the secondary pole pieces. The linear test machine occupied approximately 70^{o} of the secondary. This was considered to leave sufficient distance for the flux to decay between the exit and entry edges of the machine.

In order to measure normal forces the stator of the linear machine was suspended within its support frame from four load cells (see plate 2)*. In order to obtain a closer estimate of the force produced by a truly linear machine a correction was applied to the measured value of force. This correction factor was obtained by considering a uniform radial force acting over the portion of the periphery occupied by the motor. It was found that the transducers underestimated the true normal force by some 6%.

The motor support frame (see plate 1) was free to rotate on the main shaft. Thrust force was measured by restraining the frame with a load cell.

Fig. 5.1 shows a general view of supply connections which were used in the test apparatus. A dc drive motor was fed from a 200 volt dc supply via a starter and variable resistors. These resistors were used to control the frequency by varying the drive motor speed. The field winding of the alternator was fed via its slip rings with a dc current which was obtained from 3-phase supply SU1 and rectifier RE1. Variac VA1 was used to control the magnitude of the alternator armature current which supplied the armature winding of the test machine. The dc current for the field winding of the test machine was provided from 3-phase supply SU2 and rectifier RE2, using variac VA2 to control its magnitude.

* The plate shows a heteropolar machine mounted in the test apparatus.

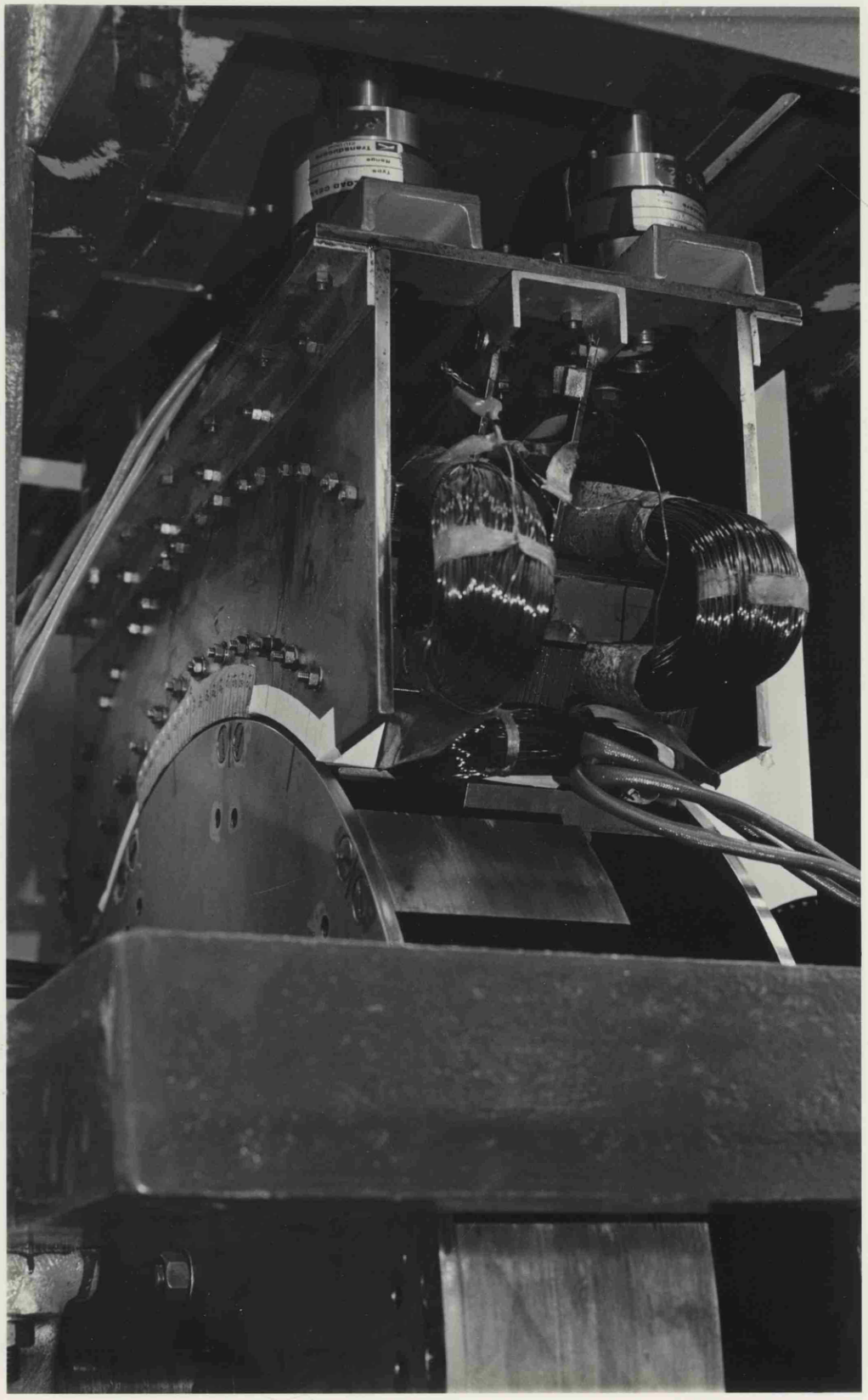

Plate 2 : Mounting of load cells
for measurement of normal force

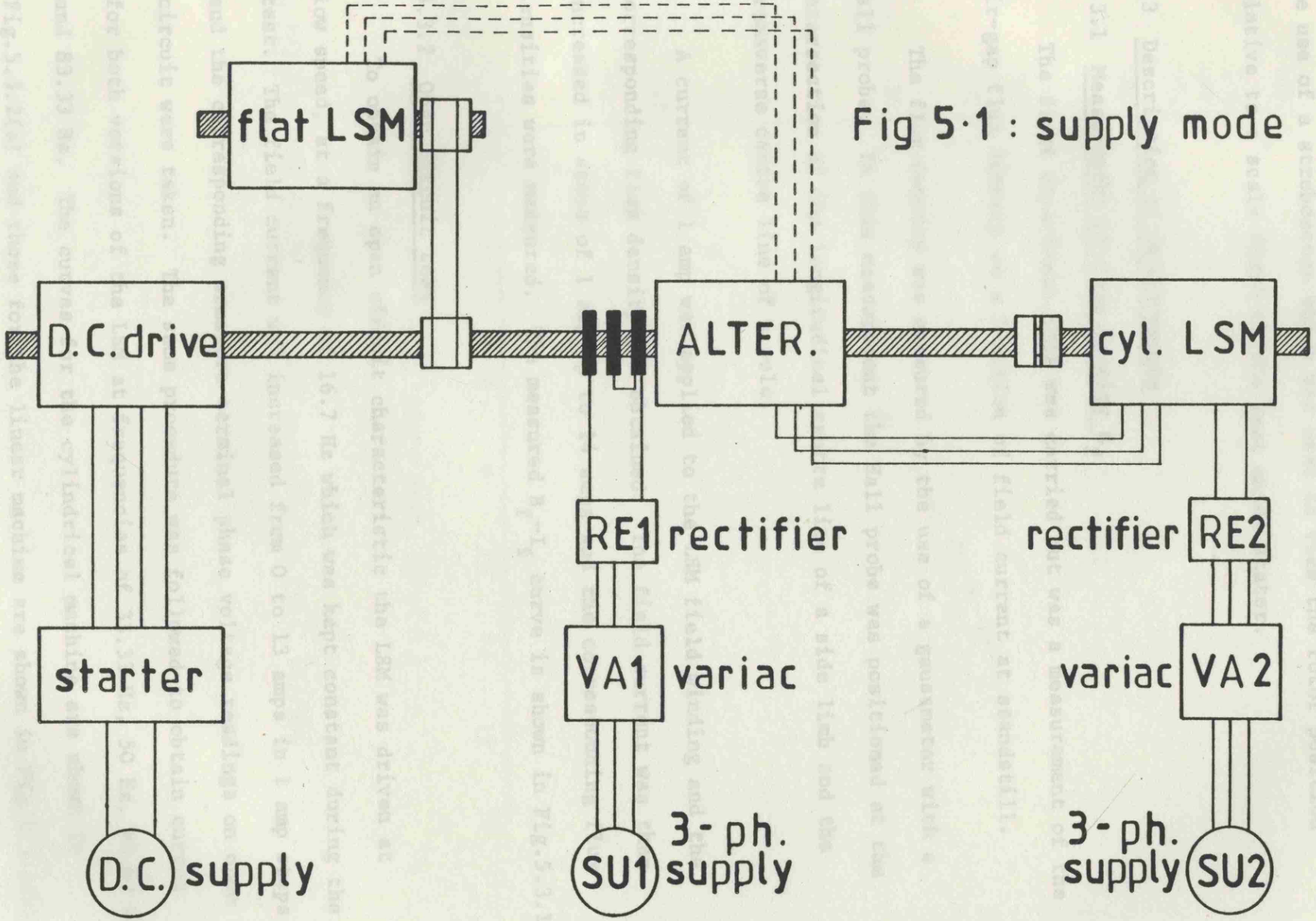

Fig 5·1 : supply mode

The coupling between the alternator and the test LSM was adjusted to obtain the desired torque angle. This torque angle was measured by the use of a stroboscope which was used to view the rotor position relative to a scale fixed to the test motor stator.

5.3 Description of Measurements

5.3.1 Measurement of flux density B_f

The first experiment that was carried out was a measurement of the air-gap flux density as a function of field current at standstill.

The flux density was measured by the use of a gaussmeter with a Hall probe. In this measurement the Hall probe was positioned at the intersection of the longitudinal centre line of a side limb and the transverse centre line of a pole.

A current of 1 amp was applied to the LSM field winding and the corresponding flux density was obtained. The field current was then increased in steps of 1 amp up to 14 amps and the corresponding flux densities were measured. The measured B_f-I_f curve is shown in Fig.5.3.1.

5.3.2 Open circuit test

To obtain an open circuit characteristic the LSM was driven at low speed, at a frequency of 16.7 Hz which was kept constant during the test. The field current was increased from 0 to 13 amps in 1 amp steps and the corresponding armature terminal phase voltage readings on open circuit were taken. The same procedure was followed to obtain curves for both versions of the LSM at frequencies of 33.33 Hz, 50 Hz, 66.67 Hz, and 83.33 Hz. The curves for the cylindrical machine are shown in Fig.5.3.2(a) and those for the linear machine are shown in Fig.5.3.2(b).

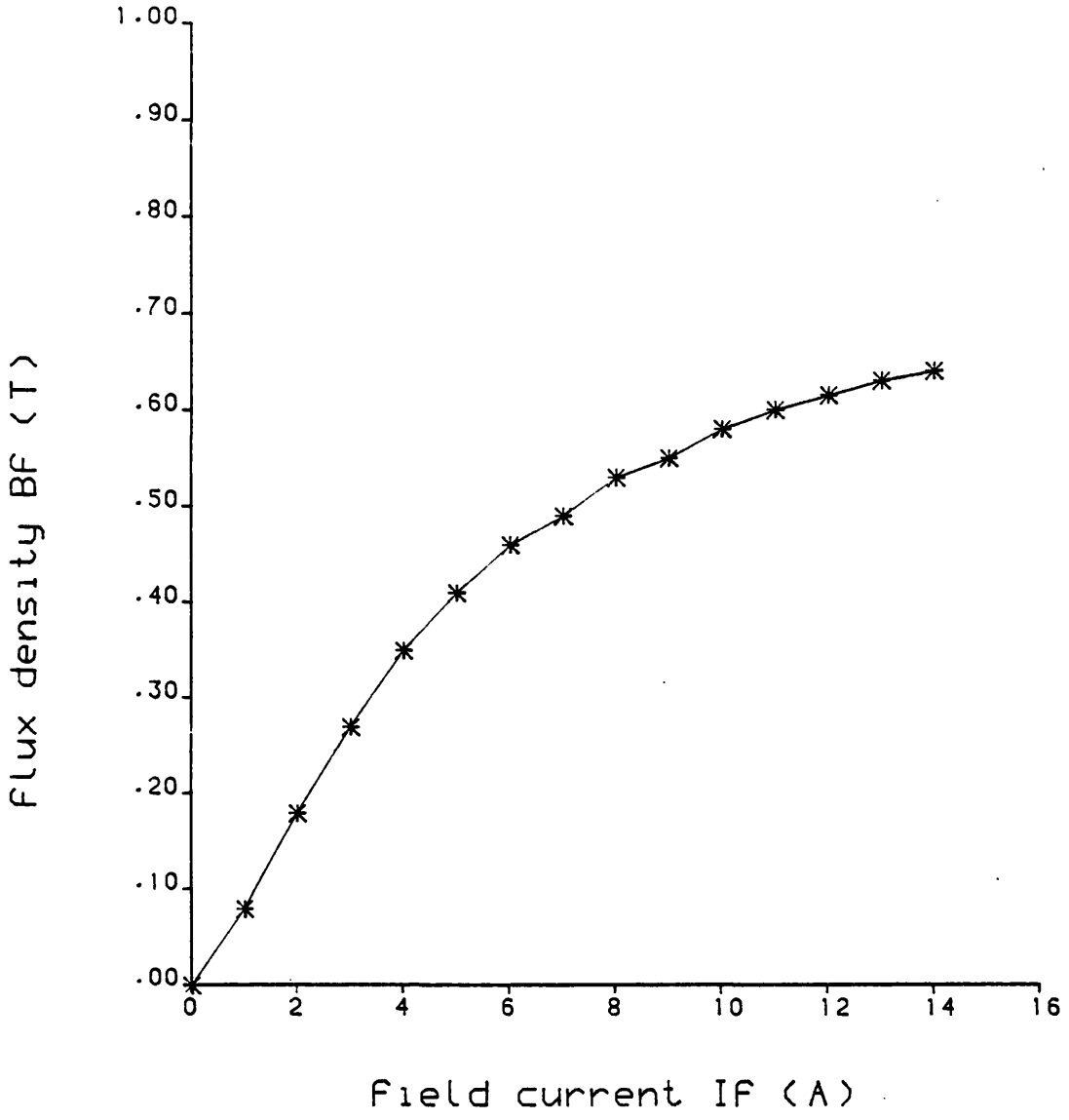

Fig. 5.3.1 Flux density at stand still due to field current

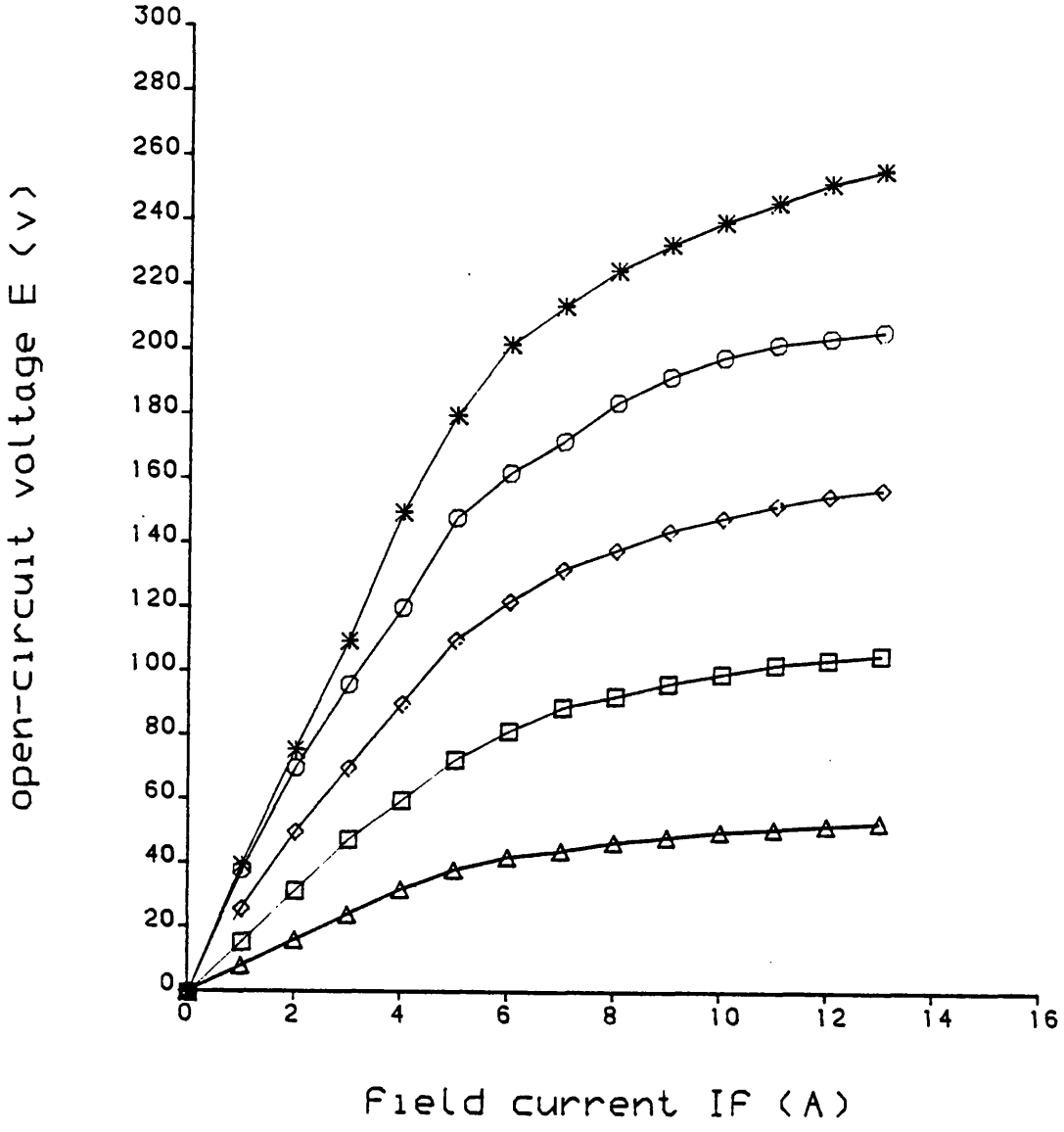

Fig. 5.3.2(a) Open-circuit test for cylindrical LSM at many frequencies

Δ–Δ–Δ–Δ–Δ measurement at 16.67 Hz

□–□–□–□–□ " " 33.33 Hz

◇–◇–◇–◇ " " 50 Hz

o–o–o–o–o " " 66.67 Hz

––*–*–* " " 83.33 Hz

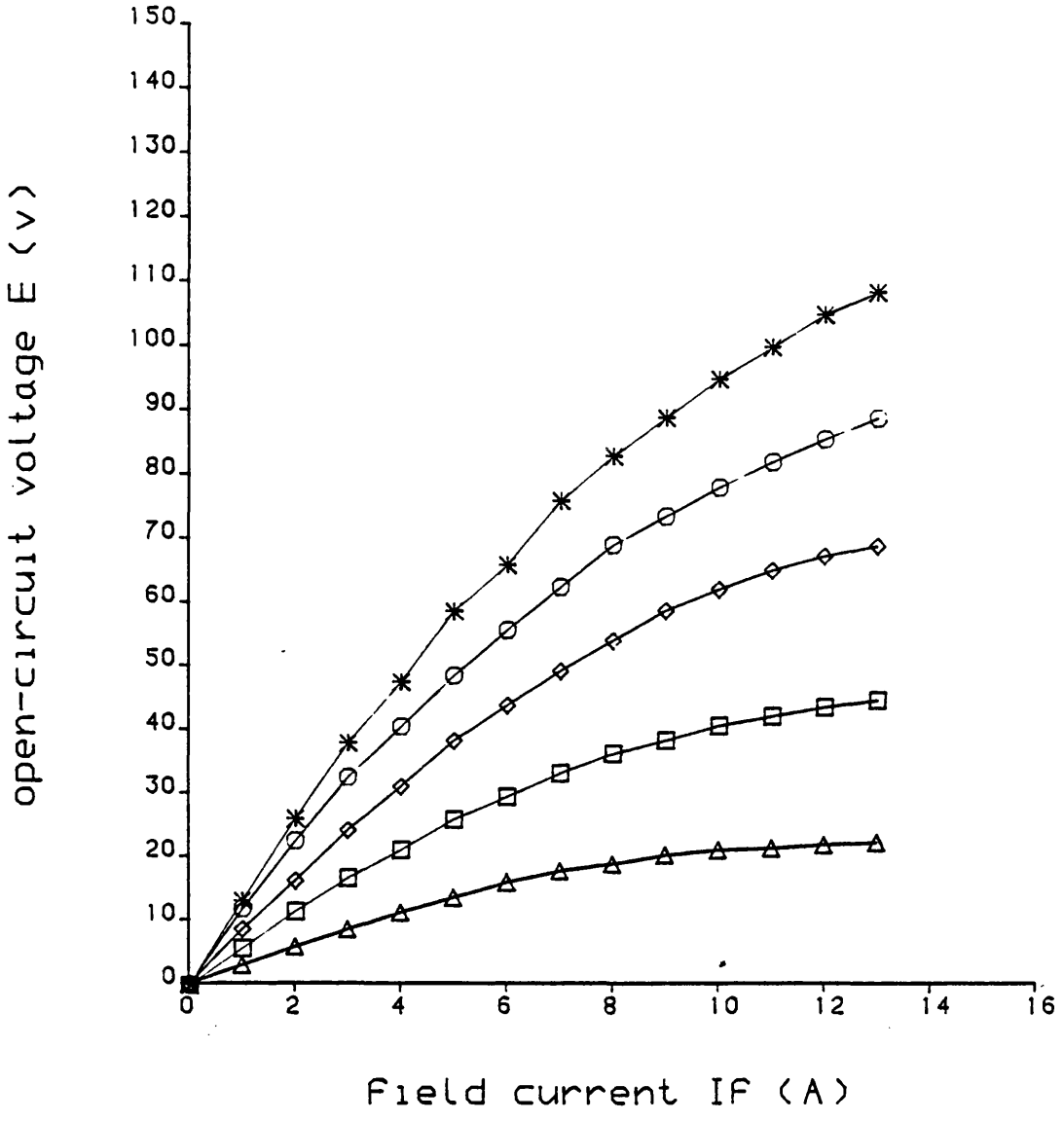

Fig. 5.3.2(b) Open-circuit test for flat LSM at many frequencies

△—△—△—△—△	measurement at	16.67 Hz
□—□—□—□—□	" "	33.33 Hz
◇—◇—◇—◇	" "	50 Hz
o—o—o—o—o	" "	66.67 Hz
——*—*—*	" "	83.33 Hz

5.3.3 Measurements of the d-axis and q-axis air-gap voltage

The two reaction theory considers direct and quadrature axes separately, assigning different reaction reactances to each. To separate the magnetizing reactance X_{md} or X_{mq} and the leakage reactance $X_{\ell d}$ or $X_{\ell q}$ a search coil was added to the test machines. This search coil was fitted to the pole face of the stator enabling an air gap voltage to be measured and a magnetizing inductance L_{md} or L_{mq} to be obtained by the use of equation $E/\omega = (L_{md}, L_{mq})I$. The cylindrical machine was used for these tests so that longitudinal edge effects could be avoided.

Firstly, the machine was driven at low speed at a frequency of 16.67 Hz with 1 amp positive sequence current applied to the armature winding. In order to offer a path of high permeance the rotor of the LSM was so rotated that a torque angle of 0^{o} was maintained. Readings of the air gap voltage were noted as the armature current was increased from 1 to 8 amps in 1 amp steps. This procedure was repeated for the same frequency steps used in the open circuit experiment mentioned in the previous section.

The same procedure was used for the q-axis measurements. All the readings just described were multiplied by 234 to obtain the equivalent phase voltage E according to the following relationship

$$E = E_g \frac{2p(Z_a\ q\ K_w)}{N_{se}}$$

where

$2p(Z_a\ q\ K_w)$ is known from Appendix 2.9.2 where Z_a for the cylindrical LSM is 140 turns

N_{se} the number of turns of the search coil (4)

E_g the reading of air gap voltage using the search coil

the sets of results for both d-axis and q-axis positions of the rotor are shown in Figures 5.3.3 and 5.3.4 respectively.

5.3.4 Normal force test

The first test carried out was the measurement of normal force as a function of field current. For this measurement the field current was increased from 0 to 8 amps in 1 amp steps without rotating the machine and the results are shown in Fig. 5.3.5.

The next step in the force measurements was to find the force characteristics due to armature current variations in both d and q axes. At first the machine was set, as in the previous test, to a low speed (16.67 Hz), with a constant torque angle of 0^{o}. The armature current was increased from 0 to 14 amps in 2 amp steps and force readings were taken at each step. These results are shown in Fig. 5.3.6.

The procedure just described was repeated for a fixed torque angle of 90^{o} in order to obtain the q-axis force. This is shown in Fig.5.3.7.

The measurement of the variation of attractive force with rotor position, and constant armature and field currents was also carried out and the results are shown in Fig. 5.3.8 and Fig. 5.3.9 respectively. For this measurement, the LSM was running at a low frequency (16.67 Hz) which was kept constant during the test. The force readings were taken for (I_f = 0, I_a = 0) amp, (I_f = 0, I_a = 9.7) amp and (I_f = 5, I_a = 9.7) amp.

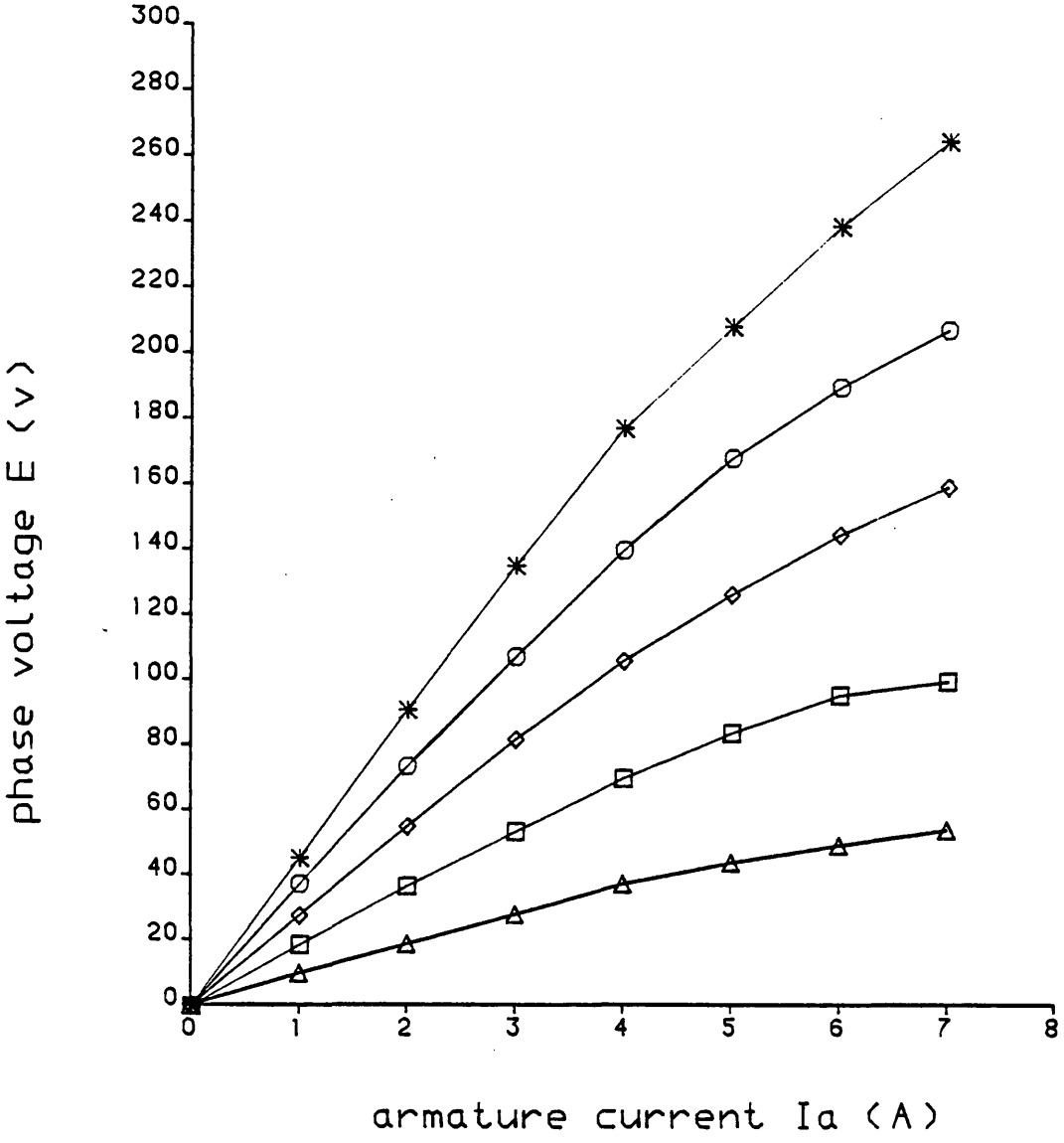

Fig. 5.3.3 D-axis phase voltage test for cylindrical LSM at many frequencies

Δ–Δ–Δ–Δ–Δ	measurement at	16.67 Hz
□–□–□–□–□	" "	33.33 Hz
◇–◇–◇–◇–◇	" "	50 Hz
o–o–o–o–o	" "	66.67 Hz
––*–*–*	" "	83.33 Hz

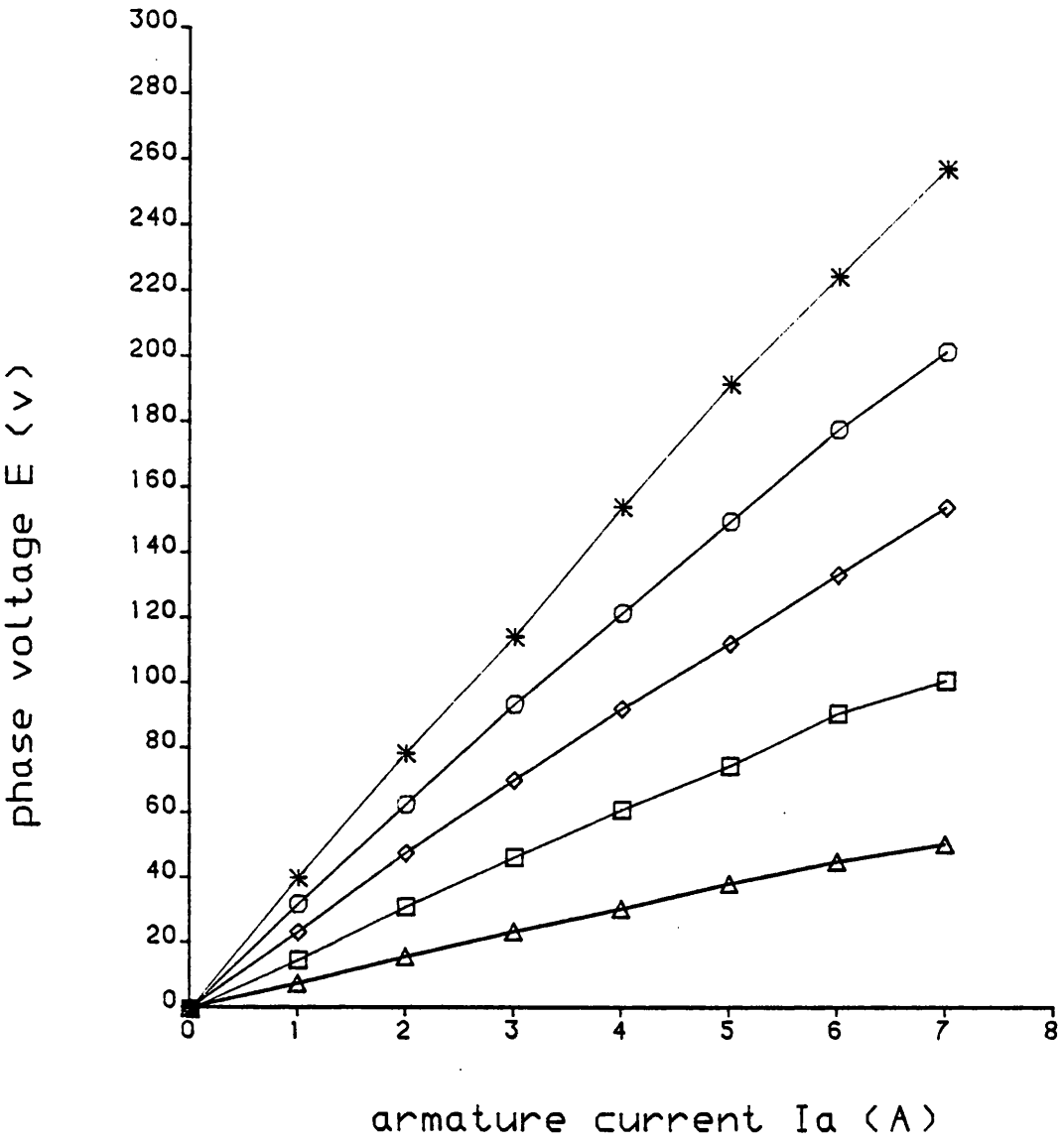

Fig. 5.3.4 Q-axis phase voltage test for cylindrical LSM at many frequencies

△—△—△—△—△ Measurement at 16.67 Hz

□—□—□—□—□ " " 33.33 Hz

◇—◇—◇—◇—◇ " " 50 Hz

○—○—○—○—○ " " 66.67 Hz

——*—*—* " " 83.33 Hz

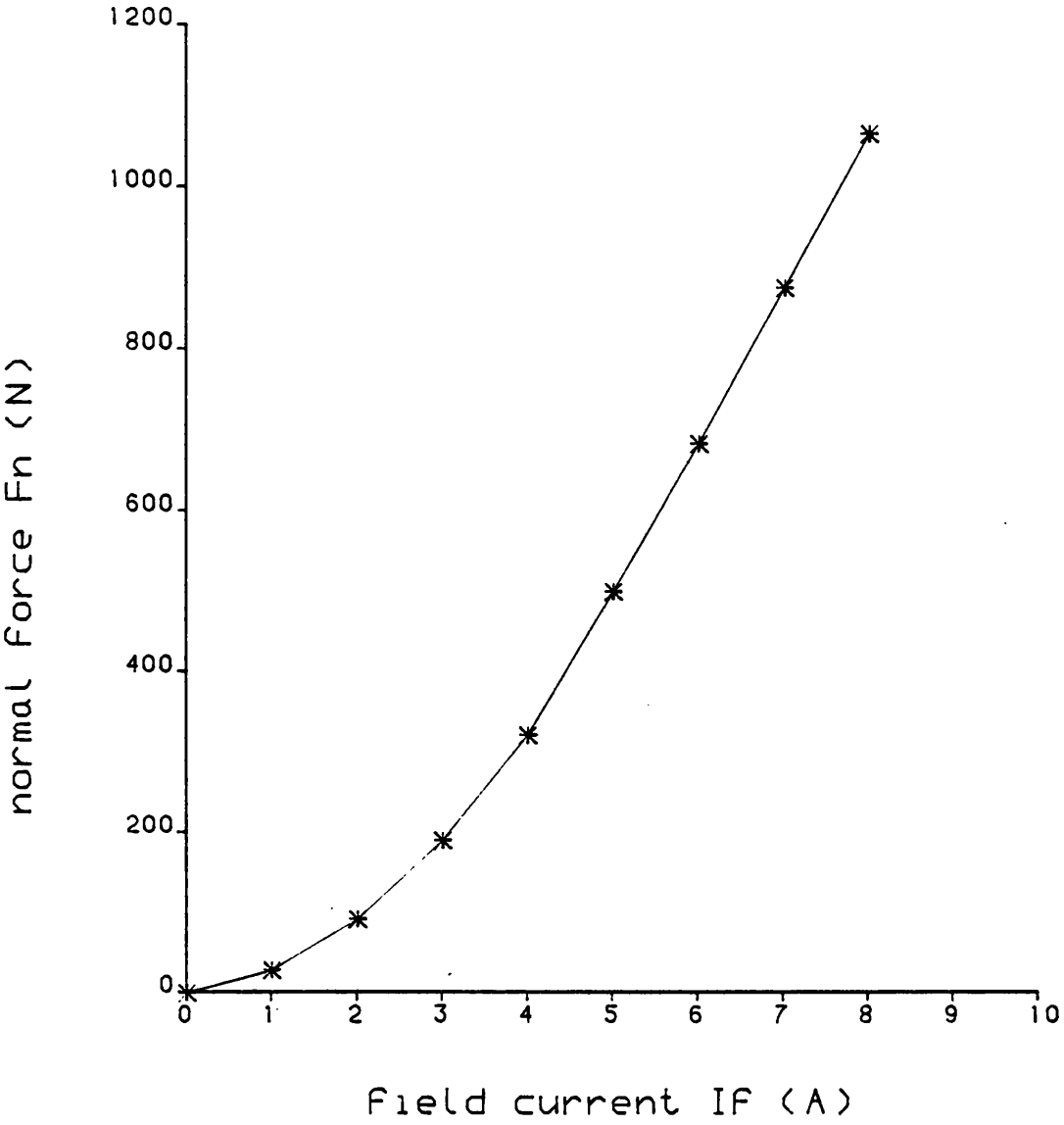

Fig. 5.3.5 Normal force due to field current measured at standstill

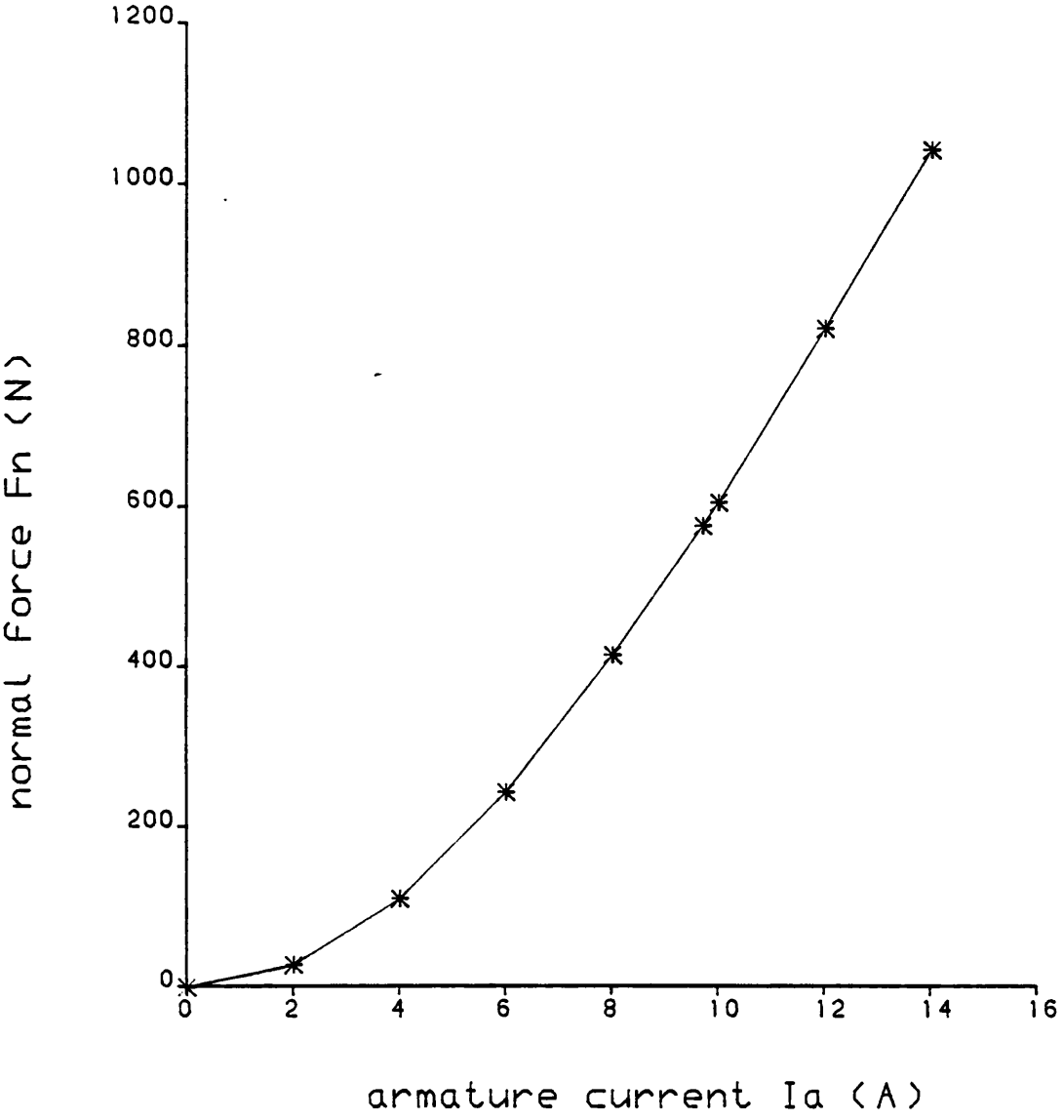

Fig. 5.3.6 D-axis: normal force due to armature current measured at 16.67 Hz

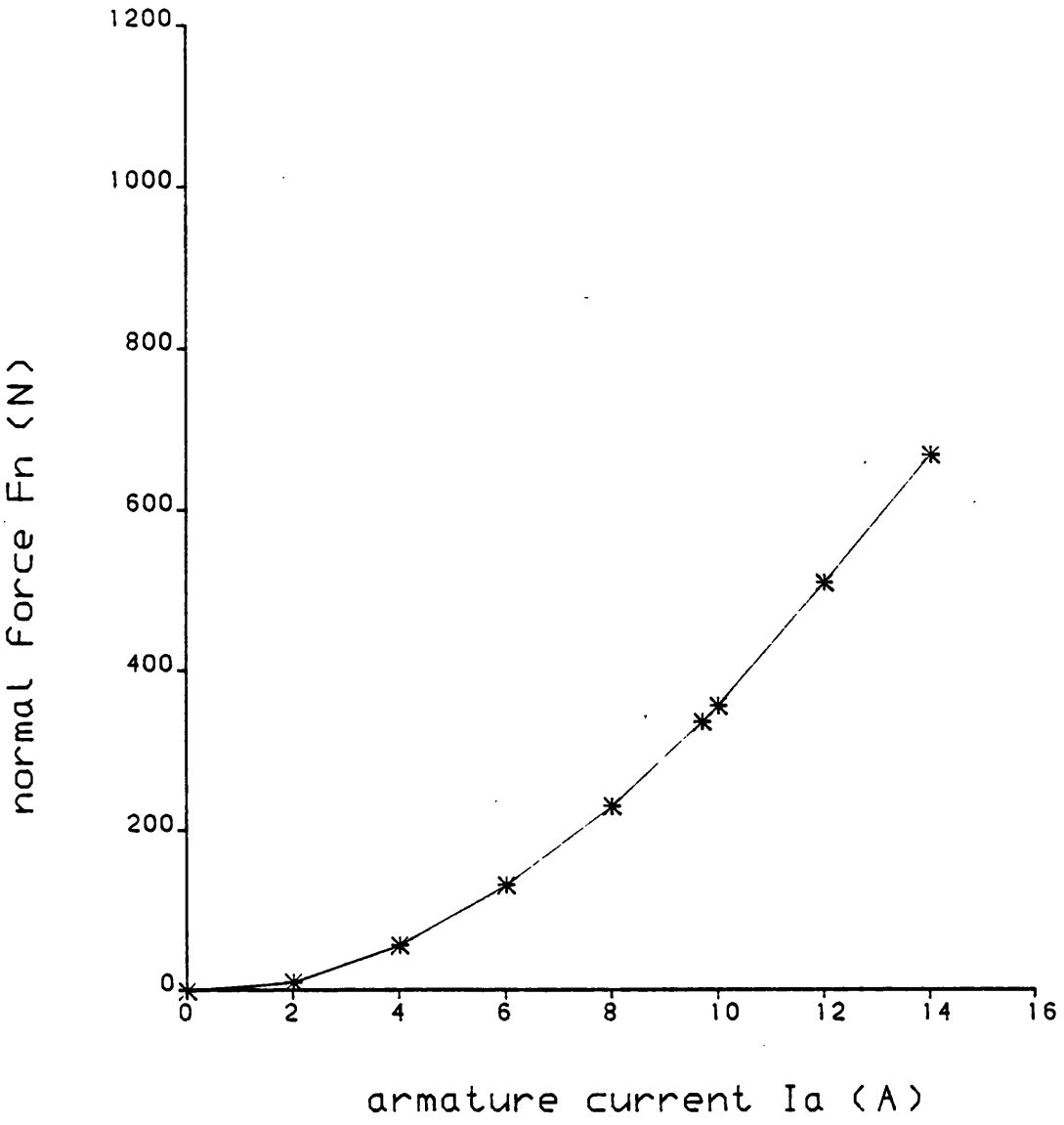

Fig. 5.3.7 Q-axis: normal force due to armature current measured at 16.67 Hz

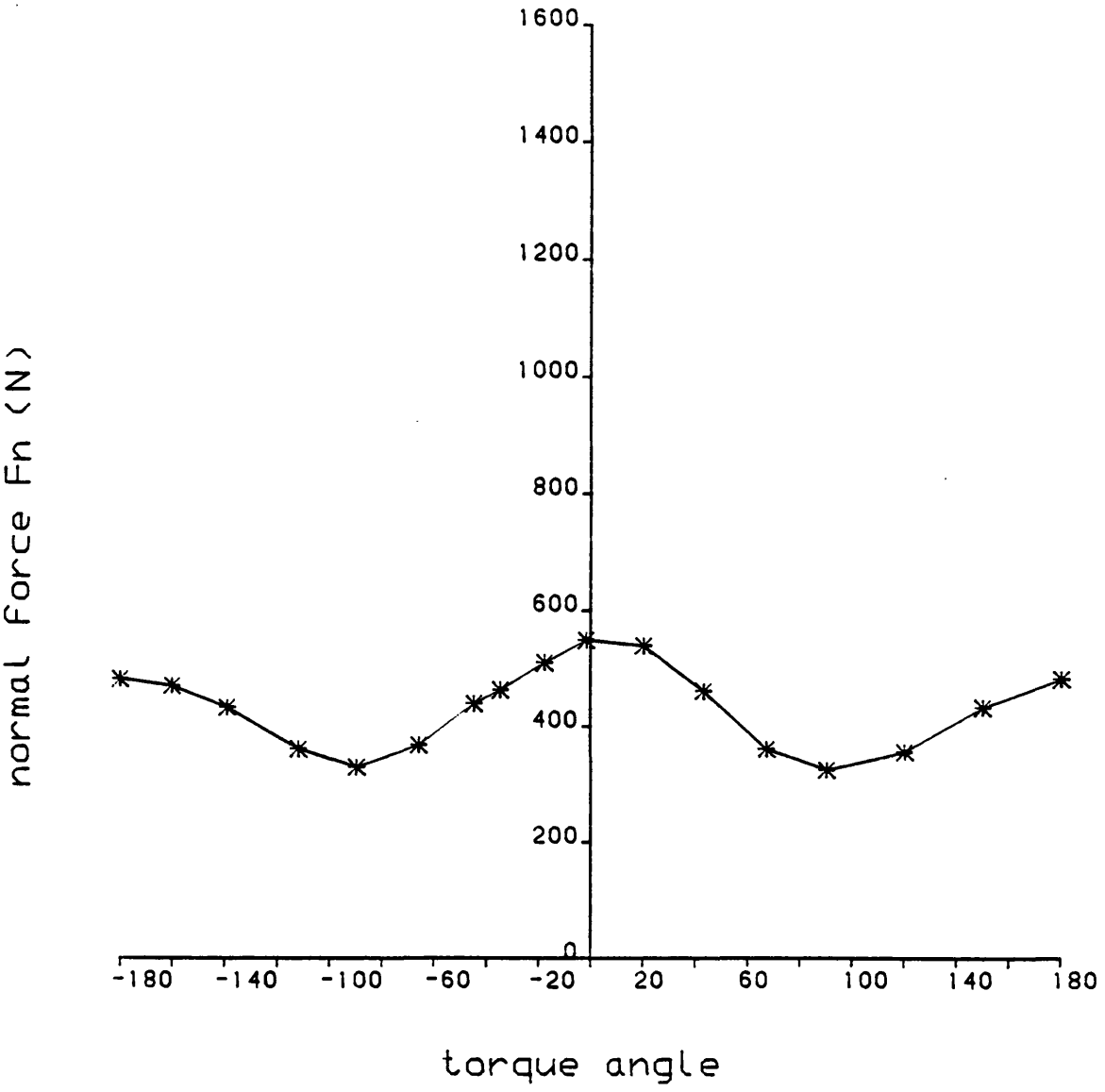

Fig. 5.3.8 Variation of normal force with torque angle due to an armature current of 9.7 amp and a frequency of 16.67 Hz

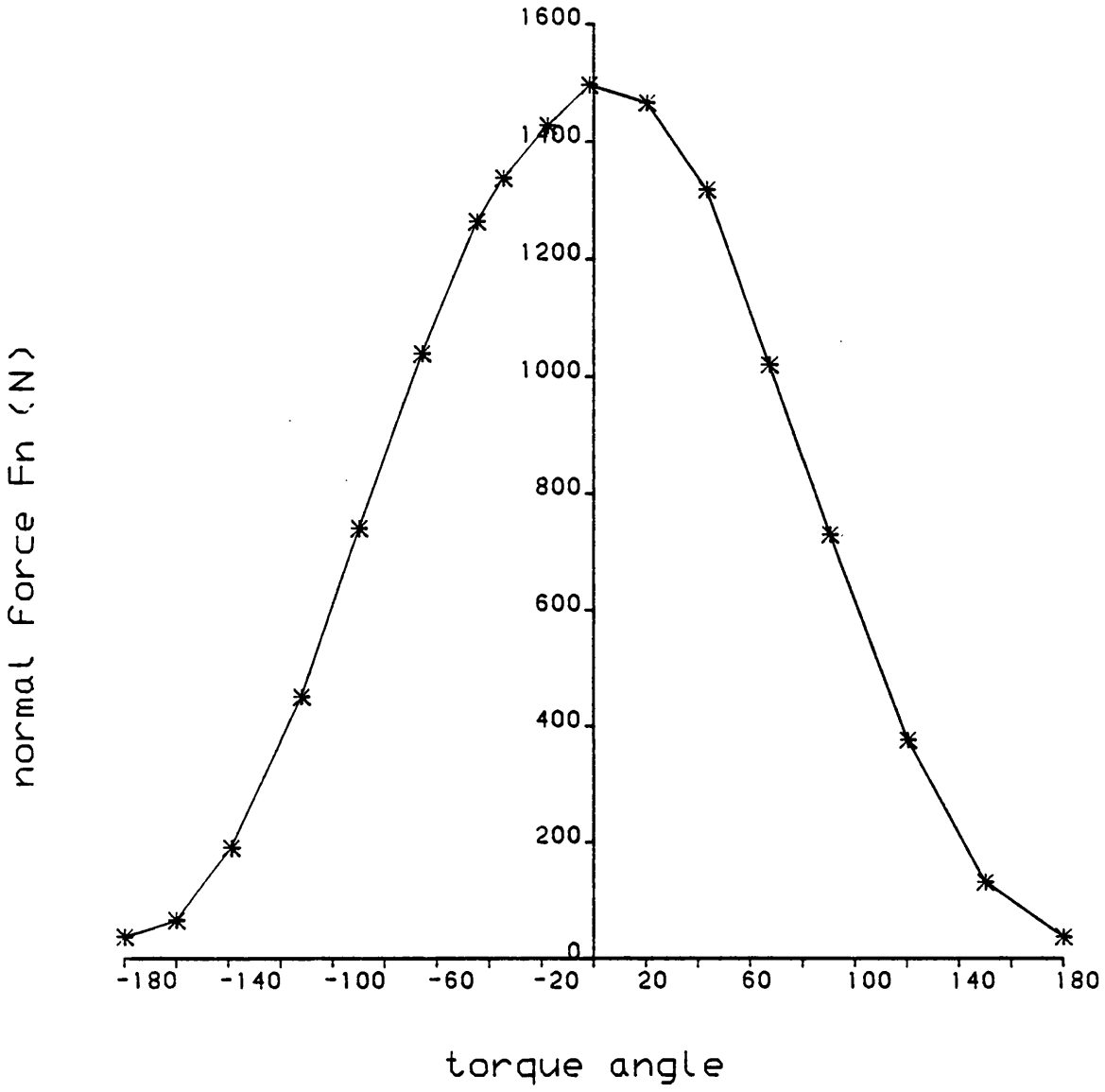

Fig. 5.3.9 Variation of normal force with torque angle due to a field current of 5 amps, an armature current of 9.7 amps and a frequency of 16.67 Hz

5.4 Discussion and Conclusion

The use of a cylindrical version of the homopolar LSM enables the longitudinal edge losses, which are present in a true linear machine, to be separated from the other losses which are normally present. The entry edge effect causes a reduction of flux density in the air gap of a linear motor, but not, of course, in a cylindrical machine. This reduction of flux has been explained in terms of eddy currents in reference 5.2. The effect of flux reduction on the open-circuit curve is shown in Fig. 5.4.1. This figure shows the curves of Figs. 5.3.2(a) and (b) plotted to the same scale. It will be observed that flux reduction is greatest at the highest speed.

Examination of Fig. 5.3.3 shows that saturation is present in the d-axis even though the machine is not excited by a field current. In the q-axis (Fig. 5.3.4) there is virtually no saturation. This is due to the much larger effective air-gap in this axis.

The reduction in air gap flux density due to the entry edge causes the attractive force to decrease with speed. It was therefore necessary to perform the force measurements at a low frequency (16.67 Hz) so that a comparison could be made with predictions from the static mathematical model. Under load conditions, greatest saturation occurs at a torque angle of 0^{o} and it decreases as the absolute value of this angle increases. Furthermore, for torque angles of greater than 90^{o} the saturation effect may be neglected.

The good agreement between calculated and experimental results gives some confidence in the prediction method that was developed in Chapter 2. This model may now be used for producing further designs in which saturation effects are accounted for.

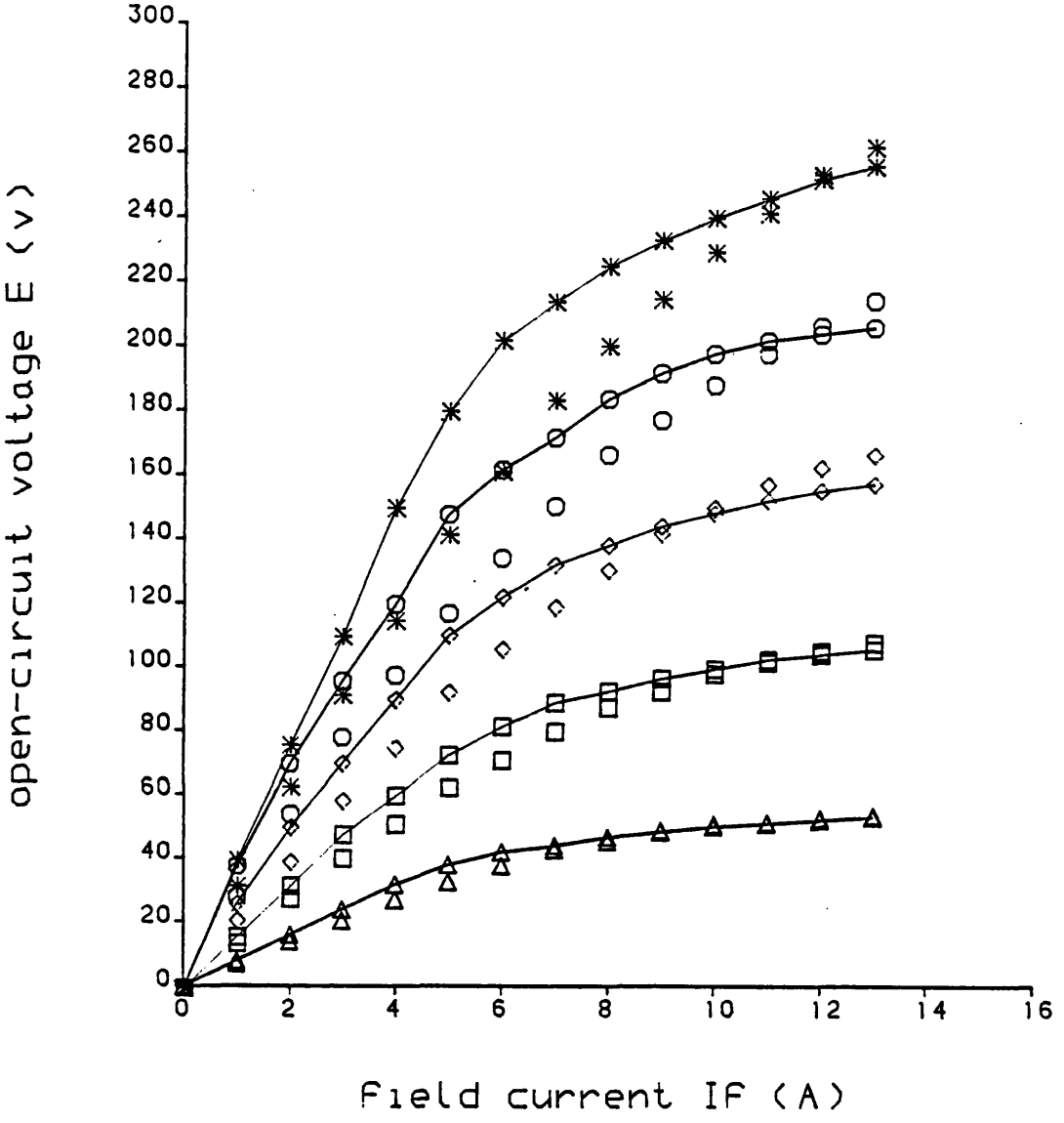

Fig. 5.4.1 Open-circuit test for cylindrical and flat LSM at many frequencies

Cylindrical				Flat
Δ–Δ–Δ–Δ–Δ	measurement at	16.67	Hz	Δ Δ Δ Δ Δ
□–□–□–□–□	"	33.33	Hz	□ □ □ □ □
◇–◇–◇–◇–◇	"	50	Hz	◇ ◇ ◇ ◇ ◇
o–o–o–o–o	"	66.67	Hz	o o o o o
––*–*–*	"	83.33	Hz	* * * * *

5.5 Appendix: Measurement of B-H Curves for LSM Stator Material

5.5.1 Introduction

Measurement of the flux-density against field strength curve for the stator core material used in the LSMs was performed using a 25 cm double-loop Epstein Square[5.5]. This square consists of four solenoids into which the test strips are inserted to form a closed magnetic circuit.

Both cylindrical and linear versions of the LSM were constructed using grain-oriented electrical steel. Since various parts of the machine were fabricated using material either aligned with the rolling direction (0^{o}) as at right angles to it, B/H curves for each direction were measured.

5.5.2 Specimen and winding assembly

Flat strips 30 mm wide and 250 mm long were cut for a particular specimen. No additional insulation was used on or between the strips. Six strips were used in each limb of the square. The effective cross-sectional area "A" of each limb was the same and was calculated from the following relationship

$$A = n.t.w \qquad 6.5.2.1$$

where

n: number of strips in each leg = 6

t: thickness of strip = 0.28 mm

w: width of strip = 30 mm

A: cross-sectional area of specimen = 5.04×10^{-5} m^2

In the Epstein square, using strips cut at 0^{o} to the rolling direction, 50 turns on each leg were connected in series to form 200 turns for the magnetization winding. Beneath this winding there were 6

turns on each leg which were connected in series to form 24 turns for the search coil. The Epstein square for strips cut perpendicular to the direction of rolling had 1840 turns for the magnetization winding and 24 turns for the search coil.

5.5.3 Test details

In the test, the method of dc reversal using the simple circuit shown in Fig. 5.5.1 was used. A magnetizing current was passed through the magnetizing winding on the square, while a flux meter was connected across the secondary winding (search coil). To obtain the flux density in the core with a certain current "i" amps in the magnetization winding the switch (s) across the flux meter was closed, the reversing switch S1 was set in position (a) and the variable resistor (R) adjusted until the magnetising current was "i" amps. This current was reversed several times and the switch left in position (a). This reversing was carried out to bring the iron into a cyclic state and thus avoid errors which could be caused by magnetic hysteresis. The switch across the flux meter was then opened and the flux meter pointer was set to zero. The magnetising current was reversed by moving the two way switch to position (b) and the flux meter deflection was noted. The procedure just described was repeated with increasing currents in the range 0 to 2.8 amps for the 90^{o} specimen. For both of these tests, the magnetising current was increased in steps of 0.01 amps and the deflection of flux meter for each step were taken. The magnetic field strengths and corresponding flux densities were determined from the following equations:

$$H = \frac{N_1 i}{\ell} \qquad 5.5.3.1$$

$$B = \frac{\lambda}{2N_2 \times A} \qquad 5.5.3.2$$

where

H: magnetic field strength (A/m)

N_1: number of turns in magnetising winding

ℓ: mean path length (taken as 0.94 m)

i: magnetising current (A)

B: flux density (T)

λ: measured flux linkage with search coil (Wb-turn)

N_2: number of turns of search coil

Figures 5.5.2 and 5.5.3 show the B/H curves for the two rolling directions.

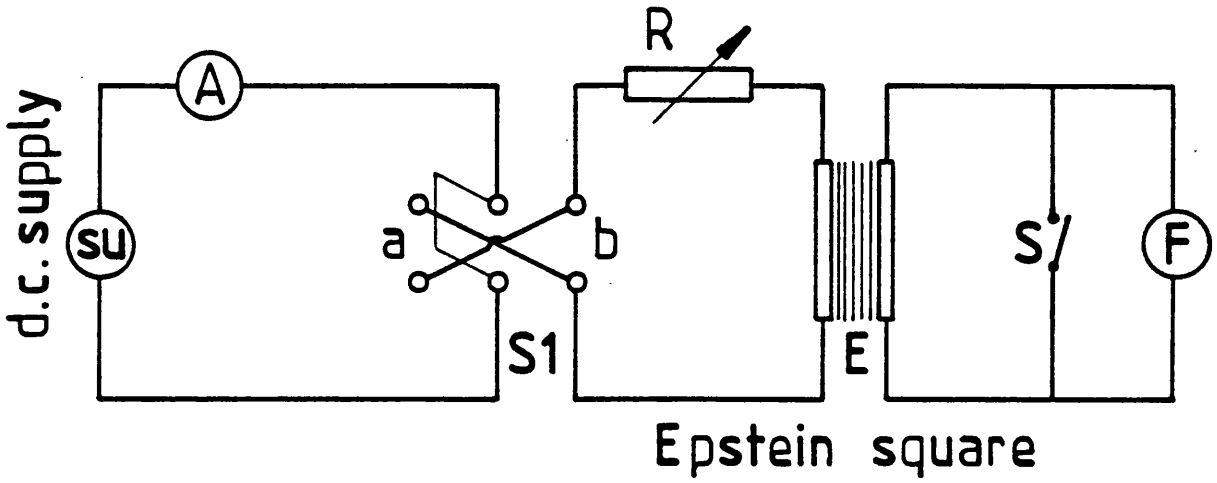

Fig 5·5·1 : circuit used for B-H curve measurement.

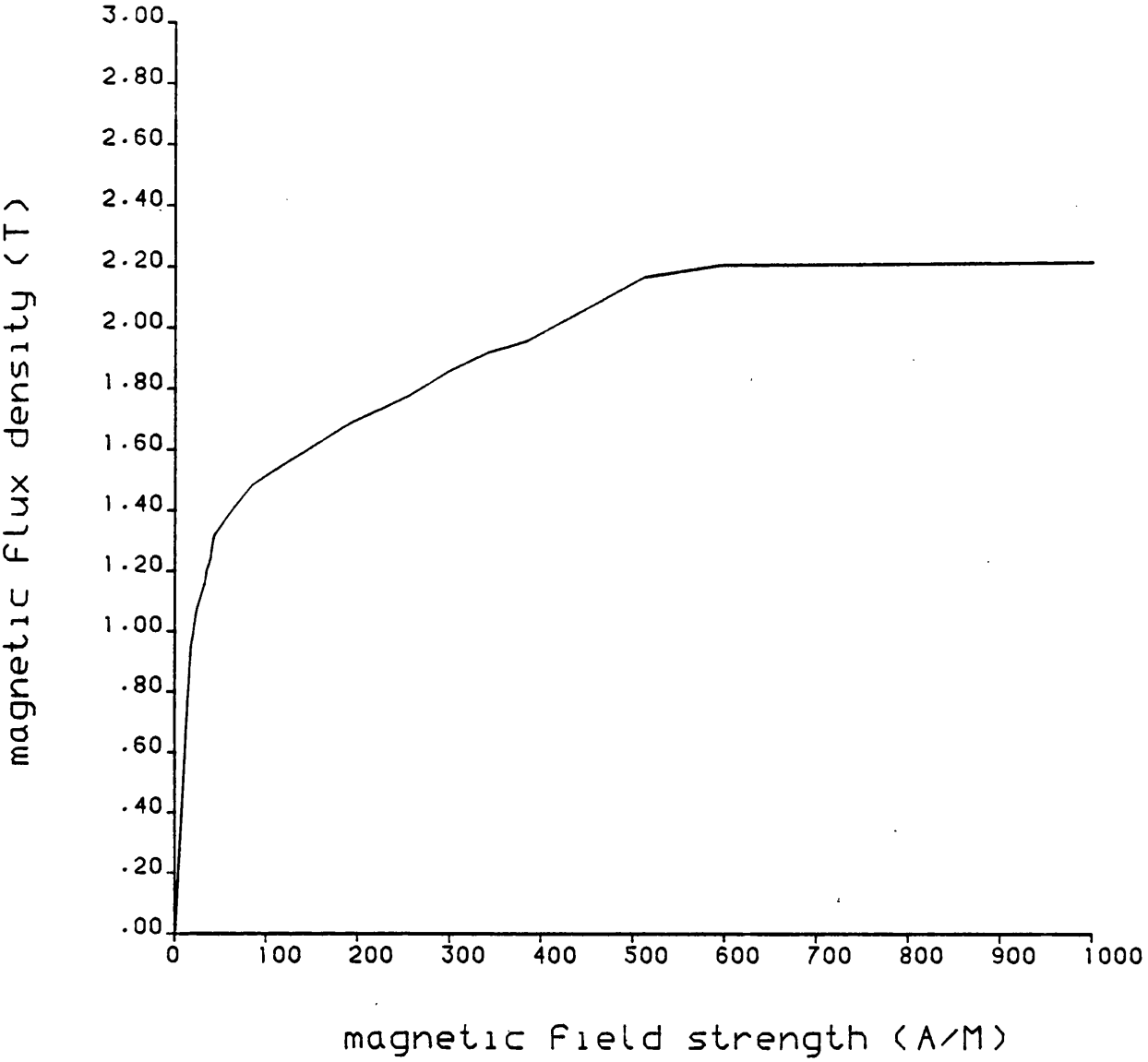

Fig. 5.5.2 Magnetisation curve for stator material in which the flux passing an iron with 0^{o}

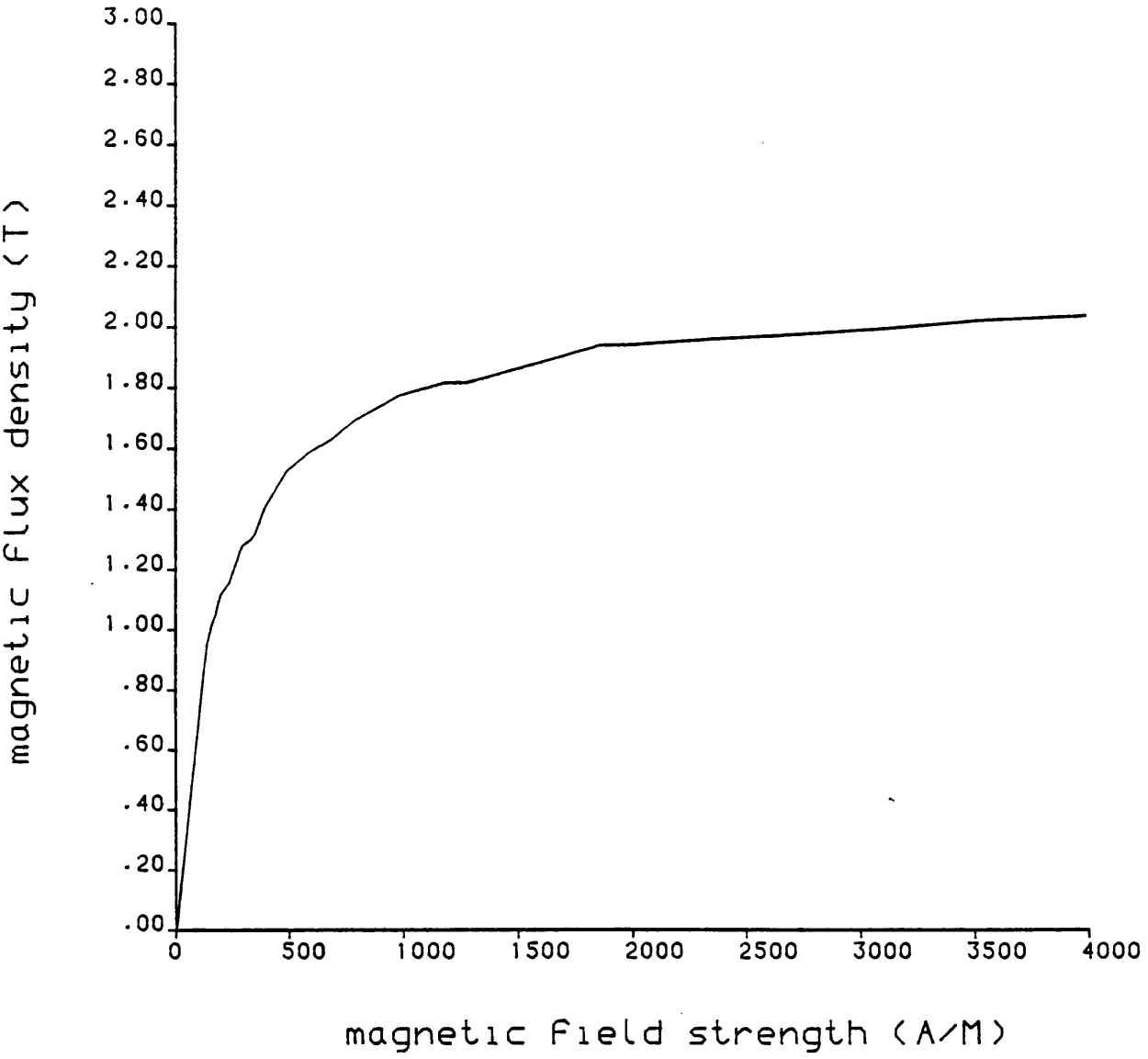

Fig. 5.5.3 Magnetisation curve for stator material in which the flux passing an iron with 90^{o}

References

5.1 Eastham, J.F.:
"Iron-cored linear synchronous machines", Electronics and Power, 1977, 23, pp.239-242.

5.2 Balchin, M.J. and Eastham, J.F.:
"Characteristics of a heteropolar linear synchronous machine with passive secondary", IEE Elect. Power Appl. (GB), Vol.2, No.6, pp.213-218.

5.3 Laithwaite, E.R.:
"Induction Machines for Special Purposes", (Newnes, 1966).

5.4 Eastham, J.F. and Laithwaite, E.R.;
"Linear motor topology", Proc.IEE, 1973, 120(3), pp.337-343.

5.5 British Standard:
"Steel sheet and strip for magnetic circuits of electrical apparatus", BS 601, Part 5, July 1973.

CHAPTER SIX

A COMPARISON OF THE CHARACTERISTICS OF HETEROPOLAR AND HOMOPOLAR LINEAR SYNCHRONOUS MOTORS

6.1 Introduction

Interest has been shown recently in the application of linear synchronous motors (LSMs) to advanced transport systems. In reference 6.1, two forms of iron-cored linear synchronous machines were described and their capabilities for providing electromagnetic thrust and suspension were considered. In both types of machine the dc as well as the ac winding was placed on the stator, which is attached to the vehicle. This avoids the necessity for an expensive wound secondary.

Theoretical and experimental results for the performance of a heteropolar LSM were presented in references 6.2 and 6.3. A homopolar machine has been investigated in the previous chapters of this thesis. It is the purpose of this chapter to present an experimental comparison of the force and electrical characteristics of heteropolar and homopolar machines designed to give the same thrust[6.5].

6.2 Details of Designs and Comparison of Weights

The heteropolar and homopolar machines are single sided machines and their stators are of E-core and C-core construction respectively (see Figs. 6.1a and 6.1b). The armature winding is placed in slots in the centre limb in the heteropolar machine and in slots in the outer limbs in the homopolar. The two field coils of the heteropolar machine were connected in series as were the two sets of armature windings on the homopolar motor. The specificiations of both machines is given in Table 6.1, and all the dimensions are shown in Fig. 6.1. The test machines were operated with the same armature currents and current densities and the same field currents and current densities. Both machines have the same excitation flux density and the same pole face area and therefore produce the same thrust.

It is desirable to keep the motor weight to a minimum since this forms a large part of the total vehicle weight. At first sight the homopolar machine appears to be the lighter of the two types since it has a field winding that is 33% of the weight of that of the heteropolar machine. However, this advantage is offset by the requirement for two identical armature windings on the homopolar so that the overall stator weights in this case are substantially similar.

As mentioned above, the field as well as the armature windings are placed on board the vehicle and this results in considerable savings in track cost. In a particular system design it will be necessary to have a very simple track construction and to use as little material as possible. It will be observed from Fig.6.2 that the track members in both machines can be simply cut from flat bar material. A comparison of the rotor iron required for both machines shows that the homopolar rotor is about 80% of the weight of that of the heteropolar rotor.

6.3 Mechanical Characteristics

The thrust forces produced by heteropolar and homopolar machines are shown in Fig. 6.3. Both curves are approximately sinusoidal functions of the torque angle and have maximum values near a torque angle of 90^{o}. The small shift away from sinusoidal is caused by the small reluctance torque. In the case of the heteropolar machine (Fig.6.3) the maximum thrust occurs at a torque angle just greater than 90^{o} while the maximum thrust of the homopolar occurs at just under 90^{o}. The reason for these differences is because $L_{md} < L_{mq}$ in the heteropolar machine and $L_{md} > L_{mq}$ in the homopolar. This effect becomes smaller, when L_{md} and L_{mq} are closer in value or when the excitation force is large compared with that of the reluctance force. At a torque angle of 90^{o}, as shown in Fig.6.3,

the experimental machines produced about the same thrust at all speeds.

Fig.6.4 shows the normal force as a function of torque angle for fixed values of field and armature currents. It will be observed that the heteropolar machine produces much more attractive force than the homopolar. The reason for this is the high flux density in the side limbs of the heteropolar machine. The normal force could be reduced by increasing the area of outer limbs. However, whilst this would have the advantage of reducing the excitation requirement, larger rotor poles would be needed leading to an inevitable increase in track costs.

The normal and thrust forces produced by both types of LSM are influenced by the longitudinal edge effect. As the poles enter the front of the machine, eddy currents are induced in the rotor poles and this causes a delay in the build up of flux. Increasing the motor speed gives an increase in the end effects and in consequence, a reduction in the available mechanical force. This effect appears to be less marked in the homopolar machine, presumably because of the smaller amount of rotor iron. The eddy current losses present when solid poles are used may be acceptable for urban speeds. For operation at higher speeds a limited amount of pole lamination may be necessary.

In order to exploit both thrust and lift forces with a minimum amount of interaction[6.2,6.3], it has been suggested that operation of the machine be at a fixed torque angle of 90^{o}. This gives nearly maximum thrust and nearly minimum attractive force due to the armature current. A simple control system may be used to maintain a constant clearance between the stator and the track because at this torque angle a large change of thrust with little change of attraction can be obtained. Table 6.2 gives the values of thrust/lift produced at the torque angle

of 90^{o}. The value of 0.05g, obtained for the heteropolar machine is probably too low for urban transport application (a figure of 0.15g has been suggested). This figure may be increased by reducing the field flux density but this will increase the track cost as mentioned above. The homopolar machine produces a thrust to lift value that is rather too high. In this case, however, a reduction can be effected by reducing the armature amp-turns.

Although the homopolar machine produces a more suitable thrust/lift value, this is at the expense of making the normal force more sensitive to variations in both armature current and speed. The force produced by the field is 0.51 kN with maximum variations of 0.07 kN and 0.05 kN due to the armature current and speed. The corresponding figures for the heteropolar machine are 0.14 kN and 0.25 kN on the field produced force of 2.4 kN.

6.4 Electrical Characteristics

The variation in power factor of heteropolar and homopolar LSMs with torque angle, when the values of the field and armature currents are kept constant is shown in Fig.6.5. At a torque angle of 90^{o}, both machines give the same power factor at low frequencies. At higher frequencies, the heteropolar machine has a higher power factor than the homopolar. This is because the reduction of L_d, L_q and M_{af} by end effects is about the same in the heteropolar machine leading to the geometry of the phasor diagram being approximately maintained. In the homopolar machine the leakage reactance forms a greater part of L_d and L_q than it does in the heteropolar.

The leakage is higher because of the homopolar rotor construction and also because there are two armature windings. Because of the greater leakage component L_d and L_q are not replaced by end-effects as rapidly as M_{af}. This results in the serious restriction in power factor with increasing speed.

Fig.6.6 shows the efficiency of the linear machines as a function of torque angle when the field and armature currents are constant. At low frequencies and at a torque angle of 90^o both LSMs have about the same efficiency. At higher speeds the homopolar machine is always more efficient as a direct consequence of the lower excitation requirement. Furthermore, at all frequencies, near optimum efficiencies can be achieved at a torque angle of 90^o.

6.5 Conclusions

A comparison of the performance of prototype heteropolar and homopolar LSMs has been given. The designs are not representative of full-sized traction machines since very small air-gaps were used.

The homopolar machine has the following advantages over the heteropolar. These are:

a) smaller volume of track material required.

b) better thrust/lift ratio.

c) better efficiency.

These advantages must be weighed against the drawbacks, which are:

a) normal force more sensitive to changes in armature current and speed.

b) lower power-factor.

Although the lower power-factor is a serious disadvantage, a reduction in stator reactance could be achieved in several ways. In references 6.2 and 6.3 the possibility of using different pole structures has been mentioned. In reference 6.4 the end winding leakage reactance of a high speed linear induction motor was reduced by eliminating the teeth altogether and producing an air gap winding. This method could also be used in LSM designs to further reduce L_q. However the increased gap between the iron surfaces of the stator and track poles would lead to an increased excitation requirement.

	Heteropolar	Homopolar
Series conductors per armature slot	140	140
Series conductors per field slot	600	400
Slots per pole and phase	2	2
Coil pitch (slots)	4	4
Slot type	Semi-closed	Semi-closed
Slot depth	29 mm	29 mm
Total armature slots	24	48
Total field slots	2	2
Number of poles	4	4
Stator iron weight	23.5 Kg	22.1 Kg
Stator copper weight	11.6 Kg	12.7 Kg
Total stator weight	35.1 Kg	34.8 Kg
Rotor iron weight (under stator)	3.61 Kg	2.89 Kg
Series connected	Field coils	Armature coils
Air gap length g	3.2 mm	3.2 mm

Table 6.1 LSM Dimensions

	Heteropolar	Homopolar
Thrust force at 16.7 Hz, kN	0.13	0.12
Lift force due to field, kN	2.4	0.51
Thrust/lift, g	0.05	0.24

Table 6.2 LSM Forces

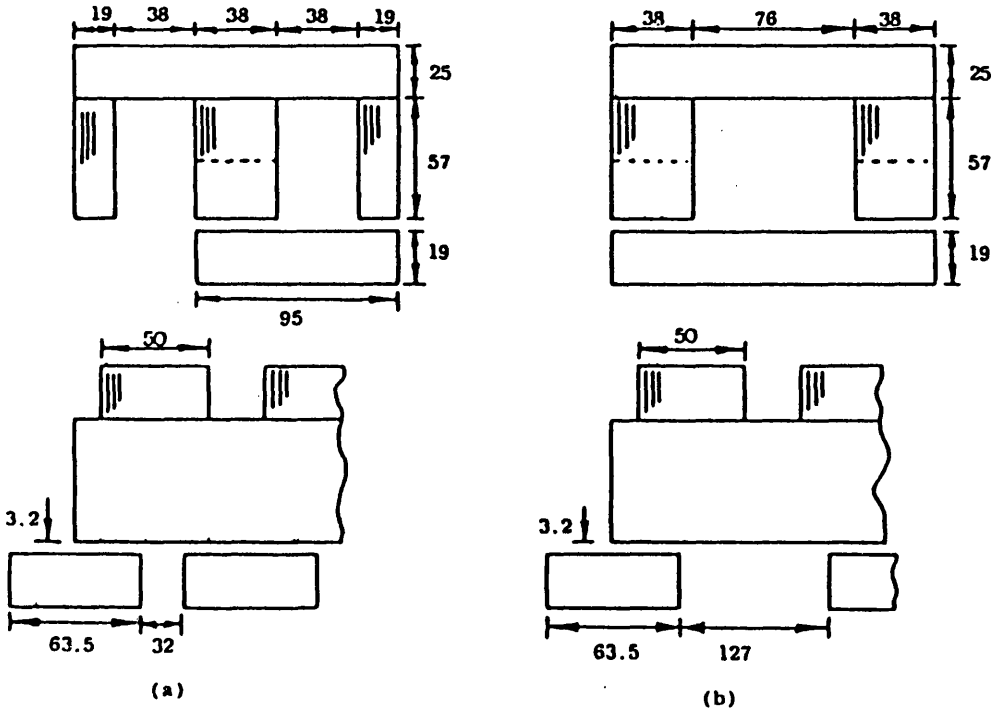

Fig 6·1 : machine dimensions

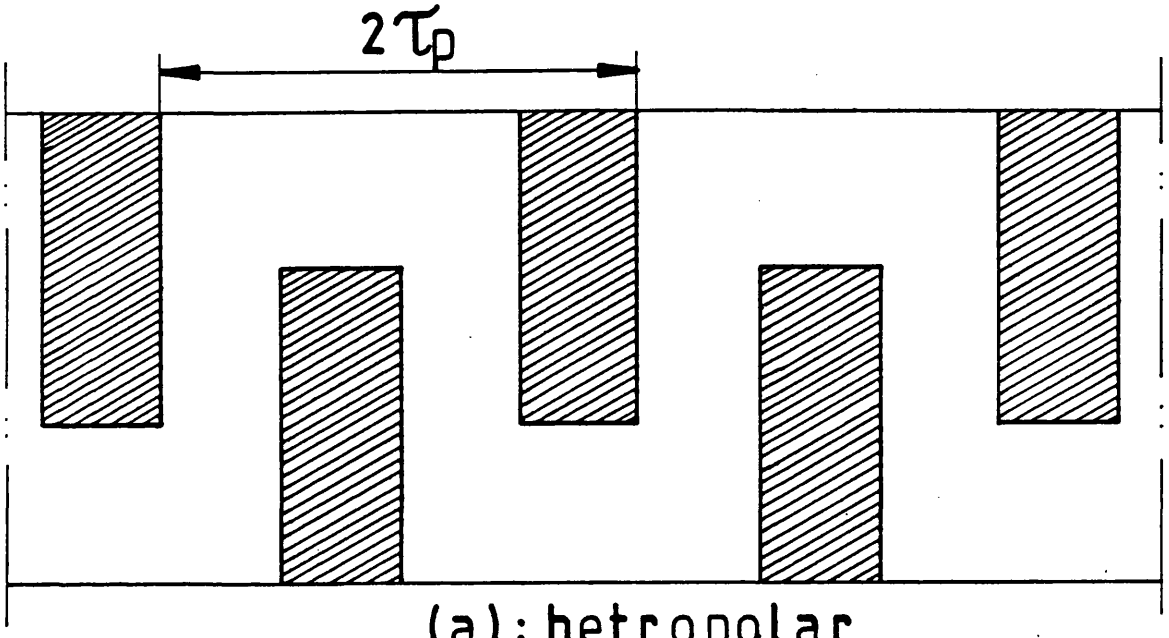

(a): hetropolar

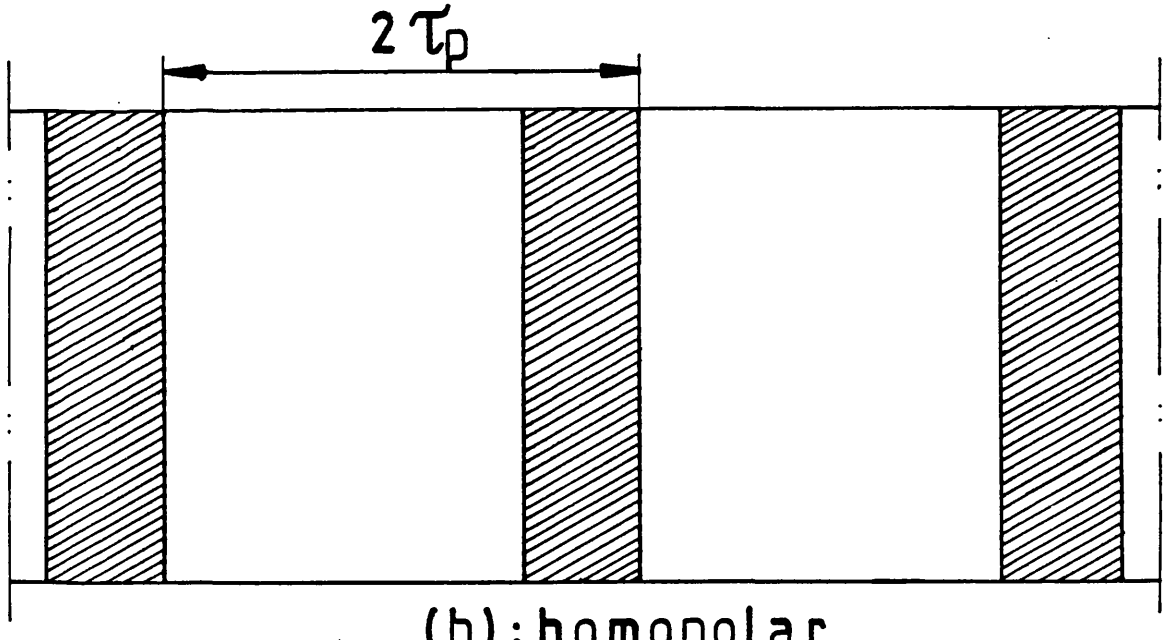

(b): homopolar

Fig 6·2 : rotor iron

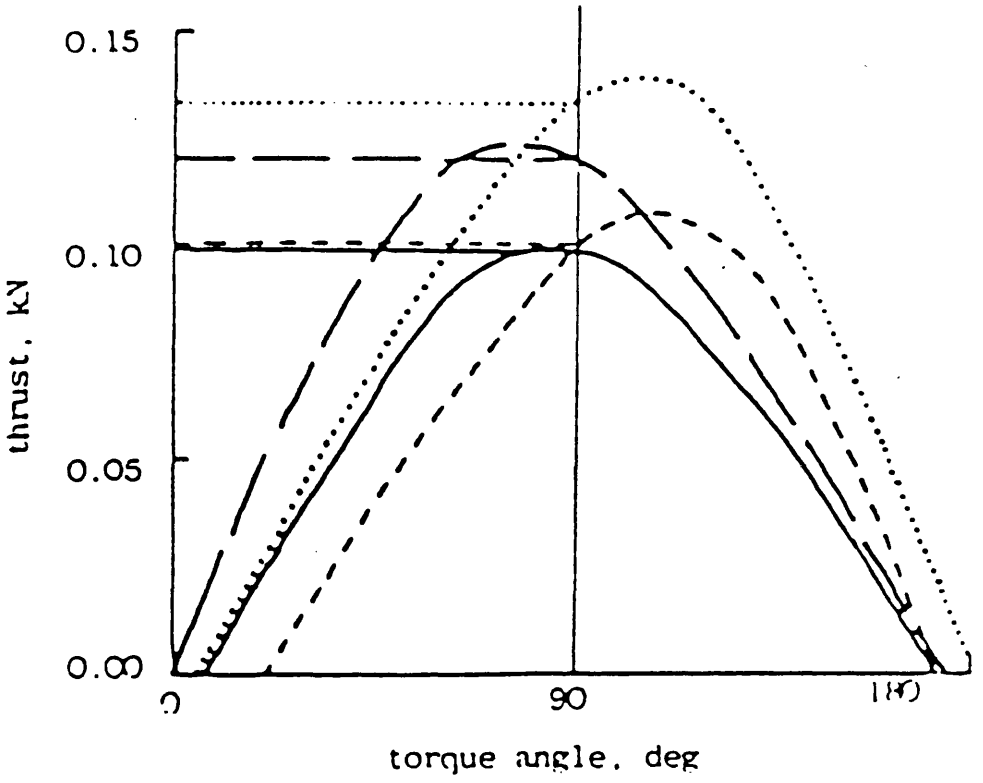

Fig 6·3 : thrust characteristics

Key to Figures

Heteropolar	16.7 Hz	----------
	83.3 Hz	— — — —
Homopolar	16.7 Hz	— — ·
	83.3 Hz	———

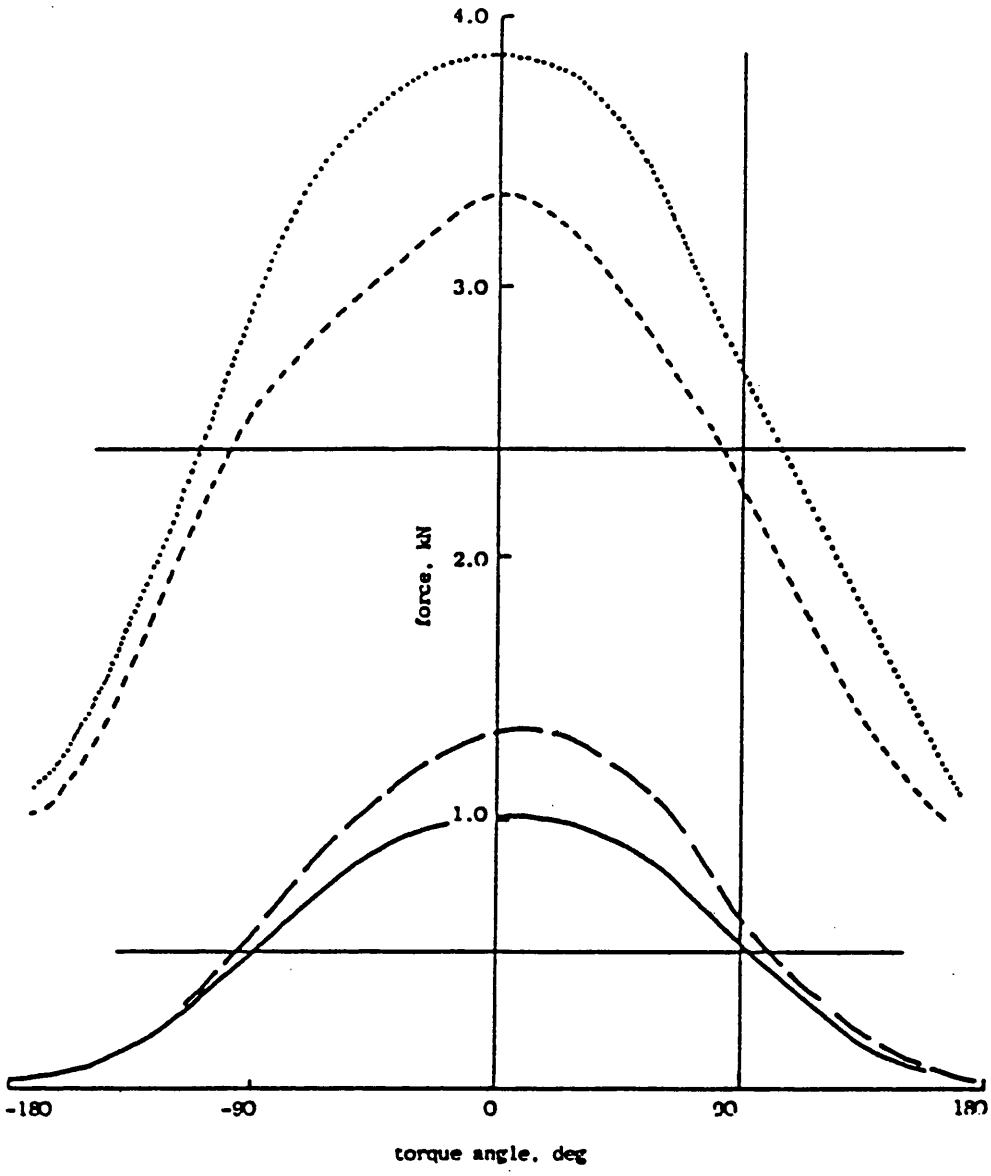

Fig 6·4 : attractive characteristics

Key to Figures

Heteropolar	16.7 Hz	.....
	83.3 Hz	- - - -
Homopolar	16.7 Hz	— — ·
	83.3 Hz	———

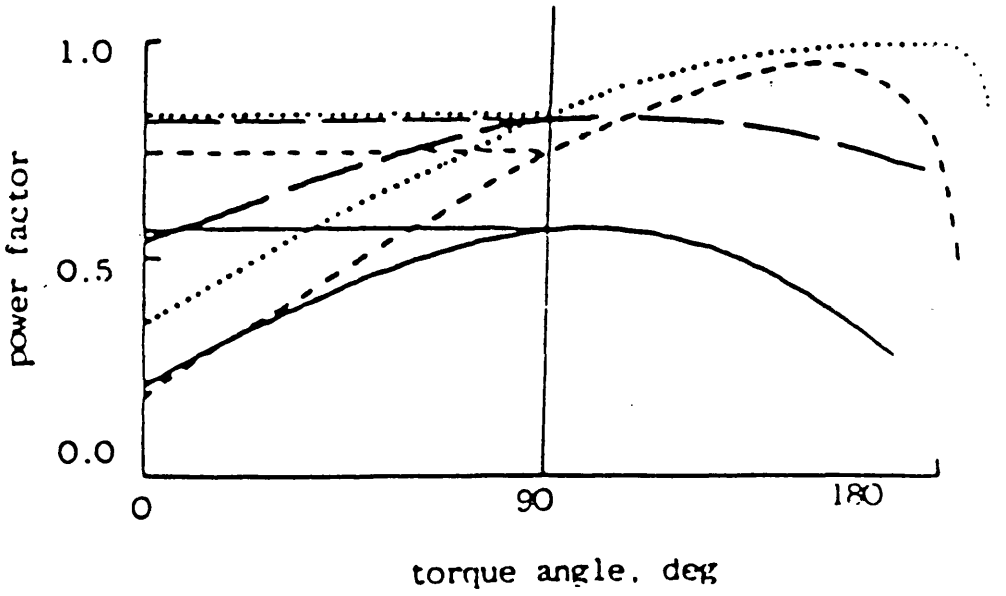

Fig6·5 : power factor

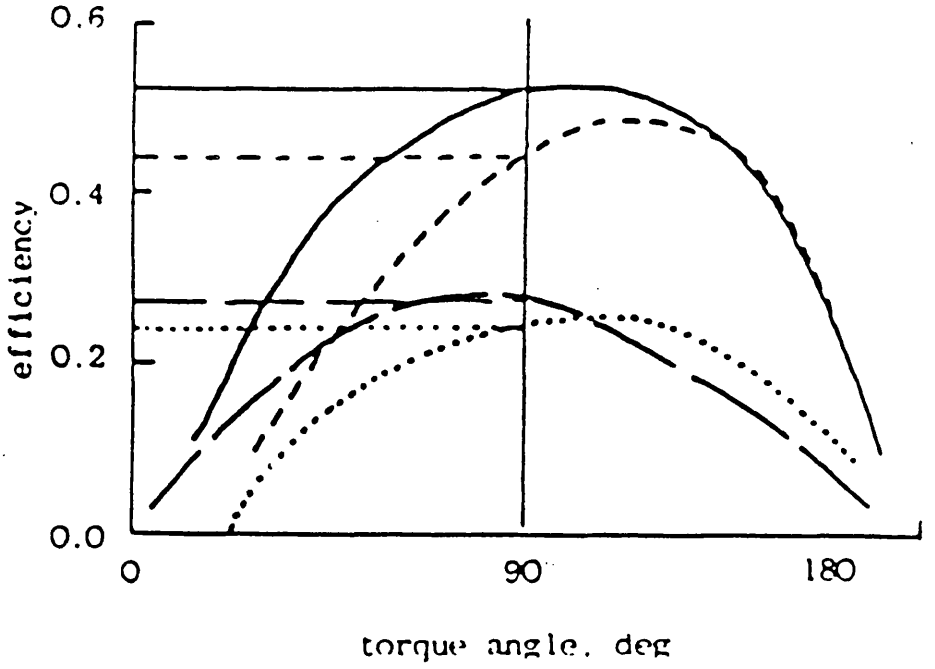

Fig6·6 : efficiency

Key to Figures

Heteropolar	16.7 Hz	.....
	83.3 Hz	- - - -
Homopolar	16.7 Hz	— — ·
	83.3 Hz	———

References

6.1 Eastham, J.F.:
"Iron-cored linear synchronous machines", Electronics and Power, 1977, 23, pp.239-242.

6.2 Balchin, M.J. and Eastham, J.F.:
"Characteristics of a heteropolar linear synchronous machine with passive secondary", Proc.IEE, Pt.A, Dec. 1979, Vol.2, No.6, pp.213-218.

6.3 Balchin, M.J.:
"Operating characteristics of a heteropolar linear synchronous motor", IEE Colloquium on Advanced Ground Transportation Schemes, April 1974, Digest No. 1979/27, pp.4.1-4.4.

6.4 Balchin, M.J. and Eastham, J.F.:
"Performance of linear induction motors with air-gap windings", Proc.IEE, Dec. 1975, Vol.122, No.12, pp.1382-1390.

6.5 Balchin, M.J., Helani, M.F. and Eastham, J.F.:
"A comparison of the characteristics of heteropolar and homopolar linear synchronous machines", IEE Colloquium on Linear Synchronous Machines for Magnetically-Levitated Vehicles, February 1983, Digest No. 1983/11, pp.3.1-3.4.

CHAPTER 7

CONCLUSIONS AND SUGGESTIONS FOR FURTHER WORK

For application in modern transport systems the advanced forms of linear synchronous machines provide an alternative to linear induction machines. Although linear analyses of the linear synchronous machines have been developed, a rigorous comparison between the various machine types requires that more detailed models be developed. To obtain more accurate predictions for the homopolar LSM, a numerical method for the solution of three dimensional magnetic fields taking the effects of saturation into account has been developed. The flux densities resulting from this method have been used to obtain the different machine characteristics which compared well with measurements, thus confirming the validity of the calculation method.

The field model was developed in network terms. The solution was in terms of scalar potential and there was one unknown for each element node point. The continuous field was assumed to be the sum of two fields, one to represent the sources and the other to represent the magnetization field. To avoid the possibility of an error occurring inside the iron region[1.14] it is necessary for this region to be current free and for all sources to exist in the branches of the air region. This procedure is possible since all Amperes' Law interaction paths can be made entirely in air.

The conditions imposed by interfaces are represented in the field model simply and directly in numerical form by assigning appropriate permeances to the network branches. The values of these permeances are proportional to permeability. This is constant in air and its value in the iron region depends on the magnetic induction. The field model interpreted in terms of a network is not complicated and should be familiar to electrical engineers.

Rectangular brick elements have been used to subdivide the field in the development of the network model. These elements are believed to be the most convenient for three dimensional work since they are easy to visualise. Boundary surfaces were arranged to coincide with the interface between adjacent elements. The node potential technique was used to solve the network model. The number of independent variables required for this solution is equal to the number of nodes in the network. The choice of the node potential solution method was made because it requires fewer independent variables (in 3 dimensions) than is required for a solution using the mesh method.

The field model of the homopolar LSM included an accurate representation of geometrical details such as teeth and slots. A periodicity condition was included in the boundary conditions so that it was only necessary to consider two poles of the machine. An iterative procedure was used for the solution of the node potential equations. The speed of convergence was enhanced by using successive over relaxation with an optimum accelerating factor, which was found by experiment to be about 1.8. Very accurate values for the node potentials are necessary. The maximum error was 5×10^{-10} of the maximum potential in a three dimensional network of 1873 nodes and 9893 branches.

The variation of μ was obtained using measured B-H curves and a non-linear iterative procedure . The permeabilities were corrected in stages after each linear network solution to reduce the permeability error to an acceptable level. Because the flux is the desired field quantity, the use of the node potential method does have a disadvantage in that the fluxes are not obtained directly. However, flux is easy to obtain from the nodal solution and it has been used to obtain the different

characteristics for the linear homopolar synchronous machine. Good agreement has been obtained by comparing these characteristics with the corresponding measured results.

The variation of L_{mf} and M_{af} with field current, that is with saturation, has been investigated using the flux linkage method. The saturation has a significant influence on both of these inductances when a high field current is employed. The curve of mutual inductance M_{af} has been used to derive the predicted open-circuit characteristic and this was shown to be in good agreement with the measured open-circuit curve. The use of cylindrical and linear versions of LSM for this measurement enabled the influence of the longitudinal end effect on the mutual inductance to be studied. It was found that the open circuit voltage of the linear homopolar machine decreased with speed. This was because the eddy currents in the solid rotor of the machine delayed the build up of flux.

The magnetizing inductances L_{md} and L_{mq} of the homopolar linear synchronous machine were determined using the flux linkage method. It was clearly shown that there is a dependence of L_{md} and L_{mq} on saturation. It was noted that the dependence of the direct axis magnetizing inductance L_{md} on saturation was marked at high values of armature currents, while that of the quadrature magnetizing inductance L_{mq} was much less dependent on saturation. This was because the interpolar air gap linearizes the flux distribution and it remains almost independent of the saturation. Both L_{md} and L_{mq} decreased with speed owing to end effects, but these reductions were less in value than that of M_{af}. The fringing effect has been discussed and considered for the calculated voltage appearing on the air gap. The influence of the leakage flux which failed to reach the rotor has also been investigated and the more accurate magnetizing inductances have been calculated leading to good agreement in comparison

with experimental results.

The equations derived in Reference 1.5 for calculation of thrust and normal force in a heteropolar LSM in terms of inductances, neglecting saturation effect, are valid for the homopolar machine. The saturation however, causes the maximum thrust, at a torque angle of approximately 90^{o}, to be reduced for a particular field current, whereas the normal force is reduced most at a torque angle of 0^{o}. This is because of the saturation of M_{af} and both L_{mf} and M_{af} respectively. As speed is inecreased, both thrust and normal forces are reduced by the end effect.

Different methods have been investigated for obtaining the normal force of the homopolar LSM for different operating conditions and taking saturation effects into account. These methods are based on the use of inductance, flux plot and Maxwell stresses. The last method gives the most accurate results. The closed Maxwell surface was chosen to surround the secondary member of the machine. An extension of this closed surface shown in Fig.4.4.4.1 enables the thrust force to be predicted. This extension was necessary because the resultant force acting on both sides of the rotor was too small to calculate accurately.

It is suggested that the homopolar linear synchronous machine be operated at a torque angle of 90^{o} since near maximum values of thrust, power factor and efficiency can be achieved. Furthermore, the interaction between the force produced by the field current and that produced by the armature current is at a minimum. Normal and thrust forces and also the power factor and efficiency are reduced with increasing speed because of end effects. In order to reduce this effect the eddy currents that occur in the solid rotor of the machine have to be reduced. This might be achieved by the use of a limited amount of pole lamination.

The investigation into the homopolar LSM has demonstrated that this type of machine can be used to generate both the lift and thrust required by a magnetically levitated vehicle. An experimental comparison of the characteristics of particular heteropolar and homopolar machines, given in Chapter 6[1.15] has demonstrated that the homopolar machine has the more suitable thrust/lift ratio for traction applications. The stator weight and volume of rotor iron are also less for the homopolar machine and this should lead to a more economical system. Further work is necessary in this area to establish whether the same advantages can be obtained from machines designed for a particular traction application. Further work is also necessary in order to compare competing designs of linear induction motor and linear synchronous motor.

A study of the normal forces and their relationship to the lateral forces which tend to centralise the primary with the track member is necessary to obtain an optimal design for the machine. A net lateral force may be realized while keeping the normal forces constant. This scheme requires the combined lift/guidance suspension system to be known. The lateral force is easy to predict using the computed flux density resulting from the three dimensional field analysis. The method of using Maxwell's surface surrounding the secondary member has been given to calculate this force in the centralised position of the rotor. To calculate the net lateral forces for different lateral positions of the secondary the input data should be modified to consider both limbs of the LSM. Further calculation and experimental results are needed to evaluate the lateral forces for a larger homopolar machine. This would be the subject of future research.